CHAPTER W22

Characterization of Materials

22.1 Introduction

The characterization of materials requires obtaining detailed information about the spatial arrangement of the atoms and identifying precisely which atoms occupy which particular sites in the crystal structure. It also includes the specification of imperfections, impurities, inhomogeneities, and so on. Often, it involves measuring some particular electronic or optical properties. In this chapter we describe a set of tools that the materials scientist has at his or her disposal to characterize materials physically. Some of these tools may be thought of as "cameras" that produce pictures of the material in real space. These include the scanning-electron microscope (SEM), the transmission-electron microscope (TEM), the scanning-tunneling microscope (STM), and the atomic-force microscope (AFM). Also included is the high-resolution transmission-electron microscope (HRTEM) and the low-energy electron microscope (LEEM). Other complementary tools take pictures in momentum space or wave-vector space rather than in real space. Included among these are apparatuses that study x-ray diffraction (XRD), low-energy electron diffraction (LEED), neutron diffraction, and reflection high-energy electron diffraction (RHEED). As with any still camera, information is most readily obtained about the static structure of the material, although the blurriness also conveys some dynamical information.

Additional tools provide information about the dynamical response of a material. Again, this information could be obtained as a function of the real time variable or as a function of the complementary frequency variable. In real time one may use time-dependent luminescent studies to capture the dynamical evolution of a system. Included among the numerous techniques available in frequency space are the optical spectroscopies: infrared, visible, and ultraviolet spectroscopy and light scattering, ellipsometry, infrared absorption, Raman scattering, photoluminescence, and nonlinear optical spectroscopy. Spectroscopy may also be performed with electrons in such techniques as electron energy-loss spectroscopy (EELS) and Auger emission spectroscopy (AES). Inelastic neutron scattering is often used. There are also spectroscopic techniques in which both the electrons and photons play a significant role, such as extended x-ray absorption fine-structure spectroscopy (EXAFS), x-ray photoemission spectroscopy (XPS), and ultraviolet photoemission spectroscopy (UPS). Included among the spectroscopic tools are a variety of resonance techniques: nuclear magnetic resonance (NMR), electron-spin resonance (ESR), nuclear-quadrupole resonance (NQR), and the Mössbauer effect.

Further information about the solid may be obtained using ionic probes, such as in secondary-ion mass spectrometry (SIMS) and Rutherford backscattering (RBS).

Positron beams are used in positron annihilation spectroscopy (PAS) and positive muon beams are used in the technique of muon-precession spectroscopy (μPS).

The chapter also touches briefly on transport measurements of electrical resistivity, the Hall effect, thermal conductivity, thermopower, and the Peltier coefficient. It describes some magnetic characterization tools, such as the Foner magnetometer, the Faraday balance, and the ac bridge. The SQUID magnetometer is discussed in the textbook in Section 16.7.[†]

Not all methods of characterization are of equal importance. Such techniques as XRD and NMR are more universally employed than others such as LEEM, EXAFS, and HRTEM. Therefore, more space is devoted in the chapter to the former than to the latter techniques. Nevertheless, all the methods in the chapter (as well as others) are used to characterize materials and so should be understood.

DIFFRACTION TECHNIQUES

In this section various diffraction techniques are studied. The most important is x-ray diffraction, which provides information about the long-range order in the bulk of the material. Low-energy electron diffraction provides similar information for the surface of the material. Reflection high-energy electron diffraction and neutron diffraction are also very useful in determining the structure. In particular, neutron scattering is sensitive to the magnetic ordering of a solid.

W22.2 X-ray Diffraction

When a beam of x-rays interacts with an arbitrary material its atoms may scatter the rays into all possible directions. In a crystalline solid, however, the atoms are arranged in a periodic array and this imposes strong constraints on the resulting diffraction pattern. It will be assumed for now that the temperature is sufficiently low that the atoms may be regarded as being frozen in position. Diffraction was introduced in Chapter 3, where the emphasis was on the kinematical aspects of the diffraction. In Section 3.4 the Bragg and von Laue points of view were stated and compared.

In the Bragg description, x-ray diffraction (XRD) is brought about by the constructive interference of waves scattered from successive lattice planes in the crystal. Each plane actually scatters from 10^{-4} to 10^{-3} of the incident wave. Referring to Fig. 3.6, let an incident beam of wave vector $\mathbf{k}$ impinge on a set of lattice planes, the rays making an angle θ with respect to the planes. Attention is restricted to the case of specular elastic scattering, so the outgoing scattered beam, of wave vector $\mathbf{k}'$, also makes an angle θ with these planes and

$$k' = k. \tag{W22.1}$$

The angle of deviation between the outgoing and incident rays is $\phi = 2\theta$. The separation between neighboring planes is denoted by d. The Bragg condition is given by

[†] The material on this home page is supplemental to *The Physics and Chemistry of Materials* by Joel I. Gersten and Frederick W. Smith. Cross-references to material herein are prefixed by a "W"; cross-references to material in the textbook appear without the "W."

Eq. (3.52). Constructive interference between successive paths occurs when the path difference equals an integer number of wavelengths.

Von Laue regarded x-ray diffraction as coming about due to the scattering of photons from the periodic lattice. Since the crystal possesses a discrete translational symmetry, there is only wave-vector conservation modulus a reciprocal lattice vector **G**. The incident and outgoing wave vectors have the same magnitude and are related by Eq. (3.54). It follows that

$$G^2 + 2\mathbf{G} \cdot \mathbf{k} = 0 \tag{W22.2}$$

As a result, only very specific directions of the incident wave vector **k** will result in diffracted beams.

There are at least four ways that one may perform x-ray diffraction experiments:

1. *Using a broadband (nonmonochromatic) x-ray source and looking at the back-reflection*. By utilizing a broadband source such as is produced by bremsstrahlung, there will be a spread of frequencies and hence a spread of wave-vector magnitudes. Even if the angle of incidence is held fixed, there will be some values of k for which Laue backscattering will occur.
2. *Using a diverging (noncollimated) beam of x-rays*. Similarly, by using a beam with a spread of angles, it is possible for the Bragg formula to be satisfied even if k is held fixed.
3. *Using a monochromatic and collimated source but rotating the crystal until the diffraction condition is met*. It is also possible to keep the beam unidirectional and monochromatic but to rotate the sample through some angular trajectory. Whenever the angle is such that the Bragg condition is met, diffraction will occur.
4. *Diffracting the monochromatic x-rays from a powder*. In a powder there are mesoscopic-sized crystals oriented in arbitrary directions. If the x-ray beam impinges on such a powder there will be some orientations for which θ will satisfy the Bragg condition. Having fixed the direction that **k** makes with the normal to the crystal, any rotation of the crystal around **k** will still satisfy the Bragg condition. Such rotations will cause the Bragg spots to sweep out circles. Since there are a huge number of orientations present in a powder, a circular diffraction pattern is produced.

According to the Heisenberg uncertainty relation, a finite size Δs for a crystal fragment implies an uncertainty in the **G** vectors that give rise to diffraction maxima; that is,

$$\Delta G \Delta s \approx 1. \tag{W22.3}$$

This means that the diffraction lines are not perfectly sharp but rather have an angular width on the order of

$$\Delta\theta \approx \frac{\tan\theta}{G\Delta s}. \tag{W22.4}$$

This helps in satisfying the Bragg condition in a powder. It also permits a quantitative estimate of the degree of long-range order to be made by examining the width of the diffraction spots or lines.

Having determined the allowed directions for x-ray scattering from simple conservation laws, one proceeds to obtain expressions for the intensities of the various diffracted beams. X-ray energies are much larger than typical energies of electrons in the conduction band (e.g., the Fermi energy) or the energies of electrons in the upper valence bands (characterized by the energy gaps and bandwidths). However, the x-ray energy may be less than the binding energies of some of the deep-core electrons, particularly in the heavier elements. One may classify the electrons into two categories, which will be termed active and deep-core. *Active electrons* are the electrons in the conduction and upper valence bands; *deep-core electrons* lie in the deep bands. To a first approximation the active electrons may be treated as if they were free. The deep-core electrons are tightly bound to the nuclei and, aside from special resonance situations, are essentially inert.

The dynamics of a free electron interacting with an electromagnetic field follows from Newton's second law:

$$-e\mathbf{E}_0 \sin \omega t = m\mathbf{a}(t). \tag{W22.5}$$

The total instantaneous power radiated by the accelerating charge is given by Larmor's radiation formula:

$$P(t) = \frac{2}{3}\frac{e^2 a^2(t)}{4\pi\epsilon_0 c^3}. \tag{W22.6}$$

The time-averaged radiated power is thus

$$\langle P \rangle = \frac{e^4 E_0^2}{12\pi\epsilon_0 m^2 c^3}. \tag{W22.7}$$

The incident intensity (power per unit area) of the x-ray field is given by the product of the speed of light and the energy density in the field

$$I = \frac{c}{2}\left[\epsilon_0 E^2(t) + \frac{B^2(t)}{\mu_0}\right]. \tag{W22.8}$$

The time-averaged intensity is obtained by noting that the electric and magnetic energy densities are the same, so

$$\left\langle \epsilon_0 E^2(t) + \frac{B^2(t)}{\mu_0} \right\rangle = \epsilon_0 E_0^2, \tag{W22.9}$$

$$\langle I \rangle = \frac{\epsilon_0 c}{2} E_0^2. \tag{W22.10}$$

The cross section for x-ray scattering is the ratio of the scattered power to the incident intensity:

$$\sigma = \frac{\langle P \rangle}{\langle I \rangle} = \frac{8\pi}{3} r_0^2. \tag{W22.11}$$

This is the Thomson cross section for x-ray scattering. The quantity $r_0 = e^2/4\pi\epsilon_0 mc^2 = 2.818 \times 10^{-15}$ m is called the *classical radius of the electron*.

The scattered radiation is not emitted isotropically (i.e., equally in all directions). Consider first a linearly polarized incident electromagnetic wave. An electron oscillating back and forth constitutes a microscopic antenna. The angular distribution of this antenna is given by the dipole distribution

$$P \approx (\hat{k}' \times \hat{E}_0)^2. \tag{W22.12}$$

The polarization vector $\mathbf{E}_0$ is perpendicular to the wave vector of the incident beam $\mathbf{k}$. If $\mathbf{E}_0$ lies in the scattering plane (the plane containing $\mathbf{k}$ and $\mathbf{k}'$; see Fig. 3.6) the function above is proportional to $\cos^2\phi$. If it is perpendicular to the scattering plane, the function above is 1. For unpolarized radiation, which consists of an equal admixture of the two polarization states, the factor is $(1 + \cos^2\phi)/2$. The differential scattering cross section for scattering radiation into a given solid angle $d\Omega$ centered around angle θ is thus

$$\frac{d\sigma}{d\Omega} = \frac{r_0^2}{2}(1 + \cos^2 2\theta). \tag{W22.13}$$

This has been normalized so that when integrated over all solid angles, the previously obtained formula for the total cross section is regained.

Having derived the cross section for x-ray scattering from a single electron using classical mechanics, this result may now be generalized to the quantum-mechanical case. Two points need to be considered. First, the electron is to be described by a wavefunction whose magnitude squared gives the local probability density for finding the electron at a point in space. If space were decomposed into small volume elements, each element has a probability for containing the electron and hence will contribute to the total x-ray scattering signal. Second, each element radiates coherently to produce the scattered x-ray beam. Determination of the phase of the scattering is simple. Suppose that the element is located at position $\mathbf{r}$. The incoming field arrives at this position with phase $(i\mathbf{k} \cdot \mathbf{r})$. For the outgoing beam the radiation is created at position $\mathbf{r}$ and emerges with wave vector $\mathbf{k}'$. Therefore, the outgoing field has a phase factor $\exp(-i\mathbf{k}' \cdot \mathbf{r})$. The scattering amplitude has a phase factor $\exp[i(\mathbf{k} - \mathbf{k}') \cdot \mathbf{r}]$. The atomic form factor is the Fourier transform of the electron probability distribution:

$$f(\mathbf{q}) = \int n(\mathbf{r})\exp[i(\mathbf{k} - \mathbf{k}') \cdot \mathbf{r}]d\mathbf{r} = \int n(\mathbf{r})\exp[-i\mathbf{q} \cdot \mathbf{r}]d\mathbf{r}. \tag{W22.14}$$

where $\mathbf{q} = \mathbf{k}' - \mathbf{k}$ is the wave-vector transfer (proportional to the momentum transfer), $n(\mathbf{r})$ is the probability density for the electrons, and the integral extends over the volume of the crystal. The classical differential scattering cross section derived previously is multiplied by the absolute square of this factor and becomes

$$\frac{d\sigma}{d\Omega} = \frac{r_0^2}{2}[1 + \cos^2(2\theta)]|f(\mathbf{q})|^2. \tag{W22.15}$$

One may extend this result immediately to the case of x-ray scattering by an atom by interpreting $n(\mathbf{r})$ as the electron number density of the atom. Note that the nucleus, although electrically charged, does not contribute to the x-ray signal because of its heavy mass. As mentioned earlier, the deep-core electrons of the heavier elements also

are not effective in scattering x-rays, so Eq. (W22.15) should only be regarded as being approximate.

The case of x-ray scattering from a crystal may now be investigated. The scattering amplitude $F(\mathbf{q})$ for the crystal is given by Eq. (3.31). It may be expressed as the product of an atomic-form factor and a geometric-structure factor, as in Eq. (3.45). For a monatomic crystal the electron number density is taken to be a superposition of atomic densities and to be of the form

$$n(\mathbf{r}) = \sum_{\mathbf{R}} n_{\text{atom}}(\mathbf{r} - \mathbf{R}). \tag{W22.16}$$

In cases where there are several atoms per unit cell, the electron density is

$$n(\mathbf{r}) = \sum_{\mathbf{R}} \sum_{j} n_j(\mathbf{r} - \mathbf{R} - \mathbf{s}_j). \tag{W22.17}$$

In place of Eq. (3.34), one obtains

$$F(\mathbf{q}) = S(\mathbf{q}) \sum_{j} f_j(\mathbf{q}) \exp(-i\mathbf{q} \cdot \mathbf{s}_j). \tag{W22.18}$$

The final formula for the differential cross section becomes

$$\frac{d\sigma}{d\Omega} = \frac{r_0^2}{2} N^2 \left(1 + \cos^2 2\theta\right) \sum_{\mathbf{G}} \delta_{\mathbf{q},\mathbf{G}} \left| \sum_{j} f_j(\mathbf{G}) \exp(-i\mathbf{G} \cdot \mathbf{s}_j) \right|^2 \exp(-2\mathrm{W}), \tag{W22.19}$$

where N is the number of unit cells in the crystal. The factor $\exp(-2W)$, called the *Debye–Waller factor*, takes into account thermal fluctuations. It is introduced in Section W5.2. The existence of the N^2 factor points to the fact that x-ray Bragg scattering is a coherent effect.

In particular experimental implementations of x-ray diffraction, additional angular-dependent terms may enter. For example, in the rotating-crystal method there is a factor $1/\sin 2\theta$ that arises from the time the crystal spends satisfying the Bragg condition. If the crystal were to rotate with an angular velocity ω_c, the time integral of the von Laue momentum constraint would be

$$\int dt\, \delta(G^2 - 2Gk \sin\theta) = \frac{1}{2Gk\omega_c \cos\theta} = \frac{1}{2\omega_c k^2 \sin 2\theta}. \tag{W22.20}$$

This enters as an additional factor multiplying the differential cross-section formula. For the powder-diffraction method there is a different angular factor.

In Fig. W22.1 a Laue back-reflection diffraction pattern for x-rays backscattered from Si(111) is presented. In Fig. W22.2 an x-ray diffraction pattern from a powdered sample of β-SiC is presented. In this figure the intensities of the diffracted x-ray cones are plotted as a function of the scattering angle, 2θ. This type of graph conveys more

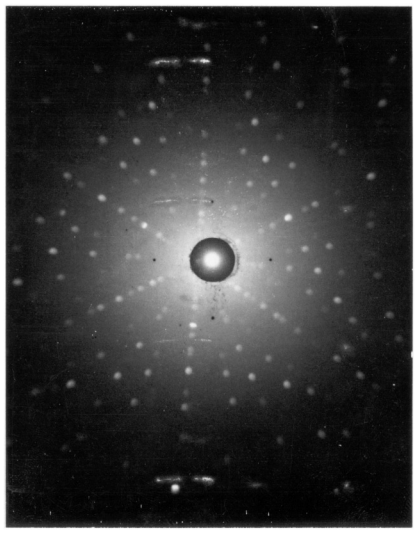

Figure W22.1. Laue back-reflection x-ray diffraction pattern for Si(111). The threefold rotational symmetry of the Si(111) planes is apparent.

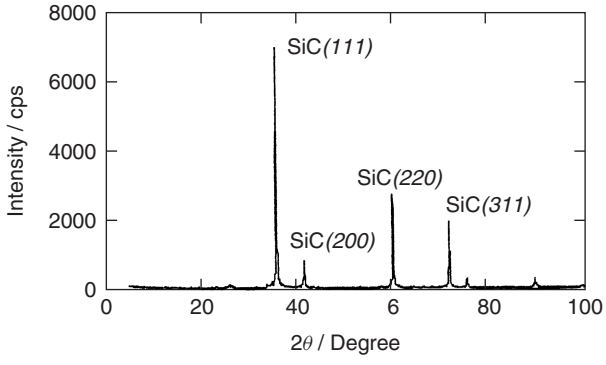

Figure W22.2. X-ray diffraction pattern of sintered SiC fiber-bonded ceramic powders. [Reprinted with permission from T. Ishikawa et al., *Science*, **282**, 1295 (1998). Copyright 1998, American Association for the Advancement of Science.]

information than the powder x-ray diffraction pattern that is presented in Fig. 6.16 in that the relative contributions from the different diffraction peaks are presented. In addition, the widths of the diffraction peaks are related to the quality of the crystallites. The larger and more perfect the crystallites are, the sharper the diffraction pattern will be.

W22.3 Low-Energy Electron Diffraction

C. J. Davisson and L. H. Germer, Phys. Rev., **30**, 705 (1927), directed a monoenergetic beam of electrons at the surface of a solid and found that the reflected electrons

consisted of a set of diffracted beams. This was consistent with the de Broglie hypothesis that, associated with electrons of momentum p, there is a wave with wavelength given by $\lambda = h/p = 2\pi/k$. The momentum of a free electron is related to the energy by $p = (2mE)^{1/2}$. Thus the wave vector of the electron is

$$k = \frac{2\pi}{\lambda} = \frac{1}{\hbar}\sqrt{2mE}. \tag{W22.21}$$

The solid-state crystal provides a microscopic diffraction grating for these electrons.

The wavelength of a 100-eV electron is 0.124 nm, a distance comparable to the spacing between atoms in a solid. The wavelength may be conveniently adjusted by varying the accelerating voltage of the electrons. This method of studying the crystal is called low-energy electron diffraction (LEED). Since the mean free path of electrons in crystals is short (typically, around 1.0 nm for 100 eV), the penetration distance is short. LEED is therefore a tool that provides information about the surface and the first few atomic layers of a solid.

The projectile electron interacts with the ion cores and electrons of the solid. Assume that the surface is flat on a distance scale large compared with the interatomic spacing. The interaction with the ion cores is primarily coulombic, whereas the interaction with the electrons includes an exchange contribution. The net result is that the potential energy is given by some function $V(\mathbf{R}, z)$, where $\mathbf{R}$ is a vector along the surface and z is the coordinate normal to the surface. In most cases of interest $V(\mathbf{R}, z)$ is a periodic function of $\mathbf{R}$ and may be expanded in a Fourier series

$$V(\mathbf{R}, z) = \sum_{\mathbf{G}} V_{\mathbf{G}}(z) \exp(i\mathbf{G} \cdot \mathbf{R}). \tag{W22.22}$$

Here the $\mathbf{G}$ vectors constitute a set of two-dimensional vectors called the *surface reciprocal net*. They play the same role in two-dimensional periodic systems as the reciprocal lattice plays in three dimensions. Note that the Fourier coefficients are themselves functions of z. The periodicity in the z direction is broken for two reasons. First, the crystal is terminated by the surface. Second, there is lattice-plane relaxation as discussed in Chapter 19. In many instances surface reconstruction occurs, in which the surface layer has a translational symmetry parallel to the surface which is not the same as the atoms in the bulk. The unit net of the reconstructed surface is in registry with the underlying bulk lattice and can include several bulk unit-cell projections.

In describing the kinematics of LEED there are two conservation laws operating. The first is conservation of wave vector parallel to the surface, modulus a reciprocal lattice vector

$$\mathbf{K}' = \mathbf{K} + \mathbf{G}. \tag{W22.23}$$

The second law is conservation of energy,

$$\frac{\hbar^2 k'^2}{2m} = \frac{\hbar^2 k^2}{2m}. \tag{W22.24}$$

Here the wave vector $\mathbf{k}$ is expressed as the sum of a vector lying in the surface plane, $\mathbf{K}$, and a vector perpendicular to the surface:

$$\mathbf{k} = \mathbf{K} + k_z \hat{z}. \tag{W22.25}$$

Similarly, for the outgoing electron,

$$\mathbf{k}' = \mathbf{K}' + k_z'\hat{z}. \tag{W22.26}$$

The scattering geometry is presented in Fig. W22.3. Note that the vector **K** has been drawn twice for presentation purposes. Let the angle the incident electron makes with the surface be θ and the corresponding angle for the outgoing electron be θ'. The conservation laws relate these angles:

$$\sin^2\theta' = \sin^2\theta - \frac{G^2 + 2\mathbf{K}\cdot\mathbf{G}}{k^2} = \sin^2\theta - \frac{G^2 + 2Gk\cos\theta\cos\psi}{k^2}, \tag{W22.27}$$

where ψ is the angle between **K** and **G**. Thus for a given incident angle there will be a set of outgoing angles corresponding to the different values of **G**. Naturally, the value of the right-hand side of Eq. (W22.27) must lie between 0 and 1 or the diffracted beam will be suppressed. The surface components of the electron wave vectors make an angle ϕ with respect to each other given by

$$\cos\phi = \frac{k^2(\cos^2\theta + \cos^2\theta') - G^2}{2k^2\cos\theta\cos\theta'}. \tag{W22.28}$$

A simple geometric interpretation of the result above is obtained by referring to Fig. W22.3. Since **k** and **k**′ have the same magnitude, they may be regarded as both touching a sphere (the Ewald sphere) of radius k centered around the origin. Their respective shadows in the plane of the surface must differ by a surface reciprocal-lattice vector in order to produce a diffraction peak. One may imagine a set of parallel rods extending upward from the surface piercing the Ewald sphere with the intersections determining the diffraction directions.

As mentioned in Chapter 19, in two dimensions there are five possible Bravais nets tiled with: squares, hexagons, rectangles, centered rectangles, and parallelograms. These are illustrated in Fig. 19.2. The primitive unit mesh vectors, $\mathbf{u}_1$ and $\mathbf{u}_2$, (as defined in Table 19.1), with their corresponding reciprocal net vectors, $\mathbf{G}_1$ and $\mathbf{G}_2$, are

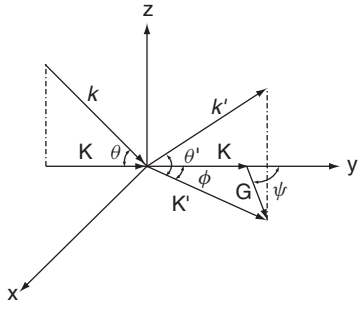

Figure W22.3. LEED scattering geometry: an incident electron with wave vector **k** is scattered to an outgoing state with wave vector **k**′.

TABLE W22.1 Five Bravais Nets and Their Properties

Bravais Net	Primitive Vectors	Reciprocal Lattice Vectors
Square	$a\hat{i}$	$(2\pi/a)\hat{i}$
	$a\hat{j}$	$(2\pi/a)\hat{j}$
Rectangular	$a\hat{i}$	$(2\pi/a)\hat{i}$
	$b\hat{j}$	$(2\pi/b)\hat{j}$
Centered rectangular	$a\hat{i}$	$(2\pi/a)\hat{i} - (2\pi/b)\hat{j}$
	$(a\hat{i} + b\hat{j})/2$	$(4\pi/b)\hat{j}$
Hexagonal	$a\hat{i}$	$(2\pi/a)[\hat{i} - \hat{j}/\sqrt{3}]$
	$a(\hat{i} + \hat{j}\sqrt{3})/2$	$(4\pi/a)\hat{j}/\sqrt{3}$
Oblique	$a\hat{i}$	$(2\pi/a)[\hat{i} - \hat{j}\cot(\phi)]$
	$b(\hat{i}\cos\phi + \hat{j}\sin\phi)$	$(2\pi/b)\hat{j}\csc(\phi)$

given in Table W22.1. They are related by

$$\mathbf{G}_1 = -2\pi\frac{\hat{k} \times \mathbf{u}_2}{\hat{k} \cdot \mathbf{u}_1 \times \mathbf{u}_2}, \qquad \mathbf{G}_2 = 2\pi\frac{\hat{k} \times \mathbf{u}_1}{\hat{k} \cdot \mathbf{u}_1 \times \mathbf{u}_2}. \tag{W22.29}$$

It is usually necessary to fit the observed LEED intensities to a model of the surface and near-surface region to obtain a detailed picture of the surface atomic structure. An example of a typical LEED pattern is given in Fig. W22.4. It shows the reconstruction of an Ir(100) surface with a 5×1 superstructure. The reciprocal lattice vectors are of the form $\mathbf{G} = h\mathbf{G}_1 + k\mathbf{G}_2$, with h and k being integers. The spots may be enumerated by these integers in the figure.

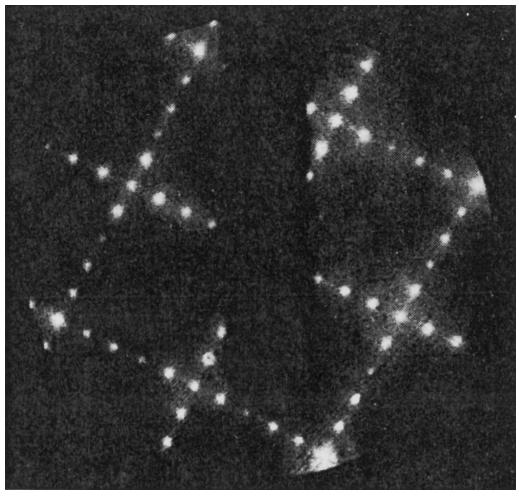

Figure W22.4. LEED pattern for a reconstructed Ir (100) surface. [Reprinted from K. Heinz, *Surf. Sci.*, **299/300**, 433 (1994), Copyright 1994 with permission from Elsevier Science.]

W22.4 Reflection High-Energy Electron Diffraction

In reflection high-energy electron diffraction (RHEED) a high-energy beam of electrons is directed at grazing angles of incidence onto the solid. The electron energy is in the range 10 to 100 keV and the angles are in the range 0.1° to 5°. The scattering mechanism becomes more Coulomb-like, with the dominant scattering in the near-forward direction. It is particularly sensitive to the surface structure of the solid.

Referring to the kinematic formulas developed for LEED and the corresponding figure (Fig. W22.3) illustrating the scattering geometry, the following simplifications are made. First, it is assumed that θ is small, so that $\cos\theta \approx 1$. For electrons in the energy range 10 to 100 keV the wave vector k is in the range 5.1×10^{11} m^{-1} to 1.6×10^{12} m^{-1}. This is typically two orders of magnitude larger than the reciprocal net vectors, G. One may therefore make a series expansion in powers of G/k and retain the lowest-order terms. Thus the numerical values for θ, θ', and ϕ and G/k are all small. The results are

$$\theta'^2 = \theta^2 - \frac{2G}{k}\cos\psi - \frac{G^2}{k^2}, \tag{W22.30}$$

$$\theta^2 = \frac{G^2}{k^2}. \tag{W22.31}$$

If a spherical screen is located a distance R from the sample along the y axis, spots will appear at the points

$$x = R\cos\theta'\sin\phi \approx R\phi \approx \pm\frac{RG}{K}, \tag{W22.32a}$$

$$y = R\cos\theta'\cos\phi \approx R, \tag{W22.32b}$$

$$z = R\sin\theta' \approx R\theta' = R\sqrt{\theta^2 - \frac{2G}{k}\cos\psi - \frac{G^2}{k^2}}. \tag{W22.32c}$$

Note that $G\cos\psi = G_y$. Thus the spots lie on a circle whose radius is

$$r = \sqrt{x^2 + z^2} = R\sqrt{\theta^2 - \frac{2G_y}{k}}. \tag{W22.33}$$

If the surface of the solid consists of a square mesh of side a then the components of $\mathbf{G}$ are

$$(G_x, G_y) = \left(\frac{2\pi n_x}{a}, \frac{2\pi n_y}{a}\right), \tag{W22.34}$$

where n_x and n_y are integers. The radius of the circle is

$$r(\theta, n_y) = R\sqrt{\theta^2 - \frac{4\pi n_y}{ka}}. \tag{W22.35}$$

Corresponding to a given value of n_y is a circle of a given radius. The location of points along the circle is determined by n_x.

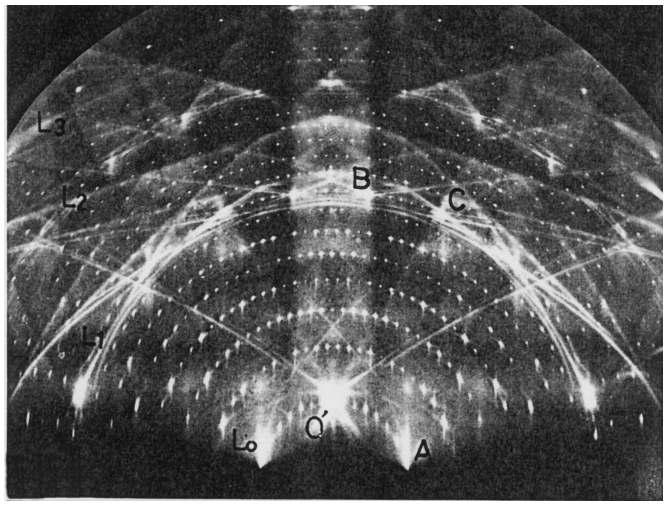

(a)

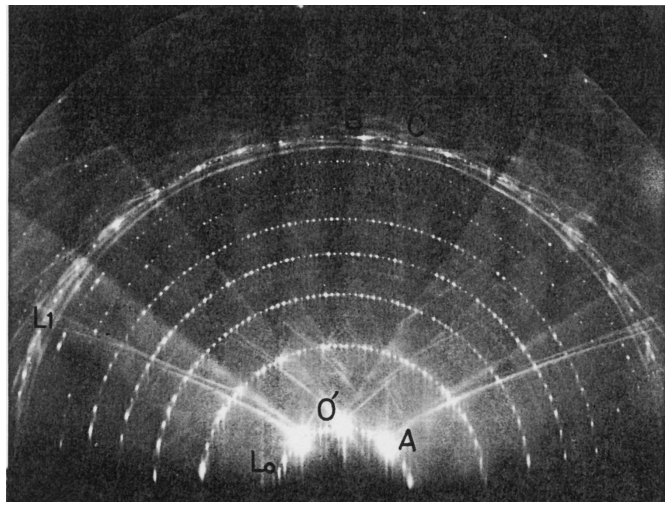

(b)

Figure W22.5. RHEED patterns taken with 20-keV electrons from Si (111) with the 7×7 structure. The upper pattern (*a*) is for $[\bar{1}2\bar{1}]$ and the lower pattern (*b*) is for $[0\bar{1}1]$ incidence. [From S. Ino, *Jpn. J. Appl. Phys.*, **16**, 891(1977). Copyright 1977 by the Japanese Journal of Applied Physics.]

Examples of RHEED patterns are given in Fig. W22.5. RHEED is used to monitor atomic layer-by-layer thin-film growth in MBE. Oscillations of spot amplitudes yield growth rates and provide information on the growth mode.

W22.5 Neutron Scattering

Neutron scattering involves directing a beam of neutrons from a nuclear reactor at a solid and monitoring the scattered neutrons with a detector. There are both elastic

and inelastic contributions. The elastic contribution produces a diffraction pattern and provides useful structural information such as interatomic spacings and symmetries of the crystal. Inelastic scattering provides information concerning the phonon spectrum and magnons in magnetic materials. Neutrons scatter off the nuclei via the strong interaction and off electrons by magnetic interactions. The cross sections are small, on the order of several square fermis [$(10^{-15}$ m$)^2$], so the mean free path is long. Therefore, information is obtained concerning the bulk sample. It makes a difference whether the sample is magnetized or not, and neutron scattering is therefore a valuable tool for probing the magnetic ordering of matter. Studies may be made as a function of temperature, external magnetic field, pressure, stress, or other thermodynamic variables. It provides a powerful tool for obtaining phase diagrams of materials.

The neutrons that emerge from the reactor are collimated into a narrow beam by placing absorbing shields in all but the desired beam direction. For thermal neutrons ($T = 300$ K) the mean wave-vector magnitude is $k = 4.3 \times 10^{10}$ m^{-1}. A monoenergetic source is constructed from the thermal source by Bragg scattering the neutrons off a crystal and further collimating the beam. By varying the angle of incidence the neutron energy is tunable through some range of values. The typical wave vector is several times greater than typical reciprocal lattice vectors G of samples to be studied. Scattering from magnetized crystals can produce a polarized neutron beam.

The discussion begins by studying the case of neutron diffraction (i.e., elastic scattering from the crystal). Suppose that the incident neutron wave vector is $\mathbf{k}$ and the scattered wave vector is $\mathbf{k}'$. The wave-vector transfer is

$$\mathbf{q} = \mathbf{k}' - \mathbf{k}. \tag{W22.36}$$

If the lattice is periodic in three dimensions, momentum is conserved modulus a reciprocal lattice vector, implying that

$$\mathbf{q} = \mathbf{G}. \tag{W22.37}$$

The energy conservation condition is

$$\frac{\hbar^2 k'^2}{2M_n} = \frac{\hbar^2 k^2}{2M_n}, \tag{W22.38}$$

where M_n is the neutron mass. It follows that

$$q = 2k \sin \frac{\theta}{2}, \tag{W22.39}$$

where θ is the scattering angle between vectors $\mathbf{k}$ and $\mathbf{k}'$. The sample is rotated, and whenever $\mathbf{q} = \mathbf{G}$ is satisfied, a diffraction peak occurs. For single crystals the actual value of the $\mathbf{G}$ vector is determined from the knowledge of $\mathbf{k}$ and $\mathbf{k}'$.

As with x-ray diffraction, at finite temperatures the crystal may be regarded as an admixture of ordered and disordered phases. The disordered part does not produce a diffraction pattern but rather, produces a thermal diffuse background scattering. When the crystal temperature is raised so that it finally melts, there is only diffuse scattering. Additional contributions to the diffuse background are due to imperfections, impurities, the magnetic moments of unaligned nuclei, and isotopic inhomogeneities.

Inelastic neutron scattering is also possible. In this case one or more phonons or magnons are either absorbed or emitted by the neutron in the course of scattering. It is possible to measure the dispersion curve of these elementary excitations [i.e., to determine the dependence of their frequency $\omega(\mathbf{Q})$ on their wave vector $\mathbf{Q}$]. For absorption of a single phonon (or magnon) the conservation laws are

$$\mathbf{k}' = \mathbf{k} + \mathbf{Q} + \mathbf{G}, \qquad \frac{\hbar^2 k'^2}{2M_n} = \frac{\hbar^2 k^2}{2M_n} + \hbar\omega(\mathbf{Q}). \tag{W22.40}$$

The corresponding formulas for the emission of a single excitation are

$$\mathbf{k}' = \mathbf{k} - \mathbf{Q} + \mathbf{G}, \qquad \frac{\hbar^2 k'^2}{2M_n} = \frac{\hbar^2 k^2}{2M_n} - \hbar\omega(\mathbf{Q}). \tag{W22.41}$$

Phonons and magnons are excitations that obey Bose–Einstein statistics. The number of excitations in mode $\mathbf{Q}$ is given by the Bose–Einstein distribution function:

$$n(\mathbf{Q}, T) = \frac{1}{\exp[\hbar\omega(\mathbf{Q})/k_B T] - 1}. \tag{W22.42}$$

The relative contribution of occupied to unoccupied states should be in the ratio of the Boltzmann factor, $\exp[-\hbar\omega(\mathbf{Q})/k_B T]$. One therefore expects to see a spectrum (called

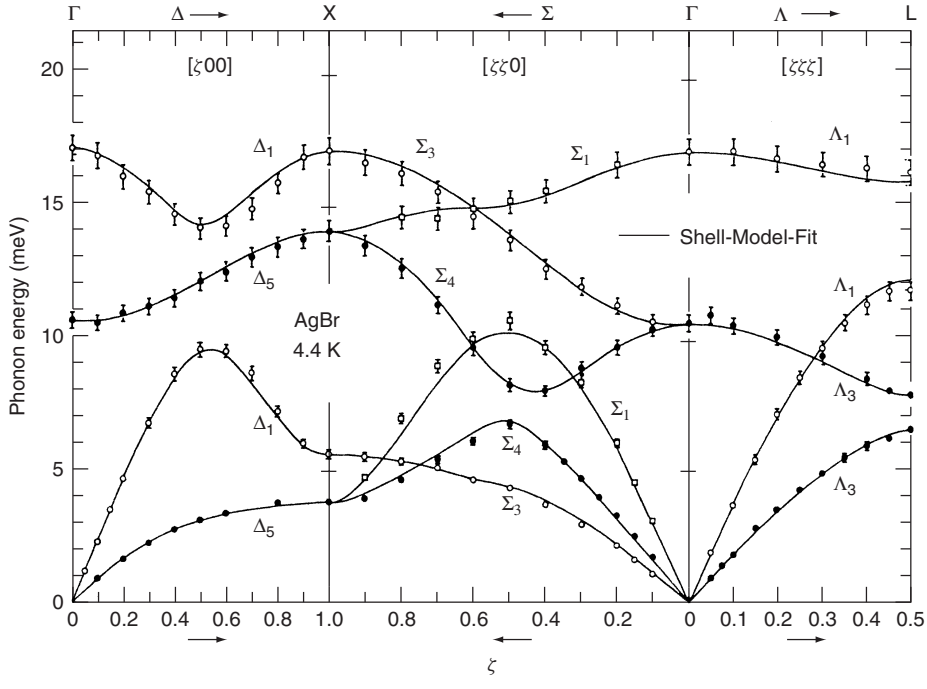

Figure W22.6. Phonon dispersion curves for AgBr at $T = 296$ K measured by neutron scattering. [From Y. Fujii et al, Phys. Rev. B, **15**, 358 (1977). Copyright 1977 by the American Physical Society.]

the *dynamical structure factor*) of the form

$$S(\mathbf{Q}, \omega) = e^{-2W} \sum_{\text{type},\mathbf{Q}} |M(\mathbf{Q})|^2 \, [[n(\mathbf{Q}, T) + 1]\delta(\omega + \omega(\mathbf{Q})) + n(\mathbf{Q}, T)\delta(\omega - \omega(\mathbf{Q}))], \tag{W22.43}$$

where M is a matrix element describing the coupling of the neutron to the particular excitation and is defined in terms of the energy transfer:

$$\hbar\omega = \frac{\hbar^2 k'^2}{2M_n} - \frac{\hbar^2 k^2}{2M_n}. \tag{W22.44}$$

The sum over "types" includes the various branches of the phonon spectrum (TA, LA, TO, LO) as well as magnons, if they are present.

If the energy of the neutrons is sufficiently high, it is also possible to have emission or absorption of more than one elementary excitation. Thus two-phonon, three-phonon,... processes are possible.

In summary, neutron scattering provides the means to measure the dispersion curves of the low-energy elementary excitations of the crystal. An example of a set of such curves is given in Fig. W22.6, where data for AgBr are presented along principal symmetry directions of the reciprocal lattice.

OPTICAL SPECTROSCOPY

In the following sections various optical methods to acquire information about solids are explored. First, optical spectroscopy is discussed for electromagnetic radiation in the infrared, visible, and ultraviolet regions of the spectrum. The solid is excited from its ground state to some excited state and information concerning such transitions may be obtained from the reflectance or transmittance. This is followed by a discussion of ellipsometry, which provides a technique for systematically mapping out the electromagnetic properties of materials by examining the reflected light. The methods of Fourier transform infrared spectroscopy and Raman spectroscopy provide complementary techniques for further characterizing the bulk of materials in the infrared. Luminescence provides additional information about the excited states of the solid as they relax toward lower-energy states by radiative emission. Finally, nonlinear optical spectroscopy provides important information on how strong electromagnetic fields interact with solids.

W22.6 Optical Spectroscopy in the Infrared, Visible, and Ultraviolet

The propagation of light through a material is governed by a complex index of refraction $\tilde{n}(\omega) = n(\omega) + i\kappa(\omega)$. The real part of this index determines the speed of propagation through the medium

$$v = \frac{c}{n(\omega)}. \tag{W22.45}$$

The imaginary part determines the absorption coefficient that appears in the law of attenuation, Beer's law:

$$\frac{I(x)}{I_0} = \exp[-\alpha(\omega)x]. \tag{W22.46}$$

Here $I(x)/I_0$ is the fraction of the initial light intensity entering the material that remains after traversing a distance x and

$$\alpha(\omega) = 2\frac{\omega}{c}\kappa(\omega). \tag{W22.47}$$

One of the central goals of solid-state physics over the years has been to try to explain the optical properties of materials in terms of the response of the electrons and the lattice.

The index of refraction is measured directly using a reflectance apparatus. The reflection coefficient, R, is the ratio of the reflected intensity to the incident intensity and is given, for the case of normal incidence on a thick sample [see Eq. (8.16)], by

$$R(\omega) = \frac{[n(\omega) - 1]^2 + [\kappa(\omega)]^2}{[n(\omega) + 1]^2 + [\kappa(\omega)]^2} \tag{W22.48}$$

(For thin samples the expression is more complicated due to interference effects caused by reflection from the back surface of the film.) Selected data for $n(\omega)$ and $\kappa(\omega)$ for the semiconductor GaAs are shown in Fig. W22.7. There is a sharp electronic band-edge apparent at ≈ 1 μm and a sharp optical-phonon resonance at ≈ 30 μm.

In attempting to understand the optical properties, the various contributions to the index of refraction need to be identified. These include the effect of optical phonons, conduction electrons, interband transitions, and excitons, as well as trapped electrons. These effects are studied in Chapter 8.

Typical ionic vibrational frequencies lie in the infrared region of the spectrum, and this is true for the phonons as well. From Chapter 8 the optical-phonon contribution to the complex index of refraction is given by the formula

$$[n(\omega) + i\kappa(\omega)]^2 = \epsilon_r(\infty)\left(1 + \frac{\omega_L^2 - \omega_T^2}{\omega_T^2 - \omega^2 - i\omega\gamma}\right). \tag{W22.49}$$

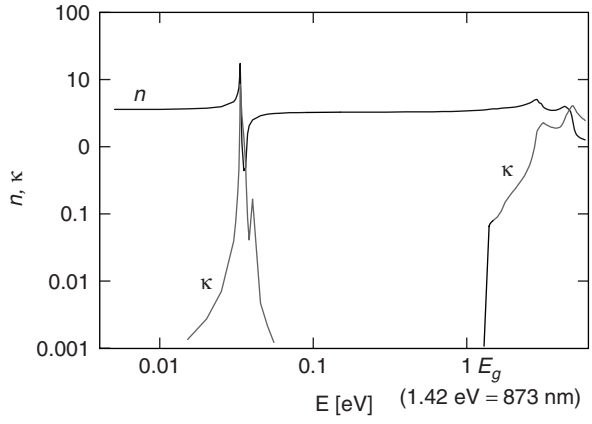

Figure W22.7. Optical constants n and κ for GaAs as a function of energy E. (Data taken from D. E. Aspnes and A. A. Studna, *Optical Constants of Solids*, E. D. Palik, ed., Academic Press, San Diego, Calif., 1985).

For GaAs the fit is made to the infrared spectrum and the fitting parameters are $\overline{\nu}_L = 292\ \text{cm}^{-1}$, $\overline{\nu}_T = 269\ \text{cm}^{-1}$, $\epsilon_r(\infty) = 11.0$, and $\gamma = 2.4\ \text{cm}^{-1}$, where $\omega = 2\pi\overline{\nu}c$.

In the case of a metal, one must take into account the plasma oscillations in describing the optical region of the spectrum, as in Section 8.4. The index of refraction would then be given by

$$[n(\omega) + i\kappa(\omega)]^2 = \epsilon_r(\infty)\left[1 - \frac{\omega_p^2}{\omega(\omega + i/\tau)}\right], \tag{W22.50}$$

where the plasma frequency is given by [see Eq. (8.11)]

$$\omega_p = \sqrt{\frac{ne^2}{m\epsilon(\infty)}}. \tag{W22.51}$$

This is often used to fit the dielectric function in the region of the plasma resonance. The lifetime τ is determined by the collisions of the electrons within a given band with phonons (intraband transitions).

Other channels for absorption open when the photon energy is larger than the gap between an occupied and an unoccupied band. A semiconductor is a case in point. When the photon energy exceeds the bandgap, electrons may be excited from the top of the valence band to the bottom of the conduction band. If these extrema coincide in **k** space, the transition is called direct. If not, phonon emission or absorption can make up for the momentum mismatch and the transition is called indirect. One therefore finds a sharp increase in $\kappa(\omega)$ when the photon energy exceeds the bandgap. The functional form depends on the density of states in the two bands. To the extent that the smooth variation of the radiation matrix elements are neglected, $\kappa(\omega)$ is proportional to

$$\kappa(\omega) \approx \int_{-\infty}^{\mu} dE\,\rho_v(E)\rho_c(E + \hbar\omega). \tag{W22.52}$$

Thus it is given by the joint density of states between the valence band (v) and the conduction band (c).

If excitons are present, then, as seen in Section 8.10, sharp absorption lines are observed below the bandgap energy. These correspond to the energy of the formation of the exciton (bandgap energy less the binding energy) and of its excited states.

One may also liberate electrons trapped in impurity levels by photon absorption and monitor their presence by studying the behavior of $\kappa(\omega)$ below the energy gap.

The chemical composition of a solid may readily be determined by sputtering excited atoms from the surface. The resulting atomic emission lines are identified using a monochromator and photodetector. The technique is called *atomic-emission spectrometry*. Typically, a beam of high-energy argon ions is used for the excitation. Before an accurate quantitative analysis may be made, however, one must know the sputtering and excitation probabilities for the individual atoms when subjected to the argon ions at a given energy. These may be obtained from sputtering experiments using samples with predetermined compositions.

It is also possible to look at the atomic absorption spectrum of the resulting plasma to obtain a quantitative analysis. The technique is then called *atomic-absorption spectrometry* (AAS).

Other methods, beside Ar^+ ion bombardment, are available for producing sputtering, including laser irradiation, electric arcs, and electron-stimulated desorption (ESD).

W22.7 Ellipsometry

Ellipsometry provides a means for characterizing the optical properties of solids, interfaces, thin films, and multilayers. The method employs polarized monochromatic light which is reflected from the surface and analyzed. A typical experimental apparatus with an arrangement referred to as the *PCSA geometry* is depicted in Fig. W22.8. A collimated light beam, with wave vector **k**, passes through a polarizer P, and a compensator C, is obliquely reflected from a sample S, passes through an analyzer A, and the beam is finally detected with wave vector $\mathbf{k}''$. The angle of incidence (and reflection) is ϕ.

Two basis states of the polarization geometry are shown in Fig. W22.9. The polarization plane is defined as the plane containing the vectors **k** and $\mathbf{k}''$ and it also contains the normal to the solid surface, $\hat{n}$. In the *p*-polarization case the incident and reflected electric field vectors, **E** and $\mathbf{E}''$, lie in the polarization plane, as shown in Fig. W22.9*a*. In the *s*-polarization case, shown on the right, the electric field vectors are perpendicular

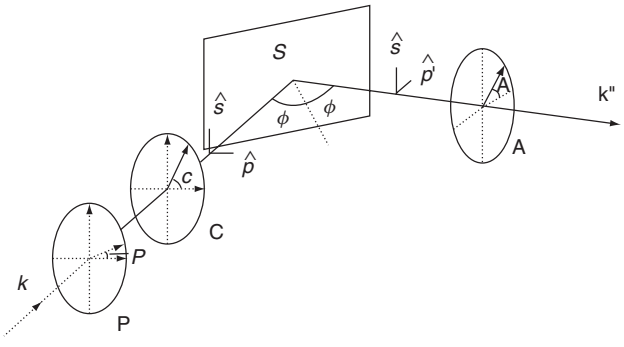

Figure W22.8. Geometry of an ellipsometry experiment.

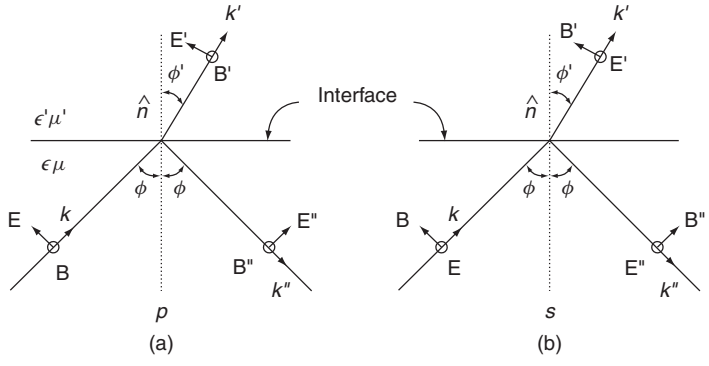

Figure W22.9. Electric and magnetic fields for the (*a*) *p*-polarization and (*b*) *s*-polarization cases. (Adapted from J. D. Jackson, *Electrodynamics*, 2nd ed., Wiley, New York, 1975, Figs. 7.6 and 7.7.)

to the polarization plane. The unit basis vectors shown in Fig. W22.8, $\hat{s}$, $\hat{p}$, and $\hat{p}'$, are appropriate for expressing the incident and reflected fields. The electric permittivity of the solid, ϵ', will be a complex function of frequency, in general.

After passing through the polarizer, whose polarization axis makes an angle P with the polarization plane, the electric field is $\mathbf{E}_1 = E_0(\hat{p}\cos P + \hat{s}\sin P)$. The compensator has a polarization axis defined by the unit vector $\hat{C}$, making an angle C with the polarization plane. It has different transmittance for electric fields along $\hat{C}$ and perpendicular to $\hat{C}$. It may be described by the transmittance dyadic $\overleftrightarrow{T} = T_\parallel \hat{C}\hat{C} + T_\perp(\overleftrightarrow{I}_2 - \hat{C}\hat{C})$, where the two-dimensional unit dyadic may be expressed as $\overleftrightarrow{I}_2 = \hat{p}\hat{p} + \hat{s}\hat{s}$. The field emerging from the compensator is

$$\begin{aligned}\mathbf{E} &= [T_\parallel \hat{C}\hat{C} + T_\perp(\overleftrightarrow{I}_2 - \hat{C}\hat{C})] \cdot \mathbf{E}_1 \\ &= E_0\{[(T_\parallel - T_\perp)\cos(P-C)\sin C + T_\perp \sin P]\hat{s} \\ &\quad + [(T_\parallel - T_\perp)\cos(P-C)\cos C + T_\perp \cos P]\hat{p}\}. \end{aligned} \tag{W22.53}$$

The ratio of E_s to E_p may be written as

$$\frac{E_s}{E_p} = \frac{\tan C + \rho_c \tan(P-C)}{1 - \rho_c \tan C \tan(P-C)} \tag{W22.54}$$

where $\rho_c \equiv T_\perp / T_\parallel$. In the case where the compensator is a quarter-wave plate one has $\rho_c = i = \sqrt{-1}$.

By matching boundary conditions for plane-wave reflection and transmission at the interface, Fresnel derived expressions for the reflection coefficients for the amplitudes of p- and s-polarized light. For the case of reflection from a semi-infinite solid, Fresnel found that (Jackson, 1975, Sec. 7.3)

$$r_s = \frac{\tilde{n}\cos\phi - \sqrt{\tilde{n}'^2 - \tilde{n}^2\sin^2\phi}}{\tilde{n}\cos\phi + \sqrt{\tilde{n}'^2 - \tilde{n}^2\sin^2\phi}}, \tag{W22.55a}$$

$$r_p = \frac{\tilde{n}'^2\cos\phi - \tilde{n}\sqrt{\tilde{n}'^2 - \tilde{n}^2\sin^2\phi}}{\tilde{n}'^2\cos\phi + \tilde{n}\sqrt{\tilde{n}'^2 - \tilde{n}'^2\sin^2\phi}}, \tag{W22.55b}$$

where it is assumed that the magnetic permeabilities are equal (i.e., $\mu' = \mu$). In the general case, either $\tilde{n}$ or $\tilde{n}'$, the indices of refraction for the incident and reflecting media, respectively, may be complex functions of frequency. In the case where light is incident from vacuum, $\tilde{n} = 1$.

The reflected wave is given by $\mathbf{E}'' = (r_p \hat{p}'\hat{p} + r_s \hat{s}\hat{s}) \cdot \mathbf{E}$, that is,

$$\mathbf{E}'' = E_0(x_s \hat{s} + x'_p \hat{p}'), \tag{W22.56}$$

where

$$x_s = r_s[(T_\parallel - T_\perp)\cos(P-C)\sin C + T_\perp \sin P] \equiv |x_s| e^{i\Delta_s}, \tag{W22.57a}$$

$$x_{p'} = r_s[(T_\parallel - T_\perp)\cos(P-C)\cos C + T_\perp \cos P] \equiv |x_{p'}| e^{i\Delta_{p'}}. \tag{W22.57b}$$

The ratio $(E_{p'}/E_s)_{\text{out}}$ is often expressed as

$$\left(\frac{E_{p'}}{E_s}\right)_{\text{out}} = \frac{x_{p'}}{x_s} \equiv \tan\psi e^{i\Delta}, \tag{W22.58}$$

where $\Delta = \Delta_{p'} - \Delta_s$.

After emerging from the analyzer, which makes an angle A with the polarizing plane, the electric field is $\mathbf{E}_{\text{out}} = \hat{A}\hat{A} \cdot \mathbf{E}''$. The intensity of the outgoing light is proportional to $|\mathbf{E}_{\text{out}}|^2$,

$$I(A) = I_0(1 + \alpha\cos 2A + \beta\sin 2A), \tag{W22.59}$$

where $I_0(\propto |E_0|^2)$ is the mean intensity amplitude,

$$\alpha = \frac{|x_{p'}|^2 - |x_s|^2}{|x_{p'}|^2 + |x_s|^2} = \frac{\tan^2\psi - 1}{\tan^2\psi + 1}, \tag{W22.60a}$$

$$\beta = \frac{2|x_{p'}||x_s|\cos\Delta}{|x_{p'}|^2 + |x_s|^2} = \frac{2\tan\psi\cos\Delta}{\tan^2\psi + 1}. \tag{W22.60b}$$

Solving for ψ and Δ gives

$$\psi = \tan^{-1}\left(\sqrt{\frac{1+\alpha}{1-\alpha}}|\tan P|\right), \qquad 0 \le \psi \le \pi/2, \tag{W22.61a}$$

$$\Delta = \pm\cos^{-1}\left(\sqrt{\frac{\beta^2}{1-\alpha^2}}\right), \qquad -\pi < \Delta \le \pi. \tag{W22.61b}$$

By fitting $I(A)$ expressed by Eq. (W22.59) to the measured data, values for α and β may be determined. One may then adjust the real and imaginary parts of $\tilde{n}' = n' + i\kappa'$ to obtain an optimum fit to the measured values of α and β. By carrying out this procedure as a function of photon frequency, the real and imaginary parts of the index of refraction, $n'(\omega)$ and $\kappa'(\omega)$, may be obtained.

The method is readily extended to the case where there is a film on a substrate. The dielectric properties of the film are often modeled using an effective-medium approximation. The sensitivity of ellipsometry is very high and the effects of monolayer or even submonolayer films may be detected.

The growth of an hydrogenated amorphous carbon (a-C:H) film on a Mo substrate is illustrated in Fig. W22.10, which shows the evolution of $\langle\epsilon_1\rangle$ and $\langle\epsilon_2\rangle$, the real and imaginary parts of the pseudodielectric function $\langle\epsilon_r\rangle$. The pseudodielectric function corresponds to a hypothetical uniform and isotropic material with a clean and abrupt surface boundary that gives the same ellipsometric data as the actual sample being studied.[†] The start point corresponds to the bare Mo substrate and the end point to $a \approx 123$ nm thick a-C:H film. The evolution of $\langle\epsilon_1\rangle$ and $\langle\epsilon_2\rangle$ has been modeled in

[†] D. E. Aspnes, *Thin Solid Films*, **89**, 249 (1982).

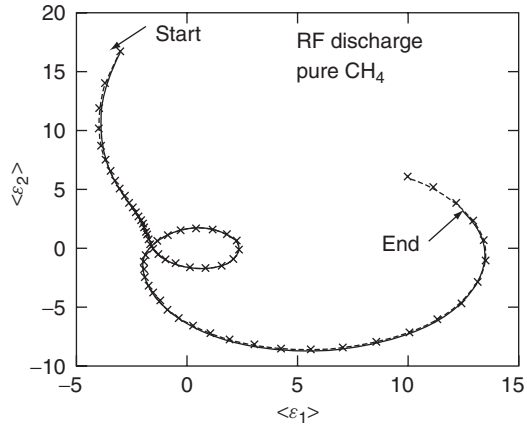

Figure W22.10. Pseudodielectric function for a-C:H film growth on Mo. "START" refers to a bare Mo substrate and "END" to a film of 123 nm covering the substrate. [From R. W. Collins, *Appl. Phys. Lett.*, **52**, 2025 (1988). Copyright 1988, American Institute of Physics.]

this case by the layer-by-layer growth of a uniform a-C:H film with $\epsilon_1 = 2.84$ and $\epsilon_2 = 0.425$ at $\lambda = 388$ nm.

W22.8 Fourier Transform Infrared Spectroscopy

It is possible to measure the entire infrared-transmission spectrum of a solid at one time using Fourier transform infrared spectroscopy (FTIR). The method is not limited to the infrared or to absorption spectroscopy, although it is often used there. The technique makes use of an interferometer with a moving mirror. The technique is to create a replica of the infrared spectrum at much lower frequencies and to make the measurements there.

The interferometer is illustrated in Fig. W22.11. Broadband infrared radiation $E_0(\omega)$ (usually blackbody radiation) is produced by a filament or globar O and is directed toward a "half-silvered" mirror *m*. The beam is split into two parts, each one traveling along a different arm of the interferometer. The first beam strikes mirror M and the second beam strikes the moving mirror M′. The beams are recombined at

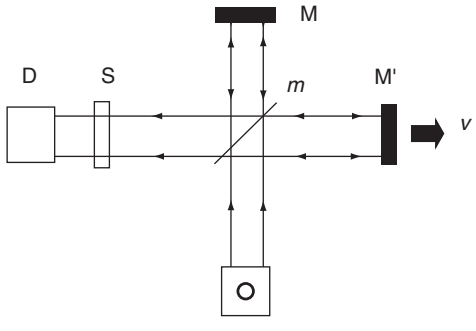

Figure W22.11. FTIR apparatus showing the interferometer.

the "half-silvered" mirror, are directed through sample S, and are finally detected at detector D (usually, a bolometer). A recording is made of the intensity as a function of time, which is then Fourier analyzed.

Let d be the distance from m to mirror M and $d' + vt$ be the distance from m to mirror M′. The amplitude of the recombined wave is the superposition of the amplitudes of the two beams

$$E(t) = \frac{E_0(\omega)}{2} \exp(2ikd) + \frac{E_0(\omega)}{2} \exp[2ik(d' + vt)]. \tag{W22.62}$$

The intensity incident on the sample is proportional to the absolute square of E. The detected intensity is

$$I(t) = 2 \int_0^\infty d\omega I_0(\omega) T(\omega) \left[1 + \cos\left(2\frac{\omega}{C}(d' - d + vt)\right)\right]. \tag{W22.63}$$

where $I_0(\omega) = |E_0(\omega)|^2$, $T(\omega)$ being the transmission coefficient for the sample. Now take the Fourier transform of this to obtain

$$\begin{aligned} I(\Omega) &= \int_{-\infty}^{\infty} \frac{dt}{2\pi} I(t) \exp(i\Omega t) \\ &= \int_0^\infty d\omega I_0(\omega) T(\omega) \left[2\delta(\Omega) + \delta\left(\Omega - 2\frac{v}{c}\omega\right) \exp(i\eta)\right. \\ &\quad \left. + \delta\left(\Omega + 2\frac{v}{c}\omega\right) \exp(-i\eta)\right], \end{aligned} \tag{W22.64}$$

where $\eta = 2\omega(d - d')/c$. Focusing attention on the resonant (second) term and computing its amplitude gives

$$|I(\Omega)| \simeq \frac{c}{2v} I_0\left(\frac{c}{2v}\Omega\right) \left|T\left(\frac{c}{2v}\Omega\right)\right|. \tag{W22.65}$$

In the ideal case, since the blackbody spectrum is known, the functional dependence of $I_0(\omega)$ is known. Therefore, a measurement of $I(\Omega)$ permits the determination of $|T(c\Omega/2v)|$. Since v will typically be on the order of 1 mm/s, the ratio $c/2v$ will be 1.5×10^{11}. Thus a measurement in the frequency range of $\Omega \approx 1$ kHz is used to determine the spectrum in the range of 10^{14} Hz! A replica of the infrared spectrum has been produced at low frequencies.

In reality, the situation is more complicated, since the source is not a blackbody. Usually, a baseline spectrum is taken without a sample. In this way the output can be normalized to the response of the system, including the source spectrum and detector sensitivity.

FTIR permits one to obtain data simultaneously over a large frequency range and over a large collection angle. Multiple scans are used to improve the signal-to-noise ratio. The technique is readily extended to other forms of spectroscopy, such as Raman spectroscopy.

The FTIR spectrum for diamond is presented in Fig. W22.12. The spectrum clearly shows various critical points and combinations of critical points in the phonon spectrum.

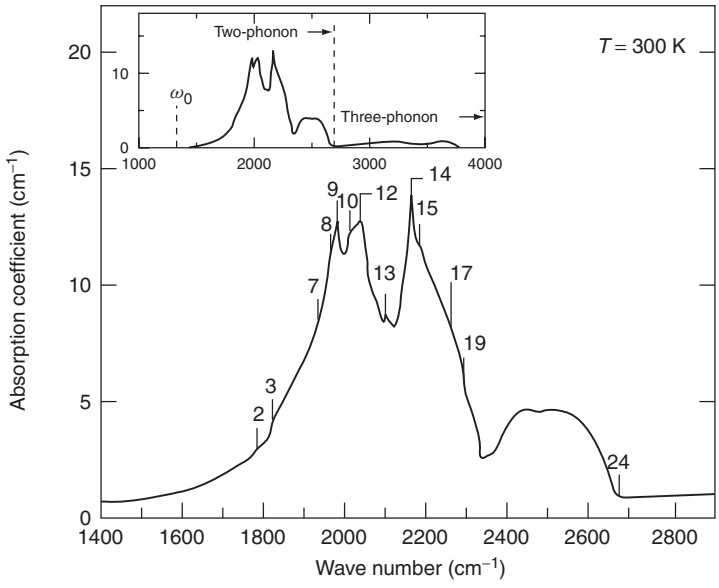

Figure W22.12. FTIR spectrum for diamond at $T = 300$ K. [From R. Vogelgesang et al., *Phys. Rev. B*, **58**, 5408 (1998). Copyright 1998 by the American Physical Society.]

This spectrum may also be contrasted with the Raman spectrum given in the following section. The spectrum should be compared with the phonon density of states presented in Fig. 5.9.

W22.9 Raman Spectroscopy

The Raman effect was originally discovered in molecular physics. Monochromatic light of frequency ω was directed at a gas sample, and the scattered light was passed through a monochromator and onto a photodetector. The scattered light consisted mainly of radiation at frequency ω (Rayleigh scattering), but also possessed sidebands at lower (Stokes shifted) and higher (anti-Stokes shifted) frequencies. The displacement of the sidebands is characteristic of the type of molecule under study and is related to the vibrational frequencies associated with nuclear motion. The angular momentum selection rules $\Delta J = 0, \pm 2$ are obeyed, where J is the total angular momentum, consistent with what is expected for scattering of a spin 1 particle, the photon. This differs from the absorption case where the selection rules are $\Delta J = 0, \pm 1$.

A simple classical theory provides a heuristic explanation of the effect, although a quantum-mechanical treatment is required to understand the effect quantitatively. Let the molecule be described by a polarizability tensor $\overleftrightarrow{\alpha}$, defined in Chapter 8. Incident light provides an electric field with amplitude E_0, which induces an oscillating electric dipole

$$\boldsymbol{\mu} = \overleftrightarrow{\boldsymbol{\alpha}}(\omega) \cdot \mathbf{E}_0 \exp(-i\omega t). \tag{W22.66}$$

This dipole will radiate in accordance with the Larmor radiation formula. The energy emitted per frequency interval $d\omega$ is

$$U(\omega) = \frac{\omega^4}{12\pi\epsilon_0 c^3} |\overleftrightarrow{\alpha}(\omega) \cdot \vec{E}_0|^2. \tag{W22.67}$$

This is elastically scattered light and is called *Rayleigh scattering*. Now suppose that the molecule is allowed to vibrate in a particular normal mode with a vibrational frequency Ω (which is much less than ω). The polarizability tensor will also fluctuate at this frequency. Let Q be the normal-mode coordinate displacement associated with Ω. Then, to a first approximation,

$$\boldsymbol{\alpha}(\omega, t) = \boldsymbol{\alpha}_0(\omega) + \frac{\partial \boldsymbol{\alpha}(\omega)}{\partial Q} Q \cos \Omega t. \tag{W22.68}$$

The oscillating dipole now produces sidebands at frequencies $\omega + \Omega$ and $\omega - \Omega$, in addition to the oscillation at ω. The emission at these frequencies constitutes the Raman anti-Stokes and Stokes radiation, respectively. Rayleigh scattering occurs at frequency ω.

In the quantum-mechanical description the molecule is originally in the ground-electronic state in some vibrational state, and the light causes it to make a virtual transition to an excited-electronic state. This is followed by the molecule radiating a photon and falling into any vibrational state associated with the ground-electronic state. If the state happens to be the original one, it produces Rayleigh scattering. If it is to a higher-energy state, it is Stokes Raman scattering, whereas if it is to a lower-energy state, it is anti-Stokes Raman scattering. In Raman scattering the outgoing photon is either lowered in energy or raised in energy by the vibrational quantum $\hbar\Omega$. In order for anti-Stokes scattering to occur, there must be population in the excited vibrational state to begin with, which arises from thermal excitation. Stokes scattering can always occur. The ratio of the anti-Stokes to the Stokes scattering is given by the Boltzmann factor:

$$\frac{I_{\text{anti-Stokes}}}{I_{\text{Stokes}}} = \exp\left(-\frac{\hbar\Omega}{k_B T}\right). \tag{W22.69}$$

Raman scattering is useful in condensed matter physics and chemistry in several instances. In solids the vibrational motions of the molecules are coupled and the excitations spread out in energy. In crystals they assume the character of phonons and are delocalized over the entire crystal. In highly disordered materials they may remain as localized oscillations extending over many nearby neighbors. The phonons may be categorized as being optical or acoustic. Raman scattering from the acoustic phonons is called *Brillouin scattering*.

For example, consider the scattering by conduction electrons in a lightly n-doped semiconductor. An electron may be virtually excited to some higher energy band and then reemit a different photon in returning to the original band. However, the wave vector of the photon is small compared with the size of the Brillouin zone. Therefore, there cannot be much of a change in the wave vector of the electron. It could emit an optical phonon with $\mathbf{k} = 0$, selection rules permitting. It could also produce Brillouin scattering. If anharmonic effects are taken into account, however, terms involving the simultaneous excitation of two phonons are also present. In terms of the simple classical model introduced earlier,

$$\boldsymbol{\alpha}(t) = \boldsymbol{\alpha}_0(\omega) + \sum_{i=1}^{2} \frac{\partial \boldsymbol{\alpha}(\omega)}{\partial Q_i} Q_i \cos \Omega_i t + \frac{1}{2} \sum_{ij} \frac{\partial^2 \boldsymbol{\alpha}(\omega)}{\partial Q_i \partial Q_j} Q_i \cos \Omega_i t Q_j \cos \Omega_j t. \tag{W22.70}$$

Sidebands now include terms with frequencies $\omega - \Omega_1 - \Omega_2$, among others. Extending this concept to solids implies that two-phonon production is possible. The net wave vector carried off by a pair of optical phonons may be small (i.e. $\mathbf{k}_1 + \mathbf{k}_2 = 0$). Thus light is able to create such a state with little momentum transfer.

Surface-enhanced Raman scattering (SERS) has emerged as a powerful tool for studying adsorbed species on the surfaces of solids. The Raman cross section for adsorbed species is found to be enhanced by as much as six orders of magnitude over the gaseous cross sections. Much of this enhancement is due to the increase in the strength of the local electromagnetic field at the surface over its value in free space. The amplification occurs because of local surface roughness, which creates miniature "lightning rods," and also because of particular electronic resonances of the solid, such as surface plasmons. At frequencies approaching these resonances the surface acts as a high-Q resonator and has high-frequency (ac) electric fields due to the incident and outgoing radiation. There is also considerable evidence that the formation of the chemical bond between the adsorbed molecule and the substrate enhances the value of the Raman tensor, $\partial\alpha/\partial Q$.

An example of a Raman spectrum is given in Fig. W22.13. The intensity of the Raman scattering for diamond is plotted as a function of the frequency shift (in wave numbers). The Raman spectrum may be contrasted with the infrared absorption spectrum given in Fig. W22.12. The Raman spectrum is due to both a single-phonon process at ω_0 (as shown in the inset to Fig. W22.13) and to much weaker two-phonon processes. The one-phonon Raman peak at $\omega_0 = 1332.4$ cm^{-1} corresponds to the zone-center optic mode at $\approx 2.5 \times 10^{14}$ rad/s of Fig. W22.12. Note that Raman scattering

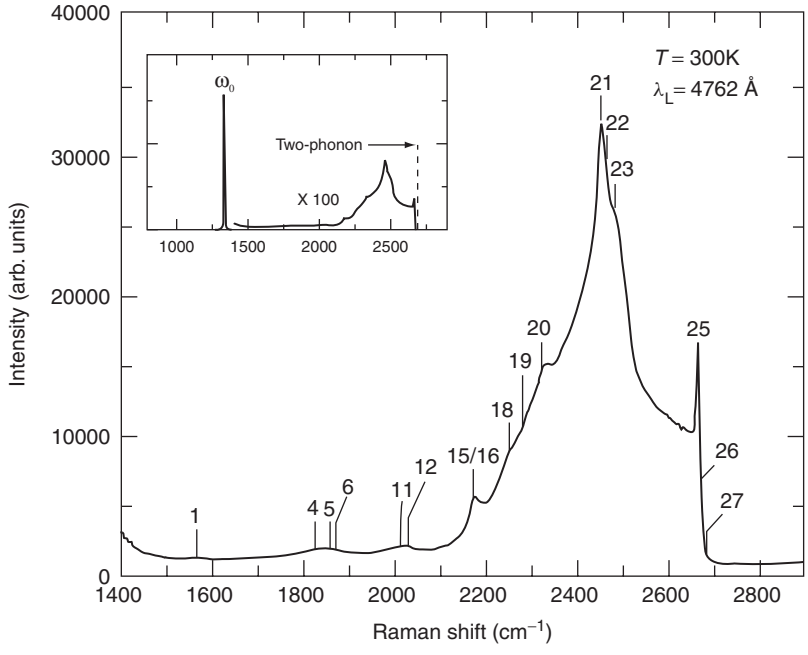

Figure W22.13. Raman spectrum for diamond at $T = 300$ K. The incident light is polarized in the (111) plane. The backscattered light is in the [111] direction. [From R. Vogelgesang et al., *Phys. Rev. B*, **58**, 5408 (1998). Copyright 1998 by the American Physical Society.]

provides a much higher precision measurement of mode frequencies than does neutron scattering. See also Fig. 11.21, which gives a Raman spectrum for a Si–Ge alloy.

W22.10 Luminescence

Light is absorbed by materials and a fraction of the light is reemitted, usually with photons of lower frequencies. The process is called *luminescence*. The light may come out promptly, on a time scale of the order of a nanosecond, in which case the process is called *fluorescence*. It may come out on a much longer time scale, in which case it is called *phosphorescence*. Just how much light comes out depends on the nature of the competing channels for nonradiative decay. The quantum efficiency for luminescence may be defined as the ratio of the number of output photons per unit time to the number of input photons per unit time:

$$\eta = \frac{\dot{N}_{\text{output}}}{\dot{N}_{\text{input}}} \times 100\%. \tag{W22.71}$$

In metals, where the excitation of electrons–hole pairs requires no activation energy, the nonradiative decay mechanism is probable and the quantum efficiency is very small. In semiconductors, where there is a substantial energy gap, the quantum efficiency may be quite large.

In Fig. W22.14 a typical luminescence process for a semiconductor is illustrated. An incident photon is absorbed by the solid, promoting an electron from a filled valence-band state (v) to a vacant conduction-band state (c). The photon must, in most instances, have an energy that exceeds the energy gap, E_g. The notable exception is the case where excitons exist just below the bottom of the conduction band. The processes above, in which an electron jumps from one band to the other band, is called an *interband process*. A hole is left behind in the valence band. The electron is generally produced in an excited state of the conduction band. By a sequence of phonon-emission processes the electron relaxes to the bottom of the band. Similarly, the hole migrates to the top of the valence band by such intraband processes. The time scale for these transitions is typically picoseconds or less. Luminescence takes place when the electron makes a radiative-decay transition from the bottom of the conduction band to the top of the valence band. The radiative lifetime is longer than a nanosecond.

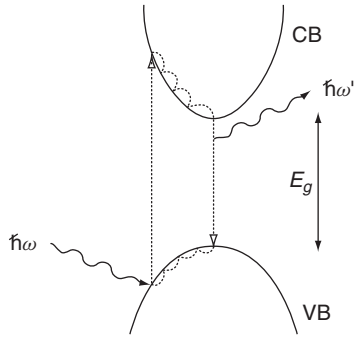

Figure W22.14. Luminescence in a direct-gap semiconductor.

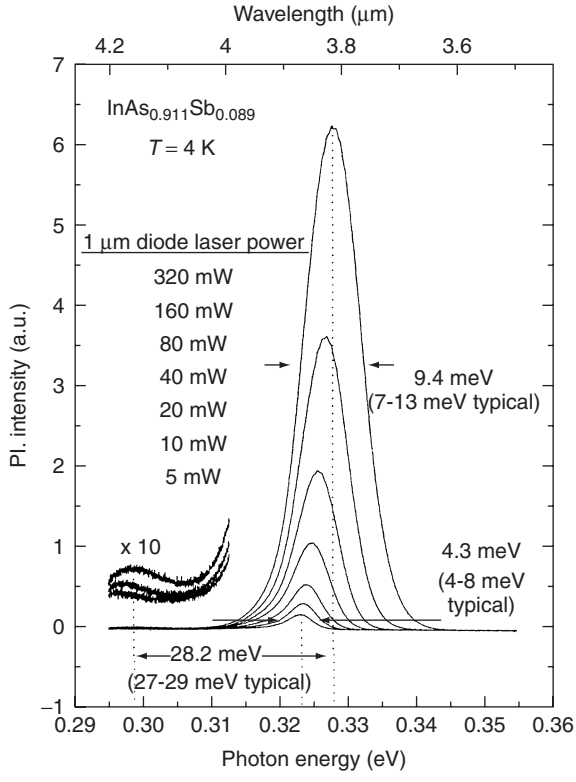

Figure W22.15. Photoluminescence spectra for MBE-grown $InAs_{0.911}Sb_{0.089}$ on a GaSb substrate at $T = 4$ K. [From M. A. Marciniak et al., *J. Appl. Phys.*, **84**, 480 (1998). Copyright 1998 by the American Institute of Physics.]

Hot luminescence occurs when the radiative recombination occurs not from the bottom of the band but from some excited state in the conduction band. If the relaxation occurs primarily with optical-phonon emission, a series of bumps will be seen in the emission spectrum, corresponding to the photon energy less some number of optical-phonon energies.

It is possible to study luminescence either in the frequency domain or in the time domain. In the latter case the procedure is called a *time-resolved luminescence study*. Luminescence may also be used to study defects. Cathodoluminescence is produced by an electron beam striking the surface of a solid.

An example of a photoluminescence spectrum is given in Fig. W22.15 for a film of $InAs_{0.911}Sb_{0.089}$ lattice-matched to a GaSb substrate. In addition to the main luminescence peak, there is a sideband lowered by the energy of a single LO phonon (≈ 28.2 meV). The narrow line width (≈ 5 meV) indicates that the material is of high quality.

W22.11 Nonlinear Optical Spectroscopy

With the advent of the laser it has become very easy to generate high-intensity electromagnetic fields. Materials no longer necessarily respond in a linear manner to

these fields, and it is important to understand their nonlinear properties. A number of phenomena are associated with nonlinear optics, such as second- and third-harmonic generation, three- and four-wave mixing, parametric excitation, self-focusing, self-phase modulation, and self-induced transparency, etc. Closely related to the pure nonlinear optical properties are the electro-optical and acousto-optical properties of materials. One is often interested in knowing how the optical properties of a material can be altered by applying electric fields or sound waves.

Attention will be focused on the polarization vector induced when an electric field exists in a medium. For a linear isotropic medium,

$$\mathbf{P}(\omega) = \epsilon_0 \chi(\omega) \mathbf{E}(\omega) \tag{W22.72}$$

where $\chi(\omega)$ is the electric susceptibility. For an anisotropic linear material the corresponding formula is [see Eq. (8.44)]

$$\mathbf{P}(\omega) = \epsilon_0 \overleftrightarrow{\chi}(\omega) \cdot \mathbf{E}(\omega) \tag{W22.73}$$

where $\overleftrightarrow{\chi}(\omega)$ is the electric susceptibility tensor. The anisotropy of this tensor is responsible for birefringence (i.e., the variation of the speed of light in a material with the polarization direction).

In nonlinear optics there are also nonlinear susceptibilities that may be defined. For example, there is the second-order susceptibility defined by [see Eq. (8.46)]

$$P_\alpha(\omega) = \epsilon_0 \sum_{\beta\gamma} \int d^{(2)}_{\alpha\beta\gamma}(\omega_1, \omega_2; \omega) E_\beta(\omega_1) E_\gamma(\omega_2)\, d\omega_1\, d\omega_2. \tag{W22.74}$$

This process describes the interaction of two photons of frequencies ω_1 and ω_2 in a material to create a photon of frequency ω. Energy conservation requires that

$$\omega_1 + \omega_2 = \omega. \tag{W22.75}$$

For this process to proceed it is also necessary to guarantee wave vector conservation, that is,

$$\mathbf{k}_1 + \mathbf{k}_2 = \mathbf{k}. \tag{W22.76}$$

This is called *phase matching*. The concept appears in Section W8.1, where the index ellipsoid is introduced. Methods for achieving phase matching in inhomogeneous media were discussed in Sections W20.6 and W20.8. Using the dispersion formula it implies that

$$\omega_1 \frac{n(\omega_1)}{c} + (\omega - \omega_1) \frac{n(\omega - \omega_1)}{c} = \omega \frac{n(\omega)}{c}. \tag{W22.77}$$

This will, in general, not be valid for arbitrary frequencies. By rotating the crystal and making use of the different indices of refraction for the ordinary and extraordinary waves, however, it is possible to achieve phase matching.

A particular application of the second-order nonlinearity is in the process of second-harmonic generation. In that case [see Eq. (8.46)]

$$P_\alpha(2\omega) = \epsilon_0 \sum_{\beta\gamma} d^{(2)}_{\alpha\beta\gamma}(\omega, \omega; 2\omega) E_\beta(\omega) E_\gamma(\omega). \tag{W22.78}$$

Depending on the symmetry of the crystal, there will only be a small number of independent components of $d^{(2)}_{\alpha\beta\gamma}$. The various components of the second-order polarization may be measured by focusing lasers of various polarizations onto a crystal volume and measuring the amount of second-harmonic light that is generated. Values for the $d^{(2)}_{\alpha\beta\gamma}$ components for various materials are given in Table 8.4.

The second-order polarizability exists only in crystals without inversion symmetry. The polarization vector **P**, being a vector, should reverse its direction under a reflection operation, as should **E**. But this is inconsistent with Eq. (W22.78), since the left-hand side changes sign but the right-hand side does not. In crystals with inversion symmetry $d^{(2)}_{\alpha\beta\gamma}$ is zero.

The third-order nonlinearity is described in terms of a fourth-order polarizability tensor defined analogously as

$$P_\alpha(\omega) = \epsilon_0 \sum_{\beta\gamma\delta} \int\int d^{(3)}_{\beta\gamma\delta}(\omega_1, \omega_2, \omega - \omega_1 - \omega_2; \omega) \times E_\beta(\omega_1) E_\gamma(\omega_2) E_\delta(\omega - \omega_1 - \omega_2)\, d\omega_1\, d\omega_2, \tag{W22.79}$$

where the phase-matching condition is

$$\mathbf{k}_1 + \mathbf{k}_2 + \mathbf{k}_3 = \mathbf{k} \tag{W22.80}$$

and energy conservation requires that

$$\omega_1 + \omega_2 + \omega_3 = \omega. \tag{W22.81}$$

The tensor $d^{(3)}_{\alpha\beta\gamma\delta}(\omega, \omega, \omega; 3\omega)$ may be determined by performing a third-harmonic generation experiment. Values for it appear in Table 8.5.

The application of an electric field to a crystal may alter the linear index of refraction of the crystal. This is of considerable technological importance since it implies that laser beams may be deflected electronically and at electronic frequencies. The degree to which the index of refraction changes when an electric field is applied to the crystal is determined by the electro-optic tensor (see Section 18.8).

The effective index of refraction for light propagating in a given direction **k** with a given polarization vector $\hat{\varepsilon}$ is defined in terms of the index ellipsoid. One constructs an imaginary ellipsoid in space (see Eq. (W8.12)]:

$$\left(\frac{x}{n_x}\right)^2 + \left(\frac{y}{n_y}\right)^2 + \left(\frac{z}{n_z}\right)^2 = 1 \tag{W22.82}$$

where x, y, and z define the coordinates in which the index of refraction tensor (related to the polarization tensor) is diagonal, and n_x, n_y, and n_z are the corresponding indices

of refraction. Draw a plane through the center of the ellipsoid perpendicular to **k**. The plane intercepts the ellipsoid in an ellipse. The length of the vector from the center of the ellipsoid to the ellipse in the direction of $\hat{\varepsilon}$ is the value of n for that light ray.

Now introduce an electric field **E**. The index ellipsoid will become stretched or compressed and will be rotated relative to the coordinates above. The new equation becomes

$$\left[\frac{1}{n^2}\right]_1 x^2 + \left[\frac{1}{n^2}\right]_2 y^2 + \left[\frac{1}{n^2}\right]_3 z^2 + 2\left[\frac{1}{n^2}\right]_4 yz + 2\left[\frac{1}{n^2}\right]_5 xz + 2\left[\frac{1}{n^2}\right]_6 xy = 1. \tag{W22.83}$$

The dependence of these coefficients on **E** is, for weak fields, a linear one. Thus

$$\left[\frac{1}{n^2}\right]_\alpha = \begin{cases} \dfrac{1}{n_\alpha^2} + \displaystyle\sum_{\beta=1}^{3} r_{\alpha\beta}E_\beta, & \alpha = 1, 2, 3, \quad \text{(W22.84}a\text{)} \\ \displaystyle\sum_{\beta=1}^{\beta} r_{\alpha_\beta}E_\beta, & \alpha = 4, 5, 6. \quad \text{(W22.84}b\text{)} \end{cases}$$

The electro-optic tensor coefficients $r_{\alpha\beta}$ may be measured by passing a laser beam through a crystal with various orientations, applying an electric field, and measuring the beam deflection produced.

Using similar ideas, it is possible to study the photoelastic tensor, which is a tensor describing the variation of the index of refraction when a strain is introduced.

ELECTRON MICROSCOPY

Conventional optical microscopy is limited in its ability to resolve structure smaller in size than the wavelength of visible light, λ. The Rayleigh criterion is

$$\sin\theta \approx 1.22\frac{\lambda}{d}, \tag{W22.85}$$

which relates the acceptance angle of the microscope, θ, and the distance, d, between two points that can be resolved. Since visible light has wavelengths in the range 400 to 700 nm, light cannot be used to see individual atoms, whose size is typically 0.1 nm. If electromagnetic radiation is to be used to study materials, one may improve matters in two ways. The first is to use shorter-wavelength radiation. X-rays would be ideal, since their wavelength can be chosen to be comparable to the size of an atom. Another approach is to use very fine optical fibers tapered to a "point" whose size is ≈ 10 nm and then bring this fiber close to the surface of the material to be probed. The coupling is done through the near field of the electromagnetic field. Using this technique, 10-nm resolution can be achieved simply and inexpensively. The method is called *near-field scanning optical microscopy* (NSOM).

Another approach is to use electrons instead of light. The relativistic expressions for the wavelength of an electron are

$$\lambda = \frac{h}{p} = \frac{hc}{\sqrt{E^2 - (mc^2)^2}} = \frac{hc}{\sqrt{K(K + 2mc^2)}} = \frac{hc}{\sqrt{eV(eV + 2mc^2)}}, \tag{W22.86}$$

where p is the momentum, E the total energy, K the kinetic energy, and V the potential difference through which the electron is accelerated to achieve this kinetic energy. By using 20-kV potentials, wavelengths of 0.009 nm are obtained, smaller than an atom. Thus resolution is no longer a limitation, but other factors, such as aberrations, prevent this fine resolution from being realized.

Electrons may be focused using electrostatic or magnetostatic lenses. The focal lengths of these lenses may be varied at will by changing the potentials and currents, respectively. It is therefore possible to construct electron microscopes in much the same way as optical microscopes are constructed. The main difference is that in electron microscopy the distance from the lenses to the sample is held fixed while the focal lengths are changed. In optical microscopy, of course, it is the other way around. The image in electron microscopy is usually obtained by rastering the beam across the sample and having the electrons collected by a detector. After amplification, the processed image is displayed on a fluorescent screen. High-vacuum conditions are needed for the electron beam to avoid collisions with gas molecules.

When high-energy electrons strike a material, they excite it and thereby lose energy. Bulk and surface plasmons can be excited. Interband transitions occur and electron–hole pair excitations are produced. There are also core-electron knock-out processes, which are followed by x-ray emission or Auger deexcitation. The Auger process is a multielectron process in which one electron fills an inner-shell vacancy, and one or more other electrons are ejected from the atom. Intraband transitions occur in metals. The net result is that copious amounts of secondary electrons are produced. In addition, there are backscattered primary electrons. Light may be emitted from the material when the electron–hole pairs recombine. If the sample is thin enough, a beam of electrons will be transmitted through the sample.

There are several methods for observing the sample. These include scanning-electron microscopy (SEM), transmission-electron microscopy (TEM), high-resolution transmission-electron microscopy (HRTEM), and low-energy electron microscopy (LEEM). These cases are discussed individually.

A number of typical electron micrographs using these techniques have appeared in Chapter 4. Figure 4.1*d* showed nanocrystalline diamond with a resolution of $\approx$ 100 nm. Figure 4.1*e* was a micrograph with atomic-scale resolution of the interface between crystalline Si and amorphous SiO_2. Figure 4.6 displayed nanocrystalline Au clusters embedded in an amorphous matrix. Figure 4.7 presented various morphologies of colloidal α-Fe_2O_3 particles. Figure 4.3 gave an HRTEM micrograph of a $PbTiO_3$–$SrTiO_3$ superlattice. Figure 4.9 showed the microstructure of a quasicrystal. Figures 4.20 and 4.21 presented images of a stacking fault and a twinned structure, respectively. These micrographs attest to the versatility of electron microscopy as a tool for studying the microstructure of materials.

W22.12 Scanning-Electron Microscopy

The scanning-electron microscope (SEM) collects the backscattered and secondary electrons that are emitted from the surface of the material. Typically, a focused 5-nm-diameter beam with a current of 10^{-11} A is directed at the surface and penetrates the material. At first, when the electron is moving fast, high-energy processes such as Auger excitation are possible. Secondary electrons are produced, but backscattering is improbable at first because of the small Rutherford cross sections at high energies.

Note that single electron–electron collisions will not produce backscattering, whereas electron–ion collisions will. At high energies, where core-electron knockout is possible, it will often be followed by characteristic x-ray emission. Superimposed on this will be the brehmsstrahlung spectrum due to the rapid deceleration of the electrons. The energy of the beam spreads out and is deposited over a region ≈ 1 μm into the surface.

The easiest electrons to detect are the secondary electrons because they are numerous and all of low energy. Backscattered electrons are particularly useful because the cross section for backscattering depends on the atomic number of the target, in accordance with our understanding of Rutherford scattering. Thus materials with different Z will produce different amounts of backscattering. This provides a means for contrasting one type of atom with another.

In the scanning-electron microscope, one may deflect the electron beam so that it focuses on different parts of the sample. As it rasters over the surface, one detects the electrons, optical luminescence, or x-rays emitted as a function of the position where the beam is when these are produced. This often involves the use of a scintillation counter and photomultiplier tube. The data may be processed and a visual image of

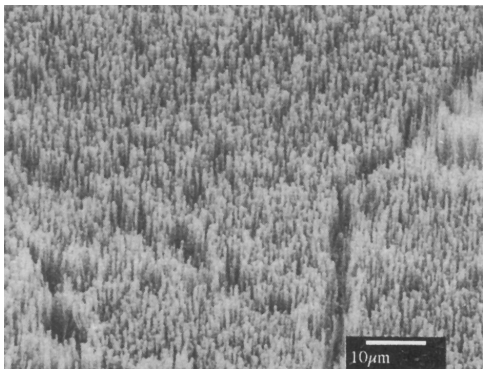

(a)

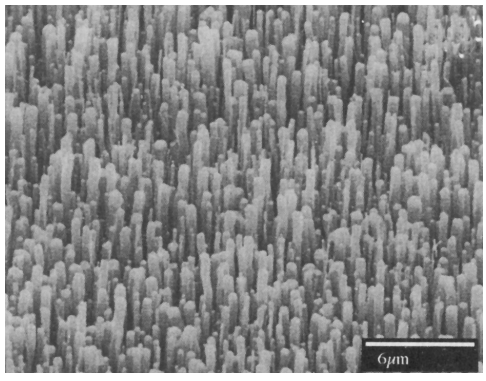

(b)

Figure W22.16. SEM micrographs of carbon nanotubes on polycrystalline Ni substrates. [From Z. P. Huang et al., *Appl. Phys. Lett.*, **73**, 3845 (1998). Copyright 1998 by the American Institute of Physics.]

the surface presented. The depth of field and magnification are controlled by varying the focal lengths. Resolutions $\approx$ 10 nm are achievable.

Instead of gathering the electrons or radiation from the incident surface of the crystal, it is also possible to use a thin film and gather them from the opposite side of the crystal. This technique is called *scanning-transmission electron microscopy* (STEM).

Figure W22.16 illustrates a scanning electron micrograph of highly oriented, multi-walled carbon nanotubes on a polycrystalline Ni substrate. The nanotubes were grown by chemical vapor deposition. It is found that growth takes place within the grain surface but not along the grain boundaries.

W22.13 Transmission-Electron Microscopy

In the transmission-electron microscope (TEM) a thin slice of the material to be studied (0.1 to 0.5 μm thick) is used and an energetic electron beam (20 to 100 keV) is passed directly through the sample. One may view either the image of the sample or the diffraction pattern that is produced on a fluorescent screen. Magnetic lenses are usually employed because it is possible to achieve short focal lengths with them. A schematic drawing of the TEM is presented in Fig. W22.17. The filament f heats the needle like cathode C, which emits electrons thermionically. The beam passes through a hole (called a *wehnelt cap*), which causes the beam to converge on and cross the optic axis (or reach some minimum spot size of radius $r_c' \approx 20$ μm for thermionic emitters). The corresponding point serves as a point source of electrons. The beam is then accelerated by an anode a and passes through a series of condenser lenses C_i and apertures A_i. It passes through a small portion of the sample and then a series of magnifying lenses M_i before it is projected on the fluorescent screen S and recorded on a photographic plate P. The sample is usually covered with a conductive coating in order to enable it to discharge electrically.

Typical cathode materials include W and LaB_6. Their work functions are 4.5 and 2.7 eV, and their operating temperatures are 2800 and $\approx$ 1700 K, respectively. In some TEMs field emitters are used instead of thermionic emitters. They make use of Fowler–Nordheim tunneling from very fine cathode tips. Materials used are W and W covered with ZrO_2. They may be operated at considerably lower temperatures, so the thermal spread of electron energies is considerably smaller than the $\approx$ 3 eV for thermionic emitters. This allows one to obtain a much better minimum spot size ($\approx$ 5 to 50 nm). Field-emission sources are brighter than thermionic sources. The respective brightnesses are typically $\approx 10^9$ and $\approx 10^{12}$ A/m$^2\cdot$ steradian. Typical vacuums for thermionic-emitter systems range from 10^{-2} to 10^{-4} Pa. For field-emitter systems ultrahigh vacuums are established, typically in the range 10^{-7} to 10^{-8} Pa.

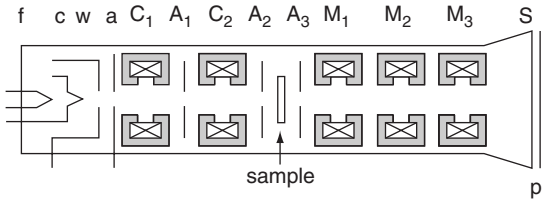

Figure W22.17. Schematic view of a transmission-electron microscope.

The focal length of a magnetic lens is given by the formula

$$\frac{1}{f} = \frac{e}{8mV} \int_{-\infty}^{\infty} B^2(z)\, dz, \tag{W22.87}$$

where $B(z)$ is the magnetic field along the axis and eV is the energy of the electron as it passes through the lens. The magnetic lens also rotates the image by an angle ϕ given by

$$\phi = \sqrt{\frac{e}{8mV}} \int_{-\infty}^{\infty} B(z)\, dz. \tag{W22.88}$$

The magnetic lenses have aberrations associated with them. These include the important spherical aberrations, chromatic aberrations, and astigmatism, as well as the less important coma and barrel or pincushion distortions. Spherical aberrations are due the fact that the rays scattered from an object point at small angles β through the lens are focused at a different image point than rays scattered at larger angles. The net result is that an object point along the axis is imaged to a disk of radius r_s rather than to a point. It may be shown that the size of this disk is given by the formula $r_s = C_s\beta^3$, where C_s is ≈ 1 mm. Unlike in the optical-lens case, there is no simple way to correct for spherical aberrations.

Chromatic aberrations are due to a variation of focal length with beam energy, and may be understood in terms of Eqs. (W22.87) and (W22.88). Inelastic losses of $\Delta V \approx 5$ to 50 eV are common for electrons passing through the sample, due to the excitation of electron–hole pairs, plasmons, phonons, and so on. The net result is that an object point is imaged to a disk-of-confusion whose radius is r_c. It may be shown that $r_c = C_c\beta\Delta V/V$, where C_c is a distance characterizing the axial variation of the magnetic field in the lens.

The imprecision with which magnetic lenses can be constructed leads to asymmetries being present. Astigmatism is caused by having a different focal length for electrons deflected in the x direction than in the y direction, the difference being Δf_A. A point source is focused to a disk of minimum size $r_A = \beta\Delta f_A$. It may usually be corrected by employing a balancing astigmatic lens.

The Rayleigh diffraction criterion gives an estimate for the minimum separation of two resolvable points, $\Delta r_d = 0.61\lambda/\beta$, where λ is the wavelength of the electrons. One may obtain an estimate for the instrument resolution by assuming that the spherical aberration and diffraction dominate. Then

$$\Delta r(\beta) = \sqrt{\left(\frac{0.61\lambda}{\beta}\right)^2 + (C_s\beta^3)^2}. \tag{W22.89}$$

There is a competition between the diffraction of the beam and the spherical aberrations of the lenses. The minimum value of Δr occurs when $\beta = (0.61\lambda/C_s\sqrt{3})^{1/4}$ and its value is $\Delta r_{\min} = 0.91C_s^{1/4}\lambda^{3/4}$. The smaller λ can be made, the better the resolution will be. Typical optimal instrumental resolutions are of the order of several tenths of a nanometer. For 100-keV beams $\Delta r = 0.33$ nm is possible, but the samples must be less than 5 nm in thickness. For 400-keV beams, a resolution of 0.17 nm has been obtained. By using beams of incoherent rather than coherent electrons and by underfocusing the

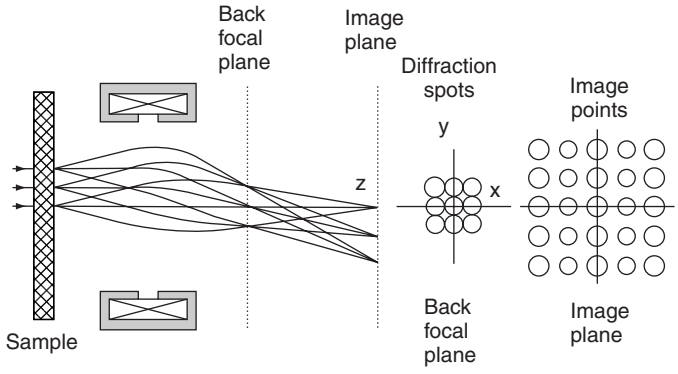

Figure W22.18. A forward-directed beam and diffracted beams are produced when the incident electron beam passes through the sample. The right figures show the diffraction spots in the back focal plane and the sample image points in the image plane.

electron beam to compensate partially for spherical aberrations, it has recently been possible to obtain 0.078-nm resolution with a 300-keV electron beam.[†]

After passing through the sample, the diffraction spots create images on the back-focal plane of the object lens (e.g., C_2 of Fig. W22.17). One may use the magnifying lenses to view this diffraction pattern directly on the screen and to produce a transmission-electron diffraction (TED) micrograph. Alternatively, a real image of the sample is produced on the image plane of the object lens. This real image may be magnified and projected on the fluorescent screen.

Emerging from the sample is both a forward-directed transmitted beam of electrons and diffracted beams of electrons, as illustrated in Fig. W22.18. The aperture A_3 of Fig. W22.17 may be used to choose one or more of these beams selectively and block the others. The technique is called *selective-area diffraction* (SAD). In the method of bright-field (BF) imaging one allows the forward-directed beam to be imaged on the screen. In the method of dark-field (DF) imaging, a diffracted beam is selected instead. The diffraction pattern in the back-focal plane and the image of the sample are depicted in the right-hand side of Fig. W22.18. The central diffraction spot corresponds to the forward-directed beam. The other spots correspond to various diffracted beams for a case where there is fourfold symmetry. As will be seen in Section W22.14, the more beams that are accepted by the aperture, the higher the resolution will be.

Kikuchi Lines. Diffraction of electrons differs from that of x-rays in two important respects. First, the samples are thin, so there are only a finite number of atomic layers, N_z, perpendicular to the beam. Second, inelastic processes are much more important for electrons than for x-rays.

Due to the finite value of $N_z(\approx 1000)$, instead of there being a pure spot diffraction pattern, the spots are elongated into streaks of length $\Delta G_z \approx 2/N_z d$, where d is the lattice spacing. Thus it is still possible to see a diffraction spot even when the von Laue condition is not exactly satisfied. One defines the mismatch reciprocal vector **s**

[†] P. D. Nellist and S. J. Pennycook, *Phys. Rev. Lett.*, **81**, 4156 (1998).

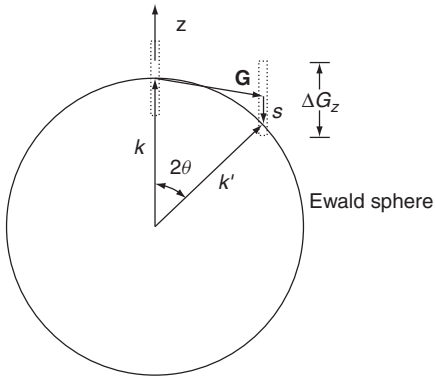

Figure W22.19. Ewald sphere and streaking of diffraction spots.

through the relation $\mathbf{k}' - \mathbf{k} = \mathbf{G} + \mathbf{s}$. This is illustrated in Fig. W22.19. The vectors $\mathbf{k}$ and $\mathbf{k}'$, making an angle 2θ with each other, have a common origin and have the same length. The head of vector $\mathbf{k}$ touches the origin of reciprocal-lattice space. The Ewald sphere passes through this origin. A diffraction spot will still be produced if the head of vector $\mathbf{k}'$ also touches the Ewald sphere, but is located a distance $s \leq \Delta G_z$ in the z direction away from the nearest reciprocal lattice point, $\mathbf{G}$. The extent of ΔG_z is denoted by the dashed rectangle in the figure.

Suppose the electron is incident on the lattice in a direction that is far removed from satisfying the von Laue diffraction condition. Electrons can suffer inelastic collisions, thereby losing energy and scattering into various directions centered around the incident direction. Energy losses of up to 50 eV are common. The probability for scattering through a given angle relative to the forward direction falls rapidly with increasing angle. An effect of this is illustrated in Fig. W22.20, where an electron suffers an inelastic collision at point p. For some scattered beams the energy and direction will be just right to satisfy the Bragg diffraction condition for a set of lattice planes. Two such planes L and L′ are illustrated in Fig. W22.20. The beams B and B′ are able

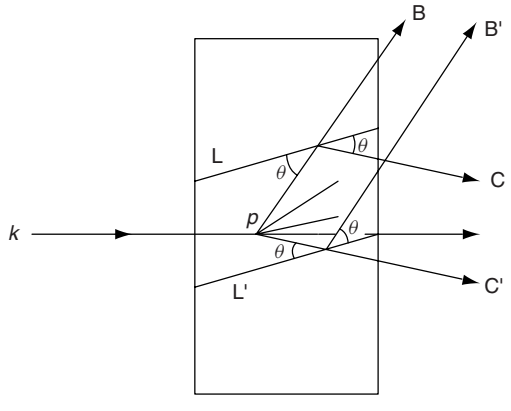

Figure W22.20. Formation of Kikuchi lines by Bragg diffraction and constructive interference of beams of inelastically scattered electrons.

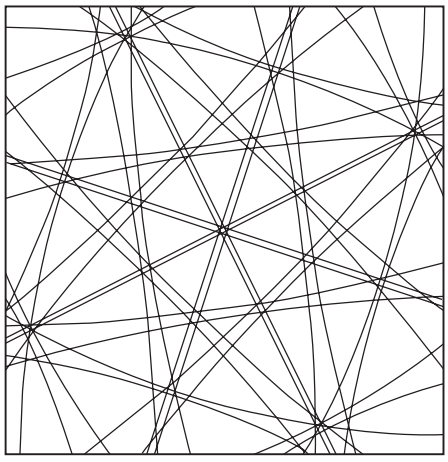

Figure W22.21. Kikuchi line pattern. (Generated using the computer program KOQUA2.2 written by S. Weber and C. Schetelich.)

to interfere with each other, as are the beams C and C′. If the Bragg condition is satisfied for the direction of beams B and B′, a bright spot will be produced in that direction. The intensity comes at the expense of radiation that was in the near-forward direction, so there will be a corresponding dark spot established along the direction of beams C and C′. The angular spread between the lines C and B is 2θ, independent of the angles through which the electrons are scattered. When one takes into account all possible angles of incidence for the electrons, the beams B and C sweep out the surfaces of cones. These cones intersect the projection of the Ewald sphere in a pair of hyperbolas. For high-energy electrons the radius of the Ewald sphere is large and it looks approximately planar. The intersections of the cones with the plane then produce a pair of approximately parallel lines. This gives rise to the *Kikuchi line pattern*. To each set of lattice planes there is a pair of Kikuchi lines, one dark and one bright. Furthermore, these lines are parallel to the intersection of the corresponding lattice planes with the Ewald sphere.

The Kikuchi line pattern shifts if the crystal is tilted. This permits one to orient a crystal precisely. An example of a Kikuchi line pattern, together with a set of diffraction spots, is illustrated in Fig. W22.21. Furthermore, at the intersection of Kikuchi lines, one finds spot patterns. Thus the Kikuchi patterns are used as maps to locate the orientations of the crystal, which give rise to diffraction-spot patterns.

W22.14 High-Resolution Transmission-Electron Microscopy

In high-resolution transmission-electron microscopy (HRTEM) a beam of high-energy electrons is passed through a thin sample and focused on an image plane. Suppose that the sample is a crystal. Recall that the diffraction condition is

$$\mathbf{G} \cdot \mathbf{k} + \frac{G^2}{2} = 0. \tag{W22.90}$$

If k is much larger than G, this equation can be satisfied only for those lattice planes whose $\mathbf{G}$ vectors are almost perpendicular to $\mathbf{k}$, for that is the only way to keep the

magnitude of the first term comparable to that of the second term. The angles between $\mathbf{k}$ and $\mathbf{k}'$ are given by

$$\sin\theta = \frac{G}{2k} \tag{W22.91}$$

and will be small.

As mentioned earlier, magnetic lenses have associated with them spherical aberrations. A beam far from the optical axis will not focus at the same point as a beam near the optical axis. In conventional microscopy, therefore, it is usually not possible to focus the Bragg-reflected beams along with the directly transmitted beam. This puts a limitation on the resolution. However, in HRTEM the Bragg peaks are coming off at small angles and therefore remain paraxial (i.e., close to the optic axes). The spherical aberrations are therefore not of major concern and it is possible to focus several Bragg orders together (Fig. W22.22).

In the figure, the sample is labeled S, the lens, L, the focal plane, F, and the image plane, I. An electron beam is incident on the sample from the left and is focused on the image plane. Note that the various Bragg-reflected beams combine with the direct beam in the image plane. This causes a sharply defined focal spot. The reason for this is that slightly away from the focal spot the various beams start to interfere with each other destructively and the intensity decays rapidly with distance away from the spot. The more diffracted beams that can be collected, the sharper the image. Once the image is formed on the image plane, further magnification is possible by the use of additional lenses, as in the case of TEM.

The angular sharpness of the image varies inversely as the number of diffracted beams in a given direction that may be focused. This is illustrated with a two-dimensional example. Consider Fig. W22.23, in which a set of N beams passes through the lens at positions y_i and is focused at the lower point on the screen. At this point all the beams arrive in phase with each other:

$$\psi = \phi_i + kl_i, \qquad i = 1, \ldots, N, \tag{W22.92}$$

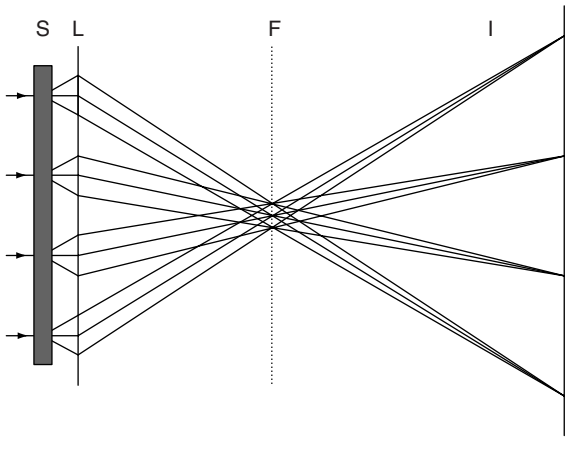

Figure W22.22. A large number of diffracted beams are focused by the lens L and are combined to form a high-resolution image of the sample S on the image plane I.

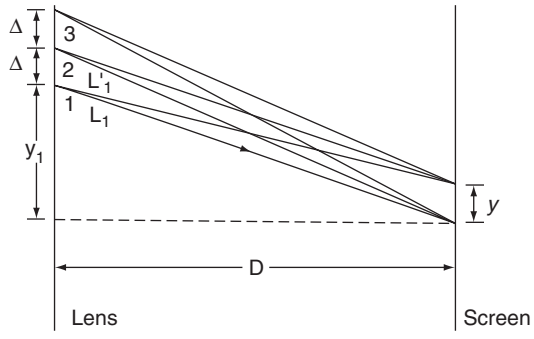

Figure W22.23. Estimation of the angular sharpness of the image.

where the $(\phi_i + kl_i)$ differ by integer multiples of 2π. The total amplitude at the point is therefore

$$A = \sum_{i=1}^{N} \exp(i\psi) = N \exp(i\psi). \tag{W22.93}$$

Next consider a point on the screen a distance y above the original point. The phase that each beam arrives with is now different:

$$\psi_i = \phi_i + k\sqrt{(y_i - y)^2 + D^2} \simeq \psi - k\frac{yy_i - y^2/2}{D}, \tag{W22.94}$$

where it is assumed that D is much larger than y_i. The amplitude at the upper point is therefore

$$A' = \sum_{n=1}^{N} \exp\left[i\psi - \frac{ik}{D}\left(yy_n - \frac{y^2}{2}\right)\right]. \tag{W22.95}$$

The points y_n on the lens are separated from each other by an arbitrary distance Δ. This amplitude will fall to zero when the phases are spread uniformly over a circle, that is, when

$$\frac{kyN\Delta}{D} = 2\pi, \tag{W22.96}$$

which shows that y is inversely proportional to N:

$$y = \frac{\lambda D}{N\Delta}. \tag{W22.97}$$

In the three-dimensional case the diffracted beams will be spread out over an area. The total number of beams will be denoted by N^2. Thus the size of the image falls off as the inverse of the square root of the number of focused diffracted beams.

It is now possible to use HRTEM to obtain spatial resolution approaching 0.1 nm, if beams of 1 MeV are used, although most conventional HRTEM applications use lower-energy beams and settle for more modest resolution goals. It is an ideal tool for studying line defects, planar defects, and interfaces.

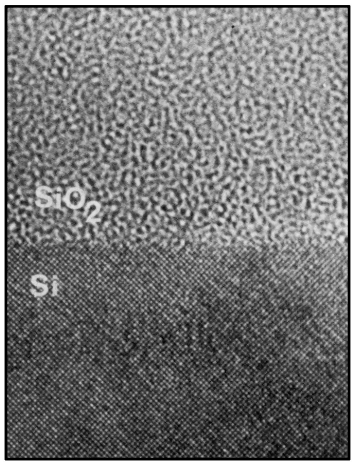

Figure W22.24. HRTEM image of the Si/a-SiO_2 interface. (From J. M. Gibson, High resolution transmission electron microscopy, *Mater. Res. Soc. Bull.*, Mar. 1991, p. 27.)

An HRTEM image of a Si/a-SiO_2 interface is shown in Fig. W22.24. The individual atoms of the Si crystal appear in the lower half of the image. The upper half shows the image of the amorphous silica.

W22.15 Low-Energy Electron Microscopy

Like LEED, low-energy electron microscopy (LEEM), involves forming a diffraction pattern using elastically scattered electrons from a crystalline surface. Unlike LEED, however, most of the pattern is discarded. Usually, one diffracted beam is extracted and imaged on a screen using conventional electron-microscope lenses. Typical energies used are in the range 100 eV to 3 keV. The resolution is as fine as 2 nm. LEEM is useful for seeing structure on a mesoscopic size scale. This includes surface steps, dislocations, imperfections, islands of adsorbates, superlattice structure, grains, and surface inhomogeneity.

In LEEM the electron beam is directed at the sample with near-normal incidence. Electrons are emitted from an electron gun from an oblique direction to the surface, and a bending magnet is used to change the direction to normal incidence. The same bending magnet is used to redirect the reflected electrons in another oblique direction toward the image plane. In Fig. W22.25 the basic imaging scheme is displayed for the case where LEEM is used to image a surface step, S, on the left. For simplicity the injection, bending magnet, and extraction are not shown, and it is simply assumed that the electron beam is incident from the right. Four reflected beams are illustrated, each with a pair of diffracted beams. The beams pass through an electron lens, L, and then through a screen, A, with an aperture in it. The aperture is placed in the focal plane of the lens. Only the specularly reflected rays are allowed through, the other diffracted beams are blocked. The rays that pass through the aperture illuminate the screen I. In passing through the aperture, the beams undergo Fresnel diffraction and are broadened into cones. Thus beam 1 is spread into cone 1, beam 2 into cone 2, and so on. The regions illuminated by these cones are denoted $1'$, $2'$, and so on.

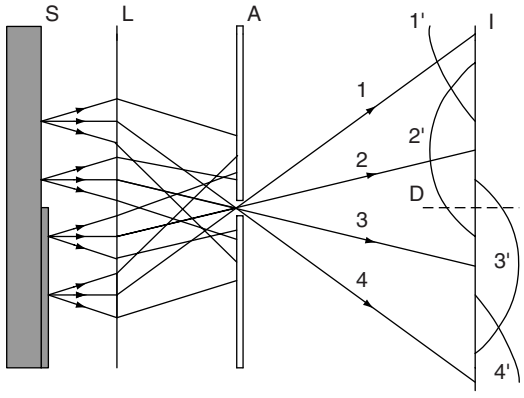

Figure W22.25. Optics of the formation of a LEEM image.

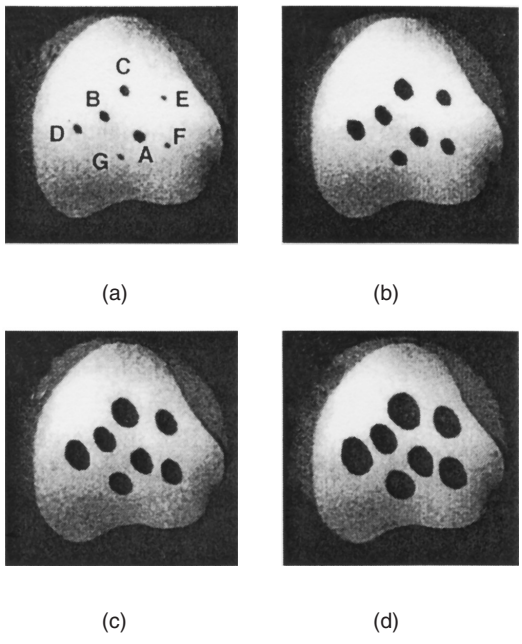

Figure W22.26. LEEM micrograph of the etching of a terrace on Si(100) by oxygen at $T = 1235$ K. The images are those of vacancy islands at (*a*) 1 s, (*b*) 10 s, (*c*) 20 s, and (*d*) 30 s after nucleation. [From J. B. Hannon et al., *Phys. Rev. Lett.*, **81**, 4676 (1998). Copyright 1998 by the American Physical Society.]

The figure illustrates the situation where rays 1 and 2 are reflected from the part of the step closer to the lens, while rays 3 and 4 come from the part farther from the lens. Positive amplitude is indicated to the left of the image plane and negative amplitude to the right of the image plane. Suppose that the energy of the electrons is adjusted so that the step size is one-fourth of a wavelength. This would cause rays 1 and 2 to be half a wavelength out of step with rays 3 and 4 when they hit the image plane, I. At

point D on the image plane, the net amplitude is zero. It will therefore show up as a dark line. This line is the phase-contrast image of the step on the surface.

Although there are other means of creating the phase contrast, such as defocusing by a small amount, the foregoing scheme illustrates the basic method of how a surface may be imaged using low-energy electrons in a microscopy arrangement. In practice a small area of the sample is illuminated with the incident beam. Information from the diffraction pattern is then processed. The beam is rastered over the sample and data are stored for presentation. The spatial resolution is a function of the electron energy used, varying from 60 nm at 250 eV to 2 nm at 30 keV.

An illustration of a LEEM micrograph is given in Fig. W22.26. The dark-field micrographs show various stages of the nucleation of vacancy islands formed during the etching of a 10 μm terrace on the Si(100) surface in an oxygen atmosphere.

ELECTRON SPECTROSCOPY AND ION SCATTERING

In the following sections we describe methods for obtaining the energy distribution of charged particles. These distributions provide important information about the elementary excitations of the solid. In photoemission experiments a beam of electromagnetic radiation is used to produce energetic electrons that are emitted from the surface and are analyzed and detected. Both ultraviolet radiation and x-rays are used. Low-energy electron beams are scattered from solids to provide information concerning the surface and adsorbates on the surface. Extended x-ray absorption fine structure may be used to obtain accurate information about short-range order in solids. Auger emission spectroscopy is an important tool for obtaining quantitative information concerning the chemical composition on or near surfaces. Secondary-ion mass spectrometry and Rutherford backscattering provide additional information regarding the chemical composition and defect structure.

W22.16 Photoemission

Photoemission involves the absorption of a photon by a material and the immediate emission of an electron into vacuum. It has been studied in some detail in Section 19.9. The energy spectrum and photoelectron yield are measured, often as a function of photon energy. Photoemission may be carried out with ultraviolet radiation, in which case it is called *ultraviolet photoemission spectroscopy* (UPS), or with x-rays, in which case it is called *x-ray photoelectron spectroscopy* (XPS) or *electron-spectroscopy for chemical analysis* (ESCA). Since the mean free path of electrons is limited in materials, photoemission provides information concerning the surface region of the solid, especially in the case of UPS. Photoemission may be used to study either crystalline or amorphous solids. It is not useful for liquids because of the need to have a good vacuum present, so that electrons may reach the detector without making collisions with gas molecules.

Ultraviolet Photoemission Spectroscopy (UPS). In UPS electrons are promoted from occupied states below the Fermi level to states above the vacuum level. The photon's energy must exceed the work function $e\Phi$ of the material being studied. The maximum energy the electron may have is given by a famous formula of Einstein:

$$E = \hbar\omega - e\Phi, \tag{W22.98}$$

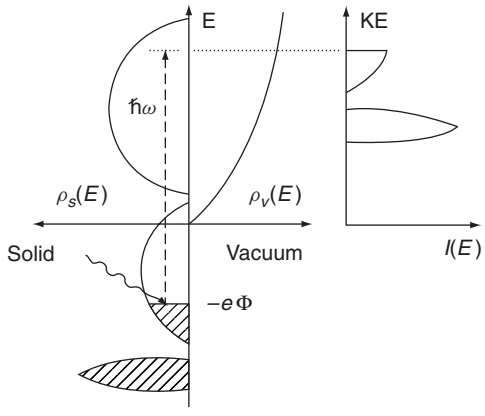

Figure W22.27. Photoemission from a metal with an occupied valence band and a partially occupied conduction band. The density of electron states in the solid and vacuum, and the energy-distribution curve $I(E)$ are shown.

where $\hbar\omega$ is the energy of the incident photon. Since the energy of the ultraviolet photon is relatively small, electrons are extracted from the conduction band and the upper valence bands. A schematic of the photoemission process is given in Fig. W22.27. Three quantities are sketched in this figure. The left-hand side shows the density of states in the solid, $\rho_s(E)$. The vacuum level is taken to be the zero of energy. The Fermi level lies at energy $-e\Phi$. Those states below the Fermi level are occupied and are shaded on the diagram. The density of states in the vacuum $\rho_v(E)$ is also sketched in the figure. It corresponds to that of a free electron. On the right-hand side of the figure the energy distribution curve of the emitted electrons, $I(E)$, is sketched. Ideally, this curve is (aside from possibly smoothly varying distortions due to the energy dependence of the dipole matrix elements) a replica of the density of states of the solid below the Fermi energy. More realistically, there are significant contributions due to secondary electrons.

A formula for the energy-distribution curves may be derived from Fermi's golden rule. The rate of absorption of photons is

$$\Gamma(\omega) = \frac{2\pi}{\hbar} \sum_{i,f} \sum_{s} |M|^2 \delta(E_f - E_i - \hbar\omega) f(E_i, T)[1 - f(E_f, T)], \qquad \text{(W22.99)}$$

where M is the dipole matrix element of the interaction of the photon with the electron, and i and f refer to the initial and final states of the electron, respectively. There is a sum over the two spin states, s, of the electron. The radiation interaction preserves spin projection. There are also Fermi–Dirac distribution function factors introduced in Chapter 7 and Appendix WB,

$$f(E, T) = \frac{1}{\exp[\beta(E - \mu)] + 1}. \qquad \text{(W22.100)}$$

Here μ is the chemical potential (approximately equal to the Fermi energy, E_F, at low temperatures). The first Fermi factor guarantees that there is an electron in state i, the

second factor guarantees that state f is empty, so a transition can occur. Introduce the electron density of states $\rho(E)$ as in Eq. (7.67). The absorption rate may be expressed as

$$\Gamma = \int \Gamma(E')\,dE', \tag{W22.101}$$

where $\Gamma(E')\,dE'$ is the rate of absorption of photons leading to excited electrons within the energy band E' to $E' + dE'$. This rate is given by

$$\Gamma(E') = \frac{\pi}{\hbar}\overline{|M|^2}\rho_v(E')\rho_s(E' - \hbar\omega)f(E' - \hbar\omega, T)[1 - f(E', T)], \tag{W22.102}$$

where an average squared matrix element is used as an approximation. The rate of producing photoemitted electrons is

$$I(E') = \Gamma(E')P(E'), \tag{W22.103}$$

where $P(E')$ is the probability that if a photoelectron is produced, it will emerge from the surface.

The graph of $I(E')$ versus E' is called the *energy-distribution curve* (EDC). The previous formulas show that $I(E')$ is proportional to the product of the density of states for the initial and final states. If the photon energy is sufficiently high, the final density of states may be approximated by a free-electron density of states $\rho_v(E') \propto (E')^{1/2}$. The energy-distribution curve may then be used to determine the density of states $\rho_s(E' - \hbar\omega)$ below the Fermi surface.

The total photoelectric current divided by the incident current of photons is called the *photoelectric yield*. It is seen to be proportional to the joint density of states,

$$I(\omega) \sim \frac{\pi}{\hbar}\overline{|M|^2 P}\int \rho_s(E')\rho_v(E' - \hbar\omega)f(E' - \hbar\omega, T)[1 - f(E', T)]\,dE', \tag{W22.104}$$

where an average escape probability factor P has been extracted from the integral.

As the electron leaves the solid, it can undergo inelastic-scattering processes with other electrons. Some of these other electrons emerge as secondary electrons. One therefore finds a large number of low-energy secondary electrons emerging from the solid as well as the photoemitted electron. The energy-distribution curve therefore rises at low energies.

In some experiments the angular distribution of the emitted electrons is analyzed as well as the energy distribution. The study is called *angular-resolved photoemission spectroscopy* (ARPES). This is particularly useful for obtaining information about the surface layer of the solid or atoms or molecules adsorbed on the surface. Different orbitals in these atoms or molecules point in different directions, and this influences the emission pattern. For example, those orbitals pointing perpendicular to the surface are more likely to photoemit electrons in a direction perpendicular to the surface. This can reveal interesting information regarding the nature of the chemical bonds or the particular bonding sites of adsorbed species.

An example of a UPS spectrum is given in Fig. W22.28 for sputter-deposited $Ge_{100-x}Ag_x$ with $0 \leq x \leq 39.6$ at room temperature. The spectra were taken with 21.2-eV photons from a He I ultraviolet light source. The Ge $4p$ valence band extends from

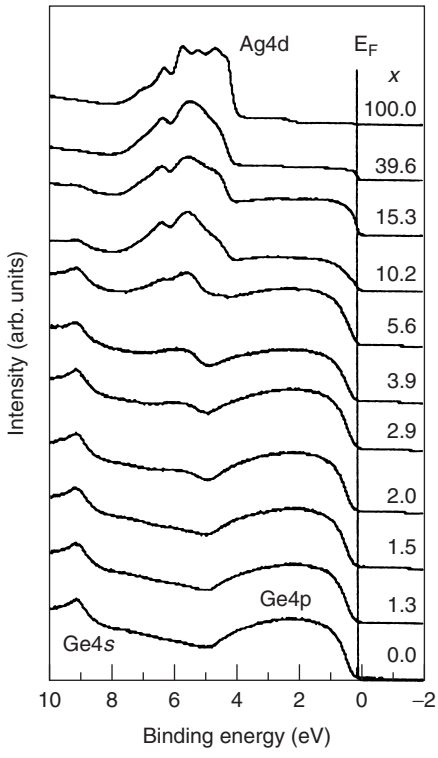

Figure W22.28. Ultraviolet photoemission spectrum of sputter-deposited $Ge_{100-x}Ag_x$ for $0 \leq x \leq 39.6$ [From A. Suzuki and K. Tanaka, *Jpn. J. Appl Phys.*, **37**, 4872 (1998). Copyright 1998 by the Japanese Journal of Applied Physics.]

a binding energy of 4.5 to 0 eV, and the 4*s* band is at a binding energy of 9 eV. The peak that develops at 5.5 eV is due to the Ag–4*d* band. For $0 \leq x \leq 5.6$ the spectra show that Ag is dissolved in a Ge matrix, since a single Ag–4*d* peak appears. For $x \geq 5.6$, phase separation occurs as silver clusters begin to form and the UPS spectrum evolves toward that of bulk Ag, shown at the top of the figure.

X-ray Photoemission Spectroscopy (XPS or ESCA). Often, x-rays rather than UV light are used in a photoemission experiment. The high energy of the x-ray permits the observation of photoemitted core electrons of the solid. The bandwidths of the core electrons are very narrow and the levels may be approximated as having a single energy, E_{core}. The energy of the emitted electron is

$$E' = \hbar\omega - E_{\text{core}}. \tag{W22.105}$$

For a given x-ray photon energy $\hbar\omega$ there will be a sharp peak in the EDC.

The precise value of the core energy is sensitive to the distribution of valence electrons surrounding the core. To photoionize the core electron, the electron must exit the atom by passing through the valence shells. There is a difference of potential between the core and the outside world determined by the charge distribution of the valence electrons. To get a qualitative feeling for this, consider a simple example.

Suppose that a distribution of valence electrons is described by a charge distribution $\rho(\mathbf{r})$, which will be taken to be spherically symmetric, for the sake of simplicity. Poisson's equation gives the potential

$$\nabla^2 V(r) = \frac{1}{r^2}\frac{\partial}{\partial r}\left[r^2 \frac{\partial}{\partial r} V(r)\right] = -\frac{\rho(r)}{\epsilon_0}. \tag{W22.106}$$

Here $V(r)$ is the contribution to the potential from the valence electrons. The contribution to the potential due to the nucleus is fixed, and will be ignored. Taking the position of the core to be approximately at $r = 0$, this gives a difference of potential

$$V(\infty) - V(0) = -\frac{1}{\epsilon_0}\int_0^\infty \frac{1}{r^2}\int_0^r \rho(r')r'^2\, dr'\, dr. \tag{W22.107}$$

For example, suppose that the valence-electron charge distribution is given by

$$\rho(r) = -Q\frac{\mu^3}{8\pi}\exp(-\mu r), \tag{W22.108}$$

so that the total valence charge is $-Q$. The parameter μ in this model represents the inverse of the length over which the valence charge distribution decays outside the atom in question. Then the difference of potential will be

$$V(\infty) - V(0) = Q\frac{\mu}{8\pi\epsilon_0}. \tag{W22.109}$$

The energy of an electron residing in the core may be written as the sum of a constant plus the difference in potential energy between the electron at the core position and the electron at infinity:

$$E_{\text{core}} = \text{constant} - e[V(0) - V(\infty)]. \tag{W22.110}$$

For the model above, therefore,

$$E_{\text{core}} = \text{constant} + \frac{eQ\mu}{8\pi\epsilon_0}. \tag{W22.111}$$

For more compact charge distributions μ will be larger and the core level will be shifted upward (i.e., less tightly bound). Correspondingly, for more spread-out valence charge distributions, the core level will be lowered. In forming chemical bonds, the electron distribution around atoms is distorted. This gives rise to core-level shifts characteristic of the particular bonds that are formed. By measuring the difference between the energy of the incident photon and the emitted electron, the energy of the core level may be found.

Examples of x-ray core-level spectra are given in Fig. W22.29. Data for $La_{1.85}Sr_{0.15}CuO_4$ are taken at $T = 300$ K, where it is semiconducting, and $T = 80$ K, where it is superconducting. The spectrum focuses on the Cu $2p_{3/2}$ state. The data provide evidence for a change of valence state with temperature.

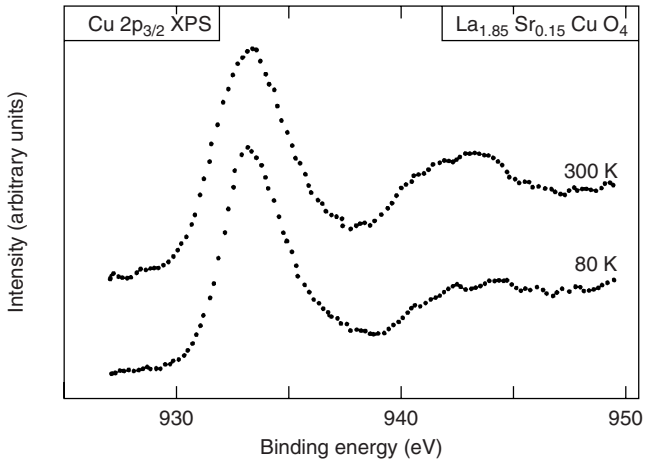

Figure W22.29. X-ray core-level spectroscopy of $La_{1.85}Sr_{0.15}CuO_4$ at $T = 300$ K and $T = 80$ K. [From D. D. Sarma, *Phys. Rev. B*, **37**, 7948 (1988). Copyright 1988 by the American Physical Society.]

W22.17 Low-Energy Electron Loss Spectroscopy

As in LEED, the technique of low-energy electron loss spectroscopy (LEELS) involves directing a beam of electrons at a surface. In LEELS, however, the energy loss of the electron is studied rather than the elastic scattering. Electrons of energy E impinge on a solid, making an angle θ with respect to the surface and come off at a variety of angles. A detector is positioned so it accepts electrons that emerge at an angle θ' and an azimuthal angle ϕ (Fig. W22.30). The current of the scattered beam, I, is then analyzed as a function of the energy of the electron, E'. LEELS data generally can consist of a table of $I(E', \theta', \phi)$ as a function of E and θ, but more often are presented as an angular-integrated function $I(E')$, showing loss peaks. As with LEED, LEELS provides information primarily about what is occurring on or near the surface.

When the electron scatters from the surface, it may emit (or absorb) an elementary excitation from the solid. This excitation is usually a phonon, but other types of

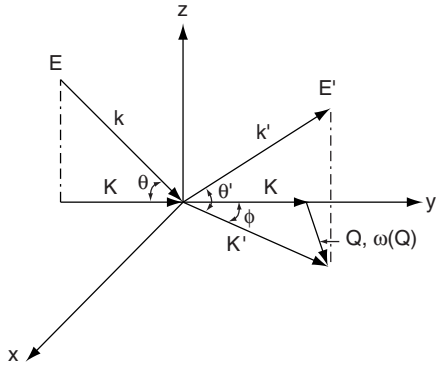

Figure W22.30. Scattering geometry for a LEELS experiment.

excitations, such as two-dimensional plasmons associated with charged layers on the surface, are also possible. The excitation carries with it both energy and momentum. In general, the LEELS spectrum consists of energy-loss peaks from three origins: bulk excitations of the substrate, surface excitations of the substrate, and excitations of adsorbed species on the surface. Because of the limited penetration of electrons into the solid, LEELS is particularly useful for studying the latter two surface excitations.

Surface excitations of the substrate are characterized by having a wave vector parallel to the surface, $\mathbf{Q}$, and a frequency $\omega(\mathbf{Q})$. For the case of a periodic lattice there is conservation of wave vector in the plane of the surface, modulus a reciprocal-net vector (i.e., surface reciprocal-lattice vector):

$$\mathbf{K}' = \mathbf{K} + \mathbf{Q} + \mathbf{G}, \tag{W22.112}$$

where $\mathbf{K}$ and $\mathbf{K}'$ are the surface components of $\mathbf{k}$ and $\mathbf{k}'$. In the case of surface adsorbates, unless the adsorbates form an ordered net, there will be no wave-vector conservation.

In the following, attention will be restricted to the case where there is energy loss. Energy gain, however, is possible if the temperature of the surface is high enough for a thermal excitation to be present and absorbed by the electron. The basic equation of LEELS is the energy conservation condition:

$$E' = E - \hbar\omega. \tag{W22.113}$$

For example, in the case of the excitation during inelastic scattering from an adsorbed molecule, the energy of the electron will be reduced by the difference in energy between two vibrational levels of the adsorbed molecule. It is also possible to study the vibrational spectrum of the adsorbate bonded to the surface. As an analytical tool one may make a quantitative analysis of the adsorbates, since the vibrational frequencies of each molecule are a unique fingerprint for that molecule. The strength of the LEELS signal is proportional to the number of adsorbed molecules.

Suppose that a substrate surface excitation is excited. It is possible to obtain the dispersion curve of the excitation [i.e., to find $\omega(\mathbf{Q})$]. The procedure follows from the energy conservation law:

$$E' = E - \hbar\omega(\mathbf{Q}). \tag{W22.114}$$

Attention will be restricted to the case of near-specular scattering (i.e., let $\mathbf{G} = 0$). Using the following expressions for the wave-vector components (see Fig. W22.30),

$$K = \frac{\sqrt{2ME}}{\hbar}\cos\theta, \qquad K' = \frac{\sqrt{2ME'}}{\hbar}\cos\theta', \tag{W22.115}$$

and the law of cosines

$$Q^2 = K^2 + K^{2'} - 2KK'\cos\phi, \tag{W22.116}$$

the following expression for the wave-vector transfer is found:

$$Q = \frac{1}{\hbar}\sqrt{2m(E'\cos^2\theta' + E\cos^2\theta - 2\sqrt{EE'}\cos\theta\cos\theta'\cos\phi)}. \tag{W22.117}$$

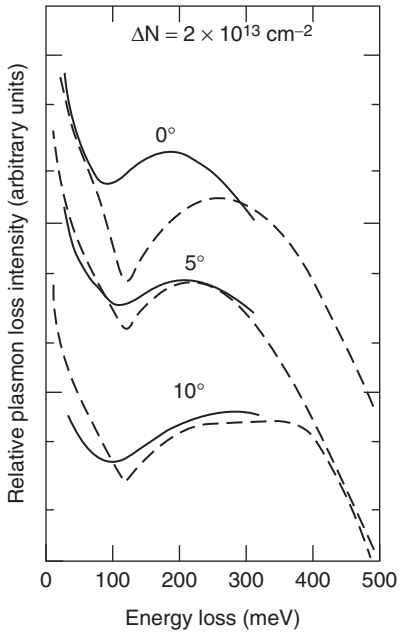

Figure W22.31. LEELS spectra for ZnO for several scattering angles. [Reprinted From Y. Goldstein et al., *Surf. Sci.*, **98**, 599 (1980), Copyright 1980, with permission from Elsevier Science.]

Since E' is measured and E is known, the value of $\omega(\mathbf{Q})$ may be determined. Equation (W22.117) gives Q in terms of E, E', θ, θ' and ϕ. Thus the dispersion relation for the excitation can be measured.

An example of a LEELS spectrum is presented in Fig. 19.17 for n-type GaAs. The spectrum shows phonon loss and gain peaks as well as a surface-plasmon loss peak. In Fig. W22.31 data for angular-resolved LEELS are presented for electrons scattering from a ZnO surface with an accumulation layer. The data are interpreted in terms of the excitation of two-dimensional plasmons in the accumulation layer. From this data, using Eq. (W22.117), it is possible to obtain information about $\omega(\mathbf{Q})$ for the two-dimensional plasmon. The breadth of the peaks is due to the large dispersion of the two-dimensional plasmon.

W22.18 Extended X-ray Absorption Fine Structure

An accurate determination of interatomic distances in a crystal may be obtained by carefully studying the x-ray absorption spectrum. The absorption spectrum exhibits oscillatory structure that comes about due to an interference effect involving the electrons. The method is called *extended x-ray absorption fine-structure* (EXAFS) *spectroscopy*.

When x-rays pass through a sample of thickness d the intensity of the emerging beam, I, is related to the intensity of the incident beam, I_0, through Beer's law:

$$I(d) = I_0 \exp(-\alpha d), \tag{W22.118}$$

where the very small surface reflection of the x-rays is neglected. The attenuation constant, α, has contributions arising from both the absorption of x-rays and the Bragg scattering of x-rays out of the incident beam (extinction). In this section attention centers on the absorption contribution.

Absorption comes about when an electron is photoionized from an atom. The electron is promoted from some low-lying state to a state in the conduction band. In the case of deep-core levels the bandwidths are very narrow and there is a threshold absorption energy from a given band equal to the difference in energy between the Fermi energy, E_F, and the core-level energy, E_{core}. For simplicity's sake, restrict the discussion to the case of a parabolic conduction band. When the excited electron travels through the crystal it has a wave vector

$$k = \frac{1}{\hbar}\sqrt{2m[\hbar\omega - (E_c - E_{\text{core}})]}, \tag{W22.119}$$

where E_c is the energy of the bottom of the conduction band. Thus the wave vector is a function of the x-ray frequency.

The rate at which photon absorption takes place depends on how probable it is to find the *excited* electron at the position of the nucleus. Technically, this comes about because the rate depends on a matrix element of the radiation operator between wavefunctions governing the initial and final states of the electron. In particular, it is sensitive to the magnitude of the final-state wavefunction at the position of the atom. If this magnitude were somehow to increase, the absorption would increase, whereas if it were to decrease, the absorption would decrease.

Upon absorption of the photon a spherically outgoing electron wave is created with the wave vector above. This wave may scatter off neighboring atoms in the crystal a distance a_j away. The waves reflected interfere with the wave emitted as in Fig. W22.32. What is of primary interest is the situation at the location of the ionized atom. If there is *constructive interference*, the amplitude of the final-state electron wavefunction will be maximum. If there is *destructive interference*, the amplitude will be minimum. The condition for constructive interference is

$$2ka_j + \delta_j = 2\pi N. \tag{W22.120}$$

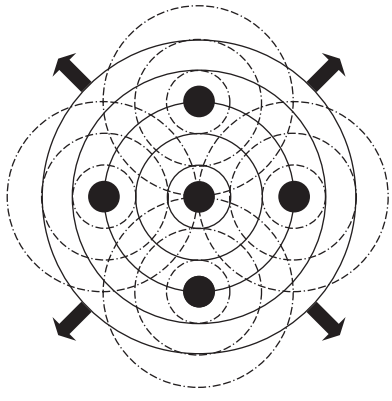

Figure W22.32. Spherically outgoing excited electron waves scatter off neighboring atoms and these reflected waves interfere with the emitted wave.

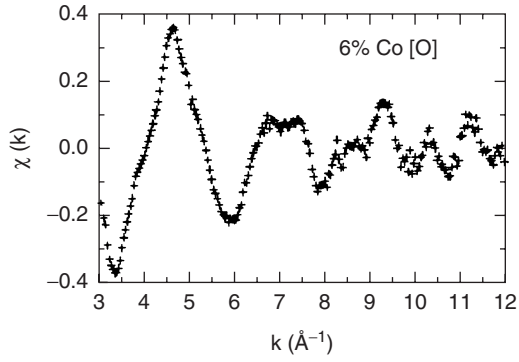

Figure W22.33. EXAFS oscillations for $YBa_2(Cu_{1-y}Co_y)_3O_{6+x}$. [From H. Renevier et al., *Phys. Rev. B*, **47**, 11398 (1993). Copyright 1993 by the American Physical Society.]

Here $2a_j$ is the round-trip distance to atom j and δ_j is a phase shift characteristic of the scattering of the electrons from the atoms. One expects the phase shift to be a slowly varying function of electron energy. Thus interference oscillations in the x-ray absorption spectrum are expected. The separation between neighboring interference maxima (Fig. W22.33) provides a measurement of the various distances to shells of nearby atoms. Thus

$$\Delta k = \frac{\pi}{a_j} = \frac{1}{\hbar}\Delta\sqrt{2m[\hbar\omega - (E_c - E_{\text{core}})]}. \tag{W22.121}$$

In practice, the absorption spectrum is Fourier analyzed as a function of k and the peak positions in r space appear directly. Separate peaks may be identified with NNs, next-NNs, and so on.

An example of EXAFS oscillations appears in Fig. W22.33 for excitation of a Co core level. The data are for the compound $YBa_2(Cu_{1-y}Co_y)_3O_{6+x}$. The quantity $\chi(k)$ is the modulated part of the absorption constant. It is defined by $\chi(k) = [\alpha(k) - \alpha_0(k)]/\alpha_0(k)$, where $\alpha(k)$ is the absorption coefficient, including its oscillations, and $\alpha_0(k)$ is obtained by averaging $\alpha(k)$ (a smoothly varying function of k) over the oscillations. By using the oscillations to determine the NN distance, it is possible to determine that the Co ion has a valence state of +3. It is also possible to determine the coordination number (5) of the Co ions to the oxygen ions.

In addition to EXAFS there is a technique called SEXAFS, which is surface EXAFS. Grazing-incidence x-rays are used so that the radiation does not penetrate the solid deeply and the surface region of the solid is probed. A technique closely related to EXAFS is XANES (*x-ray absorption near-edge structure*).

W22.19 Auger Emission Spectroscopy

A useful tool for characterizing the chemical composition of a solid in the vicinity of the surface is Auger emission spectroscopy (AES). A monoenergetic beam of high-energy (1 to 10 keV) primary electrons impinges on the surface of the solid and causes collisional ionization events to occur. Some of these events result in deep core-level electrons being knocked out. In light elements (Be to Si), typically a K-shell electron

is ionized, leaving a K-shell hole behind. In intermediate atomic-number elements (Al–Nb) the core hole might be in the L shell, and in still heavier elements (Zr–Au) in the M shell. (The various shells are actually themselves split into subshells by both fine-structure splitting and crystal-field splitting. Thus one may refer to the L-I, L-II, L-III subshells, etc.)

Upon formation of the hole, the ion is left in an excited state. An electron from some higher-energy shell (which may be broadened into a band) can fill the vacancy, but first it must get rid of its excess energy. Suppose, for example, that a K-shell hole is created and is to be filled by an electron falling from the L shell. There are two methods by which the L-shell electron can shed its excess energy. One is by emitting an x-ray, whose energy is given by

$$\hbar\omega = E_{\mathrm{L}} - E_{\mathrm{K}}. \tag{W22.122}$$

The second method is by having the electron make a Coulomb collision with another electron [e.g., also from a subshell of the L shell (denote it by L′)] and transfer the energy to that electron. The energy of the L′ electron will then be elevated to

$$E = E_{\mathrm{L}'} + E_{\mathrm{L}} - E_{\mathrm{K}}. \tag{W22.123}$$

If this energy exceeds the vacuum level, some fraction of the Auger-excited L′ electrons will be emitted from the solid (Fig. W22.34). Since for the inner shells the energies E_{K}, E_{L}, and $E_{\mathrm{L}'}$, are all well defined and vary from atom to atom, the energy E will also be well defined and will be characteristic of the particular atom involved.

The intensities of the Auger peaks provide quantitative information about the chemical abundance of those elements present. The location of the peaks in the energy distribution and their line shapes also provide information about their chemical bonding. In Table W22.2 some characteristic Auger-transition energies are listed.

For light atoms the Auger process is the dominant mode of filling the core hole. For heavy atoms x-ray emission becomes appreciable. Other possible Auger transitions involve additional shells and/or subshells of the atom. Thus one has K–L–M, K–M–M, L–M–M, N–O–O, L–M–N processes, and so on. For the upper valence bands, however, where the band width is large, there will be a broad band of electron energies emitted and the technique loses its value as an analytical tool.

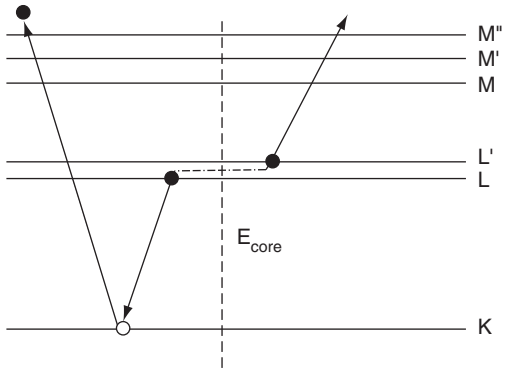

Figure W22.34. Auger process. An electron from the L-shell fills the K-shell vacancy and causes an L′ electron to be emitted.

TABLE W22.2 Typical Auger Transitions and Their Energies

Atom	Transition	Auger Electron Energy (eV)
Ag	M–N–N	351
Si	K–L–L	1619
Al	K–L–L	1396
Mg	K–L–L	1186
Cu	L–M–N	920
Si	L–M–M	92.5
Al	L–M–M	68
Mg	L–M–M	45

The reason that AES is regarded as a surface technique has to do with the mean free path of electrons in solids. The electrons lose energy by a variety of processes, including plasmon emission, electron–hole pair excitations, and phonon emission. This limits the range in which it is possible to get Auger electrons out of the solid to the vicinity of the first few surface layers.

Auger spectra are usually presented as derivative spectra. This makes the spectra less sensitive to drifts in the electrical current. The derivatives are obtained by superimposing a weak ac component to the incident current and taking the difference in the Auger current electronically. An example of an Auger spectrum for galvanized steel exposed to atmospheric corrosion for four days is presented in Fig. W22.35. In the energy range of interest there are features due to Zn and also atmospheric components such as O and C present.

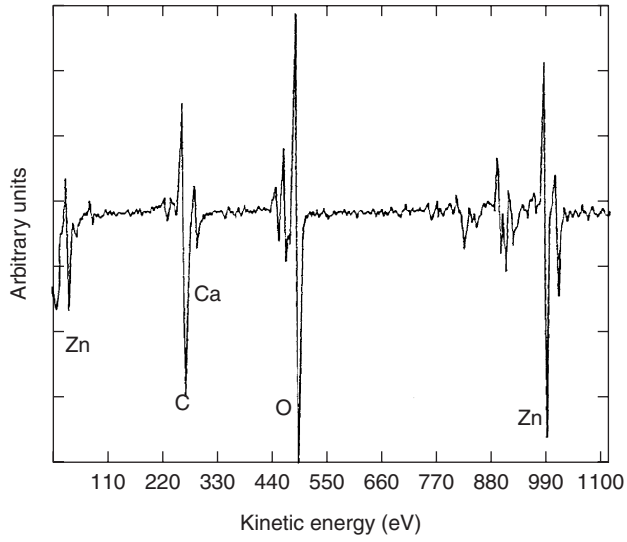

Figure W22.35. Auger electron emission spectrum for galvanized steel undergoing atmospheric corrosion. (From C. Beltran et al., in F. A. Ponce and M. Cardona, eds., *Surface Science*, Springer–Verlag, Berlin, 1991.)

Sometimes, instead of using atomic notation such as L–M–M one denotes the process by L–V–V, indicating that the valence bands (V) are considerably broader than the atomic levels.

W22.20 Secondary-Ion Mass Spectrometry

Sputtering is the process whereby a beam of energetic ions is directed at the surface of a solid and atomic and molecular fragments of the solid are ejected. The fragments may be electrically charged or neutral. In secondary-ion mass spectrometry (SIMS) a quantitative analysis of the emerging ion constituents is undertaken using a mass spectrometer. Often, the emerging neutrals are ionized by external means before the analysis is made. SIMS provides a powerful technique to study the profile of composition versus depth in a sample.

SIMS is capable, in principle, of detecting all elements present in the range of parts per million or even parts per billion. It has a dynamic range of nine orders of magnitude, meaning that it may detect dominant atoms as well as impurity atoms present in low concentrations. It can distinguish different isotopes. Typical depth resolution is on the order of 10 nm, whereas the focused beam size can be made as small as 100 nm. Sputtered holes as deep as 30 μm may be bored in the sample. It is therefore possible to create three-dimensional images of a heterogeneous structure by methodically sputtering away the outer layers. Sputtering is also used in conjunction with AES for depth profiling.

Typically, the energy of the incident ion is in the range 1 to 20 keV. The most often used ions are O_2^+ and Cs^+. The oxygen ion is used when the sample is electropositive, whereas the cesium ion is used when the sample is electronegative.

In the sputtering process the incident ion makes Coulomb collisions with the ions of the material. Since the energy of the incident ion is fairly high, to a first approximation, one may regard the collisions as if they take place between free particles. This permits the use of conservation laws to analyze the process. Consider the collision of two ions of masses M_1 and M_2, respectively. Suppose that particle 1 has momentum $\mathbf{p}_1$; particle 2 is at rest. After the collision the momenta are $\mathbf{p}_1'$ and $\mathbf{p}_2'$. Momentum conservation requires that

$$\mathbf{p}_1 = \mathbf{p}_1' + \mathbf{p}_2'. \tag{W22.124}$$

Energy conservation gives

$$\frac{p_1^2}{2M_1} = \frac{p_1'^2}{2M_1} + \frac{p_2'^2}{2M_2}. \tag{W22.125}$$

Let the angle that $\mathbf{p}_2'$ makes with $\mathbf{p}_1$ be ϕ. Then it follows that

$$E_2' = \frac{4M_1M_2}{[M_1 + M_2]^2} E_1 \cos^2 \phi. \tag{W22.126}$$

Let the angle between vectors $\mathbf{p}_1$ and $\mathbf{p}_1'$ be denoted by θ. The final energy of particle 1 is then

$$E_1' = E_1 \left[\frac{\cos\theta + \sqrt{M_2^2/M_1^2 - \sin^2\theta}}{1 + M_2/M_1} \right]^2. \tag{W22.127}$$

In general, the collisions are not elastic and there is some degree of excitation and ionization taking place. For the hard collisions (i.e., collisions involving substantial momentum transfer) that are responsible for sputtering, however, the energy transfer involved in the moderation of the incident ions is large compared with the ionization energy. The effects of the weaker collisions responsible for ionization may be studied separately.

A 10-keV O_2^+ ion has a speed of 2.5×10^5 m/s, which greatly exceeds the speed of sound in solids. The lattice is unable to carry the energy away as phonons. A cascade of collisions occurs in the region where the incident ion strikes the surface. The energy of the ion is distributed among the atoms in that region. If the energy per atom exceeds the cohesive energy of the solid, these atoms are likely to evaporate from the surface. Some of them will emerge as ions, although most will come out as neutrals. Some of the emerging ions will be reneutralized on the way out. The probability that a given species will leave as an ion is very chemical dependent as well as a function of the nature of the sputtering ion. It is known, for example, that a cesiated surface has a low work function, whereas an oxygenated surface has a high work function. This could easily affect the reneutralization probabilities for the emerging ions, since electrons will have to tunnel out from the solid across a vacuum barrier to reach the emitted ions as they leave the solid.

Once the ions emerge from the sample, the mass spectrometry may be carried out in one of three ways. One may use an accelerating cathode to speed up the ions and then inject them into a uniform magnetic field. Alternatively, one may use a quadrupole mass spectrometer. Finally, one may make a time-of-flight measurement. The first method will be examined.

The speed of the positive ion as it passes through the cathode depends on the cathode voltage V, relative to the sample:

$$v = \sqrt{\frac{2qV}{M}}, \tag{W22.128}$$

where the initial velocity of the ion as it leaves the solid is negligible. The diameter of the resulting circular orbit in the magnetic field is

$$D = \frac{2Mv}{qB}, \tag{W22.129}$$

where q and M are the charge and mass of the ion and B is the strength of the magnetic induction. Thus the mass-to-charge ratio is

$$\frac{M}{q} = \frac{B^2D^2}{8v}. \tag{W22.130}$$

A typical SIMS spectrum of Si exposed to oxygen is presented in Fig. W22.36, where the number of counts in a detector is plotted as a function of the mass-to-charge ratio M/Z and where $q = Ze$. Note that the species ejected reflect the bonding in the solid and, in particular, that an SiO_2 fragment is not ejected.

W22.21 Rutherford Backscattering

A powerful technique for compositional depth profiling of a solid is Rutherford backscattering (RBS). Usually, an α-particle source is used with its energy on the

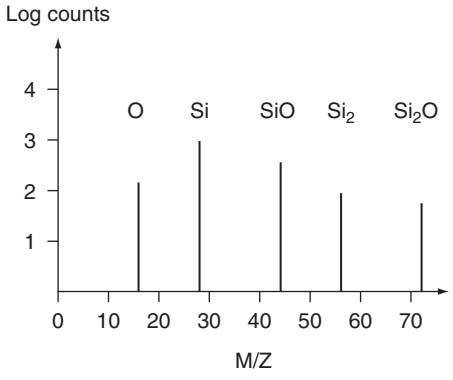

Figure W22.36. SIMS spectrum for SiO_2.

order of 1 MeV. The α-particle is directed normal to the surface and, when scattered through an angle $\theta > \pi/2$, exits through the same surface that it entered. The energy of the α-particle is measured and the energy loss is determined. This energy loss depends on how far the particle penetrated the solid and the type of atom responsible for its deflection.

As a fast charged particle passes an atom it loses energy, primarily by electronically exciting or ionizing the atom. In a solid, phonon processes or other elementary excitations also come into play. These processes lead to a steady decrease in the energy of the particle and may be described by an energy loss per unit length. Bethe gave an approximate theoretical formula for the energy loss per unit distance due to electronic excitation and ionization:

$$\frac{dE}{ds} = -\frac{2\pi n Z_2}{E}\left(\frac{Z_1 e^2}{4\pi\epsilon_0}\right)^2 \ln\frac{2mv^2}{\mathrm{IE}}, \tag{W22.131}$$

where Z_1 is the charge state of the projectile (2 for α-particles), Z_2 the atomic number of the target nucleus, E is the energy of the projectile and v the corresponding speed, n the concentration of target atoms, m the mass of an electron, and IE the ionization energy of the target atom. The energy loss is a slowly varying function of the energy and may be assumed to be constant if the energy-loss range under consideration is sufficiently small. The precise form of the energy-loss function varies from material to material and may be determined experimentally by passing beams through thin samples and measuring the resulting energy loss. It presumably also contains corrections due to phonon losses.

In addition to the mechanism above, there exists the possibility of energy loss resulting from hard Coulomb collisions between the α-particle and the target nuclei (i.e., Rutherford scattering). The cross section for these collisions is on the order of a barn (10^{-28} m^2). The differential scattering cross section in the laboratory frame is

$$\frac{d\sigma}{d\Omega} = \left(\frac{Z_1 Z_2 e^2}{8\pi\epsilon_0 E_1}\right)^2 \frac{[\cos\theta + \sqrt{1 - x^2\sin^2\theta}]^2}{\sin^4\theta\sqrt{1 - x^2\sin^2\theta}}, \tag{W22.132}$$

where E_1 is the energy of the α-particle just prior to scattering and $x = M_1/M_2$.

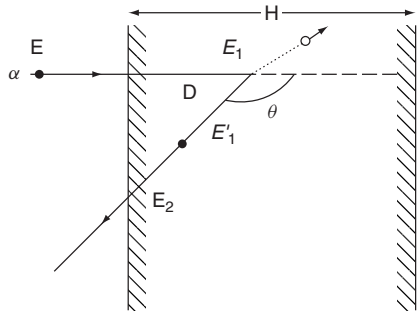

Figure W22.37. Rutherford backscattering geometry.

Suppose that the α-particle enters the solid with energy E at normal incidence and travels a distance D before undergoing Rutherford backscattering. It will arrive at the target nucleus with energy E_1:

$$E_1 = E - \int_0^D ds \frac{dE}{ds} \simeq E - D\left(\frac{dE}{ds}\right)_1, \tag{W22.133}$$

where the subscript indicates that the energy-loss function is to be evaluated at an average energy for the inward journey. The detector is set to measure the backscattered current at a scattering angle θ, as in Fig. W22.37. The energy of the projectile just after the backscattering event is

$$E_1' = F(\theta)E_1, \tag{W22.134}$$

where it was found in Eq. (W22.127) that

$$F(\theta) = \left[\frac{\cos\theta + \sqrt{1/x^2 - \sin^2\theta}}{1 + 1/x}\right]^2 \leq 1. \tag{W22.135}$$

The projectile then travels an additional distance $-D\sec\theta$ before emerging from the solid. The final energy is

$$E_2 = E_1' - \int_0^{-D\sec\theta} \frac{dE}{ds}\, ds \simeq E_1' + D\sec\theta\left(\frac{dE}{ds}\right)_2. \tag{W22.136}$$

Here dE/ds is evaluated for the backscattered journey. Thus

$$E_2 = EF(\theta) - D\left|\left(\frac{dE}{ds}\right)_1 F(\theta) - \left(\frac{dE}{ds}\right)_2 \sec\theta\right| \equiv EF(\theta) - aD. \tag{W22.137}$$

The current entering the detector per unit solid angle per unit energy is

$$\frac{d\dot{N}}{d\Omega\, dE_2} = I\int_0^H dD\, n\frac{d\sigma}{d\Omega}\delta(E_2 + aD - EF(\theta)), \tag{W22.138}$$

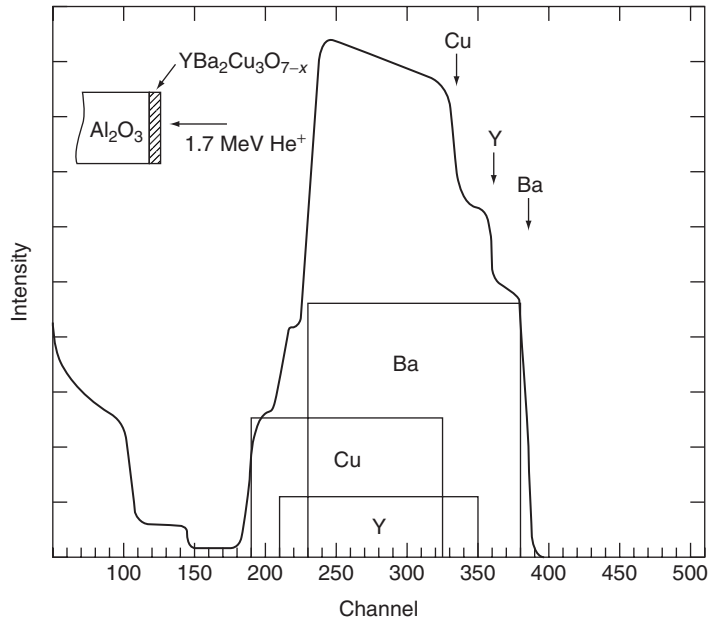

Figure W22.38. Rutherford backscattering spectrum for 1.7−MeV He^+ ions incident on a $YBa_2Cu_3O_{7-x}$ film on an Al_2O_3 substrate. (From H. J. Gossmann and L. C. Feldman, *Mater. Res. Soc. Bull.*, Aug. 1987, p. 26.)

where I is the incident particle current, a was defined in Eq. (W22.137), H is the sample thickness, and n is the concentration of target atoms. The delta function ensures the correct energy relation. Carrying out the integral gives

$$\frac{d\dot{N}}{d\Omega\, dE_2} = I\frac{n}{a}\frac{d\sigma}{d\Omega}\Theta(EF(\theta) - E_2)\Theta(E_2 - (EF(\theta) - aH)). \tag{W22.139}$$

The Θ function is 1 for positive argument and 0 for negative argument. It implies the existence of a high- and a low-energy cutoff in the energy spectrum. The high-energy cutoff corresponds to scattering from atoms on the front surface of the sample. The low-energy cutoff corresponds to scattering from atoms at the depth H (i.e., at the back surface of the sample). Since $F(\theta)$ is unique to each target atom, the locations of these cutoffs permits the identification of the presence of a particular type of atom. The size of the step is proportional to the concentration, n. A typical RBS spectrum is given in Fig. W22.38 for a thin film of $YBa_2Cu_3O_{7-x}$. The spectrum consists of a superposition of rectangles, one for each element, and each with its characteristic width aH, and energy E_2 extending from $EF(\theta) - aH$ to $EF(\theta)$.

SURFACE MICROSCOPY

The next three sections are concerned with scanning surface microscopy. The atomic-force microscope, the scanning-tunneling microscope, and the lateral-force microscope

are studied. A mobile probe is passed over the surface in a rastering fashion and a time-dependent voltage signal is sent by the microscope to a computer, where an image of the surface is constructed. In the atomic-force microscope the signals are proportional to the interatomic force between the tip of the probe and the surface. In the scanning-tunneling microscope it is proportional to the electron current that tunnels between the probe and the conducting surface. The lateral force microscope rubs the tip over the surface and measures both the normal force and the frictional force between the solids.

There are numerous extensions of scanning-probe microscopy. The near-field scanning optical microscope (NSOM) uses a tipped optical fiber to transmit light to a surface and to collect the scattered light, providing information concerning the reflectivity variations of the surface. The scanning-capacitance microscope employs the probe and substrate as the plates of a capacitor and measures the variation of capacitance due to variations in the surface height or due to dielectric deposits on the surface. The scanning-thermal microscope rasters a thermocouple over the surface to measure differences in local temperature. The scanning magnetic-force microscope probes the local magnetic structure on the surface by means of a magnetic tip. Numerous other physical effects are also used as the basis for microscopy.

W22.22 Atomic-Force Microscopy

Two objects brought in proximity will exert forces on each other. This is true of atoms and molecules and is also true of mesoscopic objects. At the most fundamental level, this force is of electromagnetic origin (neglecting the extremely weak gravitational force), although it usually appears in the guise of weak chemical bonding forces. These include van der Waals forces, the interaction of electric multipole moments with each other, and possibly magnetic forces as well. The atomic-force microscope (AFM) uses this force in a controlled way to determine surface structure.

Figure W22.39 is a sketch of the essential elements of the atomic-force microscope. A sample is mounted on a stage that is capable of being moved in three independent directions, x, y, and z. A conducting cantilever beam L with a stylus S at the end is brought close to the surface and the sample is moved in a rastering motion beneath it. Above the cantilever is a plate which, together with the cantilever, forms a capacitor. As the sample is moved back and forth, the force on the stylus varies with time. When the stylus is attracted to the sample, the gap size of the capacitor is increased and the capacitance decreases. If this capacitor is part of an LC circuit, the resonance frequency

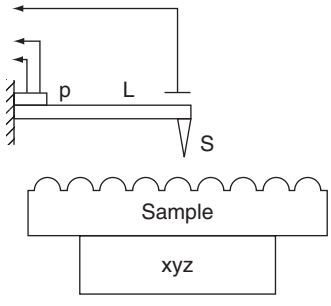

Figure W22.39. Atomic-force microscope.

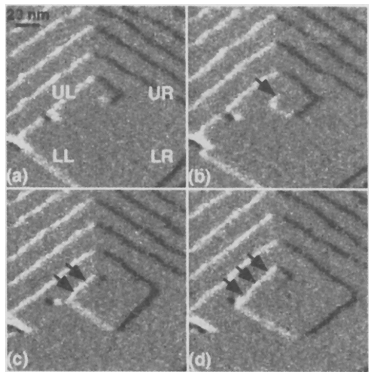

Figure W22.40. Atomic-force microscope micrographs for a growth spiral. [From G. T. Paloczi et al., *Appl. Phys. Lett.*, **73**, 1658 (1998). Copyright 1998, American Institute of Physics.]

may be monitored as a function of time. In another mode of operation, a piezoelectric crystal, p, attached to the cantilever, can be sent a feedback signal to keep the height of S above the surface constant. The voltage across the piezoelectric crystal needed to maintain this constancy then becomes the signal. Other ways of detecting the stylus motion are possible, such as interferometry.

It is important that the microscope be immune to vibrations of the surrounding environment. In addition to vibration isolation, such immunity may be obtained by using a cantilever that has a high natural vibration frequency (in the tens of kilohertz) and by rigidly attaching it to the sample stage. Then, to a first approximation, the entire microscope will vibrate as a rigid body and the separation between the stylus and the sample surface will remain approximately constant.

Since interatomic forces tend to be short ranged, the tip of the stylus provides the dominant force in its interaction with the sample. The stylus is particularly sensitive to forces produced by the sample's dangling bonds, steps, and surface imperfections.

A state-of-the-art atomic-force microscope has recently been constructed with a cantilever consisting of a single crystal of silicon of dimensions 95 μm long by 0.6 μm thick. The resonant frequency is 77 kHz and it is sensitive to forces smaller than 10^{-11} N. A typical scanning velocity is 200 nm/s.

An example of the application of the AFM to the study of a growth spiral is presented in Fig. W22.40. Sequential images are shown for the outward growth of steps from a screw dislocation. It is found that when steps reach a critical length, new steps at right angles to them begin to grow. This is a result of the competition between step-length energy and layer-area energy. The surface is that of calcite.

W22.23 Scanning-Tunneling Microscope

The scanning-tunneling microscope (STM) uses electrons that tunnel from a conducting solid to a conducting probe electrode (stylus) to map the topography of the surface of a solid. The construction is almost identical to that of the atomic-force microscope except that a potential difference, V, is imposed between the stylus and the surface. A tunneling current is established, and this current depends sensitively on the distance between the stylus and the sample. The stylus is made as sharp as possible. Tunneling through the vacuum favors the most direct path, so the characteristic region of the surface

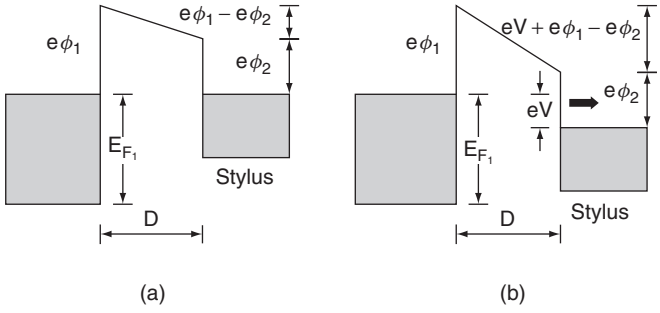

Figure W22.41. Tunneling process: (*a*) unbiased; (*b*) biased.

contributing tunneling electrons is somewhat smaller than the radius of curvature of the stylus tip.

As the surface is rastered past the stylus, the distance D between the stylus and the surface will fluctuate and this will cause the tunneling current to vary. As in the case of the AFM, it is common practice to supply a feedback voltage to the piezoelectric crystal to keep the surface at a constant distance below the stylus. This prevents the tip of the stylus (the "head") from crashing into the surface, thereby destroying the stylus. The variation of this feedback voltage with time (and hence stylus location) provides the signal needed to reconstruct the image of the surface.

It is fairly simple to derive an approximate expression for the tunneling current in a one-dimensional approximation. Consider Fig. W22.41, which shows two cases where the stylus is in proximity to the surface, one without external bias and one with a bias voltage V. For the sake of definiteness, assume that the sample is on the left and the stylus is on the right in each case. Let ϕ_1 be the work function potential of the sample and ϕ_2 be the work function potential of the stylus. When the metals are brought into contact, or near contact, the Fermi levels will rapidly equilibrate by having some charge flow from the metal with the smaller work function potential. This establishes the contact potential difference. (This effect is the basis for what is called the Kelvin probe technique for measuring work function changes associated with adsorption.) Next, suppose that an external bias voltage V is imposed on the system. The Fermi levels are no longer the same and a tunneling current of electrons can flow from one metal to the other. In the case of the diagram it flows from the sample to the stylus.

The particle current per unit area is given by an integral over the Fermi sea of the left-hand conductor:

$$J_z = -2 \int \frac{d\mathbf{k}}{(2\pi)^3} v_z P \Theta(v_z) f(E, T)[1 - f(E - eV, T)], \tag{W22.140}$$

where $f(E,T)$ is the Fermi–Dirac distribution function and P is the probability for tunneling through the barrier. The quantity P is given by

$$P = \frac{v_z'}{v_z} \exp\left[-\frac{2}{\hbar} \int_0^D \sqrt{2m[U(z) - E]}\, dz\right], \tag{W22.141}$$

where v_z' is the velocity on the right and v_z is the velocity on the left. The Fermi–Dirac factors guarantee that the tunneling electron will come from an occupied sample state and tunnel into a vacant stylus state. The form of the barrier potential energy is

$$U(z) = E_{F_1} + e\left[\phi_1 + (\phi_2 - \phi_1 - V)\frac{z}{D}\right], \tag{W22.142}$$

where $z = 0$ at the sample surface and image potential corrections are neglected. At low temperatures the Fermi factors may be replaced by unit step functions (i.e., Θ functions). If the Θ functions are expanded to first order in V, the expression becomes

$$J_z = \frac{2}{(2\pi)^3}\int d\mathbf{k} v_z P\Theta(v_z) eV\frac{1}{2}\delta(E - E_{F_1}), \tag{W22.143}$$

which may be expressed in terms of the density of states at the Fermi level:

$$J_z = \frac{eVv_F}{2}\rho(E_{F_1})\langle\cos\theta\rangle P = \frac{e^2Vv_F}{4}\rho(E_{F_1})P. \tag{W22.144}$$

Here v_z has been replaced by $v_F\cos\theta$ and the average value of $\cos\theta$ in the forward direction is equal to $\frac{1}{2}$. The tunneling integral is readily computed, and finally, a formula for the particle current density is obtained:

$$J_z(V) = \frac{eV}{4}\rho(E_F)v_F'\exp\left[-\frac{4D\sqrt{2m}}{3\hbar}\frac{(e\phi_1)^{3/2} - (e\phi_2)^{3/2}}{e\phi_1 - e\phi_2}\right]. \tag{W22.145}$$

The quantity v_F' is the Fermi velocity for the tunneling probe. The exponential falloff with tunneling distance is expected as well as the dependence on some average barrier height.

The actual value of the electric current is given by $I = -eAJ_z$, where A is a characteristic area. For the case of a stylus tip with radius of curvature R, one may expect $A \approx \pi R^2$. Equation (W22.145) is not completely correct. In reality, one should use the local density of states rather than the bulk density of states. The local density of states varies from position to position in directions parallel to the surface and reflects the variations in local charge density of the surface bonds. Therefore, as one rasters the surface under the tip, the tunneling current will vary from position to position.

An example of an STM picture of the surface of Si(100) is presented in Fig. W22.42. It shows, with atomic resolution, a Si(100) 2×1 surface with a Na overlayer.

W22.24 Lateral-Force Microscope and Surface Force Apparatus

A variant of the atomic-force microscope, called the lateral-force microscope (LFM), can measure the shear stress on a microscopic stylus that is slid across a surface (Fig. W22.43). It is sensitive to forces as small as 1 pN. The stylus, which constitutes one of the solids (commonly diamond or Si_3N_4), is supported by a flexible cantilever that can be deflected as the stylus rubs against the other surface. By measuring the bending of the cantilever, one may determine the normal force exerted on it by the stylus. By measuring the torsion of the cantilever, information concerning the frictional force is obtained. These measurements are made by reflecting a beam of light from the back of the cantilever and recording the position of the reflected spot on a screen. The

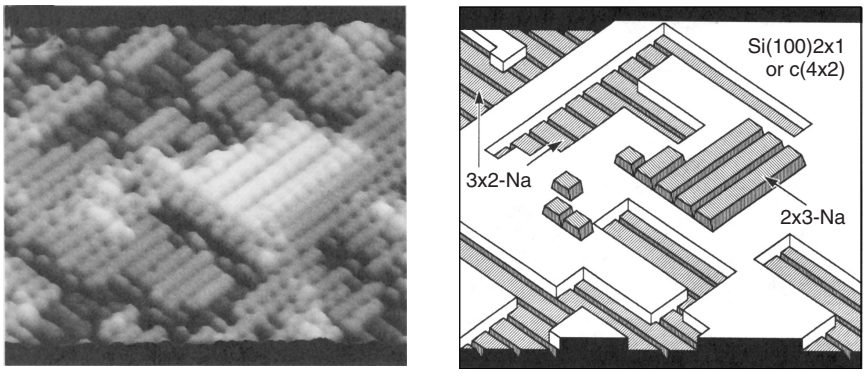

Figure W22.42. Micrograph of the Si(100) surface with an overlayer of Na atoms. [From A. A. Saranin et al., *Phys. Rev. B*, **58**, 4972 (1998). Copyright 1998 by the American Physical Society.]

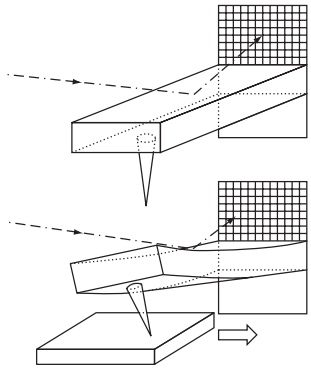

Figure W22.43. Lateral force microscope (LFM). A light beam is reflected off a cantilever and strikes an array of photodetectors. The flexure and torsion of the cantilever are related to the normal and friction forces.

solid lying beneath the stylus is attached to a piezoelectric crystal stage. By applying time-varying potential differences across this crystal, the sample may be rastered back and forth beneath the stylus. Thus a friction map may be generated.

By coating the stylus with a self-assembled monolayer (SAM) of organic molecules, it is possible to sensitize the stylus so that it will respond differently to different adsorbates on the other solid. This is because the chemical specificity of the intermolecular interactions determines the friction force. It was recently found that friction can be both anisotropic and asymmetric when the monolayer consists of tilted molecules.[†] The asymmetry refers to moving the stylus in the direction of the molecular tilt compared with against it.

The surface force apparatus (SFA) is a device with two atomically flat parallel mica plates. The width of the separation may be reduced to nm dimensions. Lubricants are

[†] M. Liley et al., *Science*, **280**, 273 (1998).

placed in the gap and the plates are slid past each other. Evidence for the formation of well-defined liquid layers is found when the gap distance is smaller than 10 nm. The viscosity rises very rapidly as the gap distance is reduced. One finds evidence for the formation of two-dimensional glassy solids within these layers if the layers are very thin (e.g., four molecules thick). As the lubricant is sheared, these layers are deformed elastically and then may release the strain energy by slipping or melting when a critical shear stress is reached. The resulting stick-slip motion is reminiscent of the mechanism believed to produce seismic earthquakes. The sudden slip motions are also believed to peel material off the surfaces, thereby producing delamination wear. Wear is the general term given to the change of geometry of the surfaces and the removal of material from them as a result of friction. In polymer applications it is found that the threshold for substantial wear is correlated with the product Pv, in accordance with Eq. (W19.39). The value is referred to as the *Pv limit*. For example, for polycarbonate and Teflon, the Pv limits are 0.01 and 0.06 MPa·m/s, respectively, for $v = 0.5$ m/s at room temperature.

Another device that is used to study the friction of lubricants is the quartz-crystal microbalance (QCM). The damping of vibrations (i.e., the Q of the quartz crystal plate) is influenced by the viscosity of the lubricant with which it is in contact.

TRANSPORT MEASUREMENTS

In Chapter 7 electrical-transport properties such as the electrical resistivities and the Hall coefficients of materials have been introduced. Some elementary thermal and thermoelectric properties are also discussed. In the following two sections some methods for measuring these properties are reviewed.

W22.25 Electrical Resistivity and Hall Effect

The simplest method for measuring resistivity involves the use of a cylindrical sample of material of length L and cross-sectional area A. The resistance R is measured and the resistivity is given by $\rho = RA/L$. The accuracy of the measurement is limited by the geometric measurements and the ability to control fringing fields. A simple geometrical arrangement for measuring the Hall coefficient is given in Fig. 7.1 and discussed in Section 7.3.

For a large sample of material with a planar surface, the four-contact method may be employed to measure ρ. Suppose that the material occupies the half-space $z < 0$. Place four contacts at four points on the surface at the locations defined by the vectors $\mathbf{r}_A$, $\mathbf{r}_B$, $\mathbf{r}_C$, and $\mathbf{r}_D$. The contacts are placed close together so the distance between them is much less than the distance to the edges of the surface. If a current I is injected into contact A, it will set up an electrostatic potential field $\phi_{\mathrm{A}}(\mathbf{r}) = \rho I/(2\pi|\mathbf{r} - \mathbf{r}_{\mathrm{A}}|)$ within the material. Similarly, if one draws a current I out of contact B, the potential field is given by $\phi_{\mathrm{B}}(\mathbf{r}) = -\rho I/(2\pi|\mathbf{r} - \mathbf{r}_{\mathrm{B}}|)$. When the current is injected at A and removed at B, these potentials are superimposed to give $\phi(\mathbf{r}) = \phi_{\mathrm{A}}(\mathbf{r}) - \phi_{\mathrm{B}}(\mathbf{r})$. The difference in potential is then measured between points C and D. The resistance is

$$R_{\mathrm{CD,AB}} = \frac{V_{\mathrm{CD,AB}}}{I} = \frac{\rho}{2\pi}\left(\frac{1}{r_{\mathrm{CA}}} - \frac{1}{r_{\mathrm{CB}}} - \frac{1}{r_{\mathrm{BA}}} + \frac{1}{r_{\mathrm{DB}}}\right), \tag{W22.146}$$

where $r_{\mathrm{CA}} = |\mathbf{r}_{\mathrm{C}} - \mathbf{r}_{\mathrm{A}}|$, and so on.

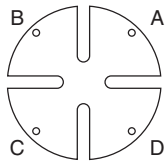

Figure W22.44. Clover-shaped sample for the van der Pauw method of measuring the resistivity or the Hall coefficient.

The van der Pauw method[†] extends this method to two dimensions and permits one to measure the resistivity and Hall coefficient for a thin sample of material. It will be assumed that there is isotropy in the plane of the slab. Four fine electrodes, labeled A, B, C, and D, are attached to the boundaries of a slab of thickness d. The shape of the sample is unimportant, as long as it has no holes in it (i.e., it must be simply connected). (This may be proven by the method of conformal transformations using complex-variable theory. It will not be derived here.) A typical geometry that is used is illustrated in Fig. W22.44. In the resistivity case two measurements are made. First a current I is driven from C to D and the voltage $V_{\mathrm{AB,CD}}$ is measured across electrodes A and B. The resistance $R_{\mathrm{AB,CD}}$ is computed by the formula $R_{\mathrm{AB,CD}} = V_{\mathrm{AB,CD}}/I$. The measurement is repeated with a current driven from D to A and the voltage measured across B and C. The resistivity is given implicitly by the formula

$$\exp(-\pi R_{\mathrm{AB,CD}} d/\rho) + \exp(-\pi R_{\mathrm{BC,DA}} d/\rho) = 1. \tag{W22.147}$$

The method may be generalized to anisotropic samples.[‡]

The Hall coefficient R_H is determined by measuring the change in the resistance $R_{\mathrm{BD,AC}}$ when a magnetic induction B is imposed perpendicular to the slab. The formula is

$$R_H = d\frac{\Delta R_{\mathrm{BD,AC}}}{B}. \tag{W22.148}$$

From a measurement of the Hall voltage the sign of the carrier may be determined.

W22.26 Thermopower, Peltier Coefficient, and Thermal Conductivity

A system in thermal equilibrium obeys the first law of thermodynamics, given by Eq. (WA.1), $T\,dS = dU + P\,dV - \mu\,dN$. When the system is driven slightly out of equilibrium, current densities are produced. These include the particle-current density, $\mathbf{J}$, and the energy-current density, $\mathbf{J}_U$. Consider the case where the charged carriers are electrons, so the particle current density is proportional to the electrical-current density (i.e., $\mathbf{J}_E = -e\mathbf{J}$). The driving forces for $\mathbf{J}_E$ include the electric field, $\mathbf{E} = -\nabla\phi$, as well as the gradient in the chemical potential and the gradient in the temperature. The same forces drive $\mathbf{J}_U$. In place of the energy-current density, the first law of thermodynamics is used to define the heat-current density, $\mathbf{J}_Q$, in terms of the chemical potential:

$$\mathbf{J}_Q = T\mathbf{J}_S \equiv \mathbf{J}_U - \mu\mathbf{J}, \tag{W22.149}$$

[†] L. J. van der Pauw, *Philips Res. Rep.*, **13**, 1 (1959).
[‡] L. J. van der Pauw, *Philips Res. Rep.*, **16**, 195 (1961).

where $\mathbf{J}_S$ is interpreted as an entropy-current density. For weak driving forces the current densities are expressed as linear combinations of the driving forces:

$$\mathbf{J}_E = e\frac{L_{11}}{T}\nabla(\mu - e\phi) + eL_{12}\nabla\frac{1}{T}, \tag{W22.150a}$$

$$\mathbf{J}_Q = \frac{L_{21}}{T}\nabla(\mu - e\phi) + L_{22}\nabla\frac{1}{T}, \tag{W22.150b}$$

where L_{ij} are coefficients. Onsager proved (in general) that $L_{12} = L_{21}$ so there are three independent coefficients. An example of the Onsager relations has been encountered when the transport properties of metals were studied in Section 7.5.

The significance of the L_{ij} coefficients may be obtained by examining special cases:

1. If T and μ are constant in space, then

$$\mathbf{J}_E = e^2\frac{L_{11}}{T}\mathbf{E}, \tag{W22.151}$$

so $\sigma = e^2L_{11}/T$. The coefficient L_{11} is therefore proportional to the electrical conductivity.

2. If the heat current is measured for the case where there is no electric current (i.e., $\mathbf{J}_E = 0$), it is found that

$$\mathbf{J}_Q = -\frac{L_{11}L_{22} - L_{12}^2}{L_{11}T^2}\nabla T = -\kappa\nabla T, \tag{W22.152}$$

where κ is the thermal conductivity.

3. In the absence of an electric current, an electric field is established in the sample, that is,

$$-e\mathbf{E} = \nabla\mu - \frac{L_{12}}{TL_{11}}\nabla T. \tag{W22.153}$$

The electromotive force is given by

$$\varepsilon = \oint \mathbf{E}\cdot d\mathbf{l} = -\frac{1}{e}\oint d\mathbf{l}\cdot\nabla\mu - \oint Qd\mathbf{l}\cdot\nabla T, \tag{W22.154}$$

where $Q = -L_{12}/eTL_{11}$ is called the absolute thermoelectric power of the material. (The symbol Q is used here rather than S so as not to confuse it with the entropy.) The first term on the right-hand side may be written as $\oint d\mu$ and is zero. The second term may be written as $-\oint Q\,dT$.

Consider an experimental arrangement such as is shown in Fig. W22.45, consisting of two conductors, labeled A and B, with absolute thermoelectric powers Q_A and Q_B, respectively. Let a voltmeter be inserted in one of the conductors to measure the electromotive force $\Delta\varepsilon$. Label the temperatures at the left and right junctions T_J and $T_J + \Delta T$, respectively, and the temperature at the voltmeter $T_J + \Delta T'$. It is assumed that $\Delta T \ll T_J$ and $\Delta T' \ll T_J$. Then

$$\begin{aligned}\Delta\varepsilon &= -Q_\mathrm{A}[(T_J + \Delta T) - (T_J + \Delta T')] - Q_\mathrm{B}[T_J - (T_J + \Delta T)] \\ &\quad - Q_\mathrm{A}[(T_J + \Delta T') - T_J] \\ &= (Q_\mathrm{B} - Q_\mathrm{A})\,\Delta T.\end{aligned} \tag{W22.155}$$

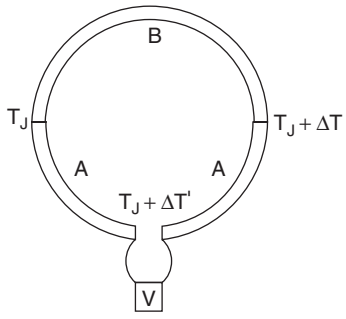

Figure W22.45. Arrangement for measuring the absolute thermopower.

Thus the difference in the thermopowers is the voltage per unit temperature difference:

$$Q_{\mathrm{B}} - Q_{\mathrm{A}} = \frac{\Delta \varepsilon}{\Delta T}. \tag{W22.156}$$

A four-probe technique is used to measure the thermopower. Thermocouple thermometers are placed at the left and right junctions to measure T_J and $T_J + \Delta T$, and the difference of the temperatures is taken to obtain ΔT. The voltage leads are placed across the gap, as shown in Fig. W22.45. In measuring the thermopower one places both the sample and thermometer in vacuum, to eliminate convective heat channels. They are also shielded with highly reflecting surfaces to minimize radiative losses. (The same techniques are used in the design of a thermos bottle.) The voltage could be measured using a potentiometer connected to a sensitive galvanometer. Very small thermocouples, connected to very fine leads, are employed as thermometers.

Thermocouples are thermometers that produce an electromotive potential related to the temperature at the junction. A typical thermocouple is illustrated in Fig. W22.46. Two conductors, A and B, form a junction that acts as the temperature probe. The other wires are each connected to identical conductors, labeled C. The AC and BC junctions are each held at the same standard temperature, T_0. A mixture of ice and water at atmospheric temperature is often used to set $T_0 = 0^{\circ}\mathrm{C}$. The other ends of the C wires are connected to a galvanometer and a potentiometer at room temperature. Typical thermocouples involve the use of copper versus constantan, chromel versus alumel, chromel versus constantan, iron versus constantan, and platinum versus platinum–rhodium.

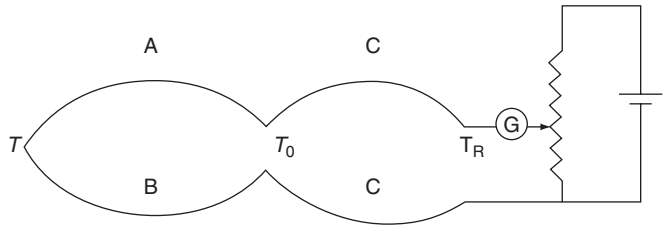

Figure W22.46. Thermocouple arrangement.

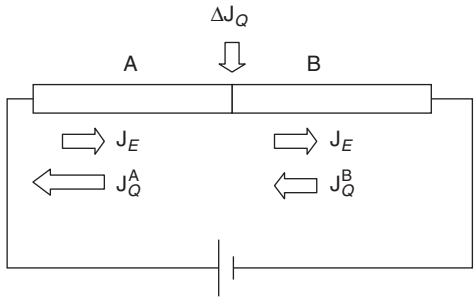

Figure W22.47. Peltier effect.

The Peltier effect involves creating a junction of two dissimilar conductors and passing an electrical current through it. The electrical current is the same in each conductor. Assume that the temperature is held constant. The situation is illustrated in Fig. W22.47. In the absence of a temperature gradient term, the heat current is proportional to the electric current:

$$\mathbf{J}_Q = \frac{L_{12}}{eL_{11}}\mathbf{J}_E = -QT\mathbf{J}_E. \tag{W22.157}$$

Since Q is discontinuous from one conductor to the other, this implies that a heat transfer must take place at the junction. The heat extracted at the junction from the environment is given by

$$\Delta J_Q = J_Q^{\mathrm{B}} - J_Q^{\mathrm{A}} = -T(Q_{\mathrm{B}} - Q_{\mathrm{A}})J_E \equiv \pi_{\mathrm{BA}}J_E, \tag{W22.158}$$

where π_{BA} is called the *Peltier coefficient*. Thus the Peltier coefficient is defined as the heat extracted per unit current. It may be determined from a measurement of the thermopower through the relation

$$\pi_{\mathrm{BA}} = -T\,\frac{\Delta\varepsilon}{\Delta T}. \tag{W22.159}$$

There are a number of ways to measure the thermal conductivity. They often may be classified as transient measurements or steady-state measurements. An example of a transient measurement is the following. Take a rod of length L initially at temperature T_0. At $t = 0$ place the left end of the rod in contact with a thermal bath at temperature T_1. Measure the temperature of a point on the rod at position x for times $t > 0$. The thermal diffusion equation is

$$\nabla \cdot \mathbf{J}_{\mathrm{Q}} + \frac{\partial u}{\partial t} = -\nabla \cdot (\kappa\,\nabla T) + \frac{\partial(\rho c T)}{\partial t} = -\kappa\frac{\partial^2 T}{\partial x^2} + \rho c\frac{\partial T}{\partial t} = 0, \tag{W22.160}$$

where it is assumed that κ is independent of T. The solution to Eq. (W22.160) is

$$T(x, t) = T_1 - (T_1 - T_0)\ \mathrm{erf}\left(\frac{x}{2\sqrt{at}}\right), \tag{W22.161}$$

where ρ is the density, c the specific heat, and the thermal diffusivity is $a = \kappa/\rho c$. The error function erf(x) is defined in Chapter W6. The rise of $T(x,t)$ with time at a fixed x is compared to this formula, and a value for a is determined. The value of c is obtained from a calorimetry experiment.

In the steady-state measurements simple geometrical arrangements are chosen and heat is supplied to the material at a known rate. The temperature differential is measured. For example, if a rod of length L is connected to a heater supplying a known heat flux J_Q, and the temperature difference ΔT is measured between two points along the rod a distance Δx apart, then $\kappa = J_Q \, \Delta x/\Delta T$.

A preferable geometrical arrangement involves the use of concentric cylinders. A cylindrical heater of length L and radius R_1 is surrounded by a hollow sample of material of the same length, with inner radius R_1 and outer radius R_2. Heat is delivered by the electrical heater at a known rate, H. Thermocouples are used to measure the temperature difference ΔT between the inner and outer surfaces of the sample. The thermal conductivity is then given by

$$\kappa = \frac{H}{2\pi L \, \Delta T} \ln \frac{R_2}{R_1}. \tag{W22.162}$$

MAGNETIC MEASUREMENTS

The magnetic properties of materials are discussed in Chapter 9, and a number of magnetic materials are studied in Chapter 17. In this section some of the measurement techniques for characterizing magnetic materials are described. They include use of the Foner magnetometer, the Faraday balance, and the ac bridge. The SQUID magnetometer is discussed in Chapter 16.

W22.27 Foner Magnetometer

The Foner magnetometer is used to measure the magnetization of a small sample of magnetic material. When measuring the saturation magnetization the shape of the sample is not important. For nonsaturation conditions a spherical sample is used so that the orientation of the sample is not relevant. The sample is placed on a reed and is made to vibrate in the presence of a coil of wire. For this reason the apparatus is also known as the *vibrating-sample magnetometer* (VSM). Alternatively, the coil may be vibrated in the presence of the magnetic sample. In either case an ac electromotive force is established in the coil which is readily measured. From this measurement the magnetization may be determined.

A formula for the EMF may be obtained by considering a coil with a current I in the neighborhood of the sample and neglecting resistance effects. Let L be the inductance of the coil in the absence of the sample. The energy of the system is

$$U = \tfrac{1}{2} L I^2 - \mu_0 \mathbf{m} \cdot \mathbf{H}, \tag{W22.163}$$

where H is the magnetic field intensity and $\mathbf{m}$ is the magnetic moment of the sample. It will be assumed that $\mathbf{H} = H\hat{k}$ and that $\mathbf{m} = \mathbf{M}V$, where $\mathbf{M}$ is the magnetization and

V is the volume of the sample. The energy of the system will be constant, so

$$\frac{dU}{dt} = 0 = LI\frac{dI}{dt} - \mu_0 MV\frac{dH}{dt}. \tag{W22.164}$$

Use $LI = N\Phi$, where N the number of turns in the coil and Φ is the magnetic flux through the coil. Assume that $H = H(z)$ and write $dH/dt = v_z\, dH/dz$, where v_z is the z component of the velocity of the sample. From Faraday's law the EMF is given by $\varepsilon = -N\, d\Phi/dt = -L\, dI/dt$. Thus

$$\varepsilon = -\mu_0 MV v_z \frac{1}{I}\frac{dH}{dz}. \tag{W22.165}$$

For a harmonic oscillation of the sample, $z = A\cos\omega t$, where A is the amplitude (typically ≈ 1 mm) and ω is the frequency (typically corresponding to ≈ 100 Hz). Therefore,

$$\varepsilon(t) = \frac{\mu_0 \omega MVA}{I}\frac{dH}{dz}\sin\omega t. \tag{W22.166}$$

From a measurement of the amplitude of the EMF and the mechanical motion, together with knowledge of the sensitivity of the instrument, $|(dH/dz)/I|$, and the volume of the sample, one may determine the magnetization of the sample. The sensitivity function depends on the geometry. For example, consider the ideal case of two coils of wire of radius R separated by a coaxial distance $2D$. A sketch of the Foner magnetometer is given in Fig. W22.48. Some external source (not shown), such as a loudspeaker, is used to establish vibrations in the reed to which the sample is attached. The coils are wound so that the currents generated in the coils will flow in opposite directions. Near the center of symmetry one finds the sensitivity

$$\frac{1}{I}\frac{dH_z}{dz} = -\frac{3NDR^2}{2(R^2 + D^2)^{5/2}}. \tag{W22.167}$$

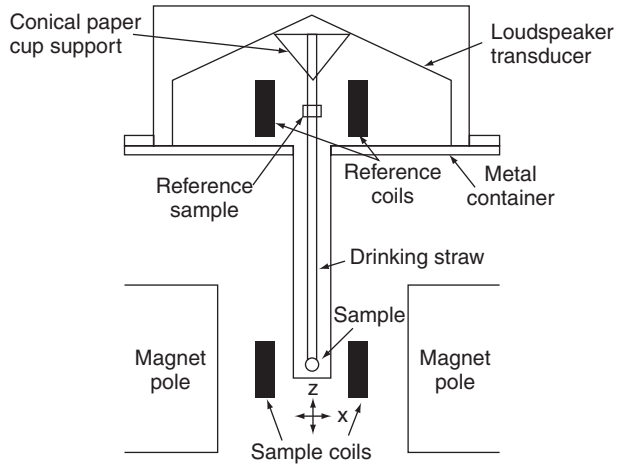

Figure W22.48. Foner magnetometer. (Adapted from S. Foner, J. Appl. Phys., **79**, 4740 (1996). Copyright 1996 by the American Institute of Physics.)

The maximum sensitivity occurs when $R = 2D$ and has the value $|(dH/dz)/I| = 96N/(5R^2\sqrt{5})$. The sensitivity grows with the number of turns (which could typically be $\approx 25{,}000$) and falls off inversely as the square of the radius.

The Foner magnetometer readily measures magnetic moments on the order of 10^{-10} A·m^2 at liquid-nitrogen temperatures, to reduce the thermal noise. The instrument is generally calibrated in terms of a known ferromagnetic material, such as Ni. Magnetizations are measured relative to the calibration standard.

W22.28 Faraday Balance

The Faraday balance permits one to measure the magnetization of a sample in a magnetic field. The technique is illustrated in Fig. W22.49. A solenoidal superconducting magnet establishes a magnetic field intensity H_0 in the axial direction which magnetizes the sample, the magnetization being $M(H_0)$. Note that this uniform magnetic field does not produce a net force on the sample. Weights are placed on the right-hand side of the balance equal to the weight of the sample to maintain equilibrium. Then an inhomogeneous magnetic field H is established by the smaller pair of coils. The coils are arranged as shown in Fig. W22.49. The magnetic force in the axial direction is given by

$$F_z = \frac{\partial(\mathbf{m} \cdot \mathbf{B})}{\partial z} = M(H_0)V\mu_0\frac{\partial H}{\partial z} = W, \tag{W22.168}$$

where V is the volume of the sample. The additional weight W is placed on the right-hand side to counterbalance the magnetic force. In practice, an analytical microbalance is adapted to serve as the balance. The field gradient is vertical. The radius, R, equals the separation between the coils, D, as in the Helmoltz coil arrangement, but the currents are in opposite directions so that a uniform gradient dH/dz is established.

W22.29 AC Bridge

The complex frequency-dependent magnetic permeability of a material, $\mu_r(\omega) = \mu_1(\omega) + i\mu_2(\omega)$, may be measured by means of the ac bridge method. One prepares a

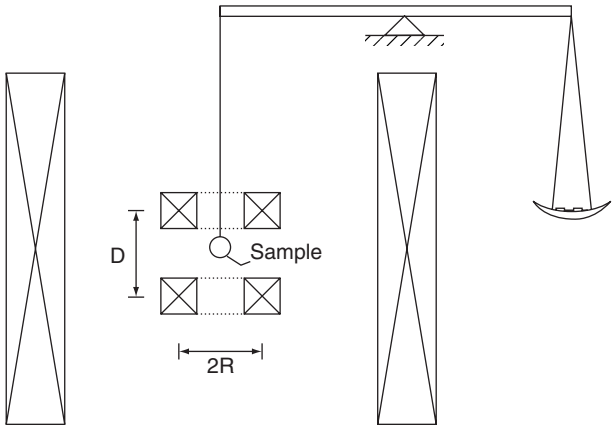

Figure W22.49. Faraday balance.

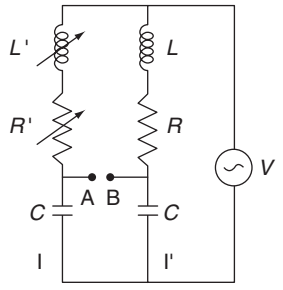

Figure W22.50. Ac bridge.

sample in the shape of a ring and winds N uniform turns of wire around it to fashion an inductor. The inductance is given by

$$L(\omega) = \frac{\mu_0 \mu_r(\omega) h N^2}{2\pi} \ln \frac{b}{a}, \tag{W22.169}$$

where it is assumed that the ring is in the form of an annulus of inner radius a, outer radius b, and thickness h. The inductance is seen to be a complex quantity and may be regarded as a pure inductor in series with a pure resistor. The reactance of the pair is $X = -i\omega L(\omega) = R - i\omega \text{ Re } (L(\omega)) \equiv R - i\omega L$, where

$$R = \frac{\omega \mu_0 \mu_2 h N^2}{2\pi} \ln \frac{b}{a}. \tag{W22.170}$$

The inductor is inserted into one leg of a bridge, as shown in Fig. W22.50. The other legs of the bridge consist of a variable inductor L' in series with a variable resistor R', and two capacitors, each with capacitance C. An ac voltage of frequency ω is imposed across the bridge. The value of R' and L' are adjusted until a null reading for the voltage occurs across the terminals A and B. The bridge is then balanced with $L' = L$ and $R' = R$. The values of $\mu_1(\omega)$ and $\mu_2(\omega)$ are then determined from Eqs. (W22.169) and (W22.170).

RESONANCE TECHNIQUES

The ability of scientists to determine resonance frequencies accurately has played a central role in the development of atomic and nuclear physics and gas-phase chemistry. The techniques were later applied to liquid-phase chemistry and ultimately to solid-state measurements. In the following sections several of these resonance techniques are described. The discussion begins with nuclear magnetic resonance spectroscopy. This is followed by a consideration of nuclear quadrupole resonance spectroscopy. Then electron spin resonance is studied. Finally, the Mössbauer effect is described.

W22.30 Nuclear Magnetic Resonance

It is possible to obtain useful information concerning the composition of a material and the local environment of its individual nuclei by performing nuclear magnetic

resonance (NMR) measurements. The procedure involves placing a sample of the material in a constant uniform magnetic field. A weak perturbing radio-frequency magnetic field is simultaneously applied to the sample while its frequency is varied until maximum power is delivered by the RF field to the sample. This frequency is called the *resonance frequency*. For a given magnetic field it is found that each nucleus has its own particular resonance frequency. The strength of the resonance is directly proportional to the amount of that particular nucleus present in the sample. This is the basis of the use of NMR as a tool for determining the chemical composition. In addition, there are slight shifts of the resonance frequency caused by variations of the local chemical environment of the nucleus. This is due to the nuclei coupling to the surrounding electrons by magnetic interactions and the electrons also coupling to the applied magnetic field. Since the electron distribution reflects the chemical environment (e.g., which chemical bonds are present and what the NNs and next-NNs are), one may also use NMR to obtain this kind of information as well. From a knowledge of the NNs and next-NNs one is often able to piece together the structure of complicated chemical compounds or solids. The utility of NMR hinges on the ability to generate uniform magnetic fields and to perform resonance measurements with extremely high precision. The utility is also based on having a database of NMR signals from known sequences of atoms with which a comparison may be made in determining the structure of a complex molecule or solid.

Some of the main features of NMR follow directly from a classical-mechanical theory, although the correct description must be formulated within the framework of quantum mechanics. The need for a quantum theory stems from the fact that angular momentum is quantized. A nucleus has an angular momentum operator given by

$$\mathbf{J} = \mathbf{I}\hbar, \tag{W22.171}$$

where $\mathbf{I}$ is a vector of spin matrices (i.e., I_x, I_y, and I_z are square matrices). The magnitude of the angular momentum, according to quantum mechanics, is given by $\hbar[I(I+1)]^{1/2}$, where I is either a nonnegative integer or a half integer. The number of rows in the matrices I_x, I_y, or I_z is $2I+1$. For nuclei, I is small and quantum effects are important. For pedagogic reasons, however, the discussion begins with the classical theory. The quantum-mechanical treatment is covered in Appendix W22A.

A nucleus has a magnetic moment directed along the spin angular momentum vector

$$\mathbf{m} = g_I \mu_N \hbar \mathbf{I} = \hbar \gamma \mathbf{I}, \tag{W22.172}$$

where $\mu_N = e\hbar/2M_p = 5.050824 \times 10^{-27}$ J/T is the nuclear magneton, g_I is the nuclear g factor, and $\gamma = g_I \mu_N$. Each nucleus has its unique value of γ, and this is what gives NMR its chemical (and isotopic) specificity. Impose a uniform magnetic induction $\mathbf{B} = B_0 \hat{k}$ on the nucleus. The nucleus will experience a magnetic torque and this will cause the spin angular momentum to change its direction in time according to

$$\frac{d\mathbf{I}}{dt} = \frac{\mathbf{m} \times \mathbf{B}}{\hbar} = \gamma B_0 \, \mathbf{I} \times \hat{k} = \mathbf{I} \times \boldsymbol{\Omega}. \tag{W22.173}$$

This is in the form of a precession equation for $\mathbf{I}$. The precession frequency is the magnitude of the vector

$$\boldsymbol{\Omega} = \frac{\gamma \mathbf{B}}{\hbar}. \tag{W22.174}$$

TABLE W22.3 Spin $I = \frac{1}{2}$ Nuclei Commonly Used in NMR Spectroscopy

Nucleus	Isotopic Abundance (%)	f ($B = 1$ T) (MHz)
^{1}H	99.985	42.5764
^{13}C	1.10	10.7081
^{15}N	0.366	4.3172
^{19}F	100	40.0765
^{29}Si	4.67	8.4653
^{31}P	100	17.2510
^{89}Y	100	2.0949
^{109}Ag	48.161	1.9924
^{119}Sn	8.59	15.9656
^{183}W	14.3	1.7956
^{199}Hg	16.87	7.7121
^{205}Tl	70.476	24.9742
^{207}Pb	22.1	9.0338

Source: D. R. Lide, ed., *CRC Handbook of Chemistry and Physics*, 75th ed., CRC Press, Boca Raton, Fla., 1997.

A list of some nuclei commonly used in NMR, along with their precession frequencies, $f = \Omega/2\pi$ is given in Table W22.3. Many nuclei have $I = 0$ and so are not NMR-active (e.g., ^{12}C, ^{16}O, ^{28}Si, ^{56}Fe).

The effect of the electrons, which are sensitive to the chemical environment, is to partially shield the nucleus from the magnetic field. The magnetic induction may be written as

$$\mathbf{B} = (\overleftrightarrow{I} - \overleftrightarrow{\sigma}) \cdot \mathbf{B}_0, \tag{W22.175}$$

where $\overleftrightarrow{\sigma}$ is called the *shielding tensor*. It may be written as the sum of an isotropic part, $\sigma\overleftrightarrow{I}$, and an anisotropic part, $\Delta\overleftrightarrow{\sigma}$ (i.e., $\overleftrightarrow{\sigma} = \sigma\overleftrightarrow{I} + \Delta\overleftrightarrow{\sigma}$). The effect of the shielding is usually described in terms of a chemical-shift parameter, δ. The value is usually reported relative to a standard value

$$\delta = \frac{\Omega - \Omega_{\text{st}}}{\Omega_{\text{st}}} \times 10^6, \tag{W22.176}$$

where Ω_{st} is the frequency of the standard. The frequency shifts for protons typically range from 0 to 10 ppm. For ^{13}C they range up to ≈ 200 ppm. The standard used is often the tetramethylsilane (TMS) molecule, $(CH_3)_4Si$.

If the precession equation is separated into components, three equations are obtained:

$$\frac{dI_x}{dt} = \Omega I_y, \qquad \frac{dI_y}{dt} = -\Omega I_x, \qquad \frac{dI_z}{dt} = 0. \tag{W22.177}$$

It follows that I_z and I remain constant in time. The x and y components undergo a precessional motion

$$I_x = I_0 \cos \Omega t, \qquad I_y = -I_0 \sin \Omega t, \tag{W22.178}$$

where I_0 is a constant in the classical theory. The value of I_z is that appropriate to thermal equilibrium, and is given in terms of the Brillouin function:

$$\langle I_z \rangle = IB_I \left(\frac{\gamma IB}{k_B T} \right), \tag{W22.179}$$

which is analogous to Eqs. (9.23) and (9.24).

In a solid, the nuclei interact with the other atoms of the material through a variety of interactions, including spin–orbit and spin–spin interactions. These interactions have two effects. First, they cause the z component of the nuclear spin to relax to its equilibrium value, with a characteristic relaxation time T_1, that is,

$$\frac{dI_z}{dt} = -\frac{I_z - \langle I_z \rangle}{T_1}. \tag{W22.180}$$

The parameter T_1 is called the *longitudinal* or *spin-lattice relaxation time*. Second, they cause the precessional motion to become phase interrupted. Introduce a phenomenological damping term to account for this spin–lattice interaction:

$$\frac{dI_x}{dt} + \frac{I_x}{T_2} = (\mathbf{I} \times \Omega)_x, \tag{W22.181}$$

$$\frac{dI_y}{dt} + \frac{I_y}{T_2} = (\mathbf{I} \times \Omega)_y, \tag{W22.182}$$

The parameter T_2 is called the *transverse relaxation time*. It is assumed that there is no difference in the phase-interruption time constant for x- or y-spin components.

It is convenient to form the combination $I_+ = I_x + iI_y$ and combine the two precession equations into one:

$$\left(\frac{d}{dt} + i\Omega + \frac{1}{T_2} \right) I_+ = 0. \tag{W22.183}$$

This is an equation for damped oscillation of the spin.

Next, introduce the perturbing magnetic field, $\mathbf{H}'(t)$, at right angles to $\mathbf{B}$. It is taken to be circularly polarized, since this leads to a simpler formula. Thus

$$H'_x = H' \cos \omega t, \qquad H'_y = -H' \sin \omega t. \tag{W22.184}$$

The dynamical equation becomes

$$\left(\frac{d}{dt} + i\Omega + \frac{1}{T_2} \right) I_+ = i\Omega' I_z \exp(-i\omega t), \tag{W22.185}$$

where $\Omega' = \mu_0 \gamma H'/\hbar$. In the limit of weak RF fields, I_x and I_y will be small, so I_z will differ from $\langle I_z \rangle$ only by terms of order $(H')^2$. Hence I_z will be approximated by $\langle I_z \rangle$. A steady-state solution for I_+ is found by writing $I_+ = I_0 \exp(-i\omega t)$, so

$$I_0 = \frac{\Omega' \langle I_z \rangle}{\Omega - \omega - i/T_2}. \tag{W22.186}$$

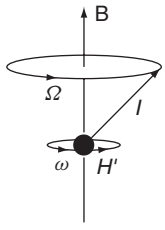

Figure W22.51. Precession of a nuclear spin around the magnetic-induction vector.

This equation demonstrates that as the frequency ω approaches the resonance frequency Ω, the amplitude of I_+ can grow to be large, limited only by the shortness of T_2. The resonance is detected by monitoring the power transfer from the RF circuit to the spin system. It shows up by adding extra inductance and resistance to the RF circuit. This power, of course, is ultimately transferred to the translational motion of the other atoms and so heats the material. A sketch of the precessing magnetic dipole is presented in Fig. W22.51.

The resonance frequency of a nucleus depends on the *local* magnetic field. In addition, for spin $I \geq 1$, nuclei also possess electric-quadrupole moments. These interact with electric fields and affect the NMR spectrum in important ways. The local magnetic field is given by the sum of the applied field and the fields due to all the other electronic and nuclear magnetic moments of the material. Since these moments are likely to be oriented in an almost random manner, each nucleus will experience a different magnetic field and hence have a different resonance frequency. Instead of the sample exhibiting a sharp NMR resonance line, the line will be inhomogeneously broadened. It is important to make a distinction between the magnetic moments participating in the resonance (such as protons interacting with other protons in an proton NMR signal) and other moments (such as protons interacting with Fe atomic spins in iron). In this example, the spin–spin interaction of the protons is approximately included in the parameter T_2. The other interactions contribute to the inhomogeneous broadening of the NMR line. This limits the ability to resolve closely spaced resonance lines.

There are at least two methods to overcome this limitation. One may do NMR on a liquid instead of a solid. There is a phenomenon called *motional line narrowing* which can occur in liquids and will now be explained. As the nuclei move about due to their thermal motion, the contribution to the local magnetic field from other nuclei is as likely to be in one direction as in the opposite direction. Its average value is zero, although the mean-square fluctuation remains nonzero. Let the contribution to the precession frequency of a given nucleus from the other magnetic dipoles of the material be denoted by $\Omega''(t)$. As a simple model, suppose that it may assume only two values, $+\Omega''$ and $-\Omega''$, and that there is a 50% probability of switching from one value to the other every τ seconds. The mean value of the square of the accumulated phase after a time t is then

$$\overline{\left[\int_0^t \Omega''(t')\,dt'\right]^2} = \frac{t}{\tau}\Omega''^2\tau^2, \tag{W22.187}$$

where t/τ is the number of opportunities for switching that occur. If the effective dephasing time is determined by when this is ≈ 1 radian, an estimate for T_2 is obtained:

$$T_2 = \frac{1}{\Omega''^2 \tau}. \tag{W22.188}$$

As the thermal motion increases, τ becomes smaller and the dephasing time becomes longer.

A second technique for reducing the inhomogeneous width is called *magic-angle spinning*. It permits high-resolution NMR to be applied to solid-state samples. It may be accomplished by either actually physically spinning the solid about an axis making an angle $\theta = 54.7^\circ$ with the dc magnetic field and using a very weak RF field, or holding the sample stationary but arranging that the ratio of the RF magnetic field to the dc magnetic field be equal to $H'/H_0 = \tan(54.7^\circ) = 2^{1/2}$. To understand how this comes about, consider the magnetic dipole–dipole interaction between the magnetic dipoles located at the various sites $\mathbf{r}_i$ in the solid:

$$U = \frac{\mu_0}{4\pi} \sum_{i=1}^{N} \sum_{j=i+1}^{N} \frac{3(\mathbf{m}_i \cdot \hat{r}_{ij})(\mathbf{m}_j \cdot \hat{r}_{ij}) - \mathbf{m}_i \cdot \mathbf{m}_j}{r_{ij}^3}, \tag{W22.189}$$

where $r_{ij} = |\mathbf{r}_i - \mathbf{r}_j|$. It will be assumed that the magnetic field is strong enough so that $\mathbf{m}_i$ precesses rapidly around the applied magnetic induction $\mathbf{B}_0$. On the average, the magnetic moment therefore points along the direction of the magnetic field. The angular factor in the numerator may then be written as

$$2P_2(\cos\theta_{ij}) = 3\cos^2\theta_{ij} - 1 = 3(\hat{B}_0 \cdot \hat{r}_{ij})^2 - 1, \tag{W22.190}$$

where $P_2(\cos\theta)$ is the second-order Legendre polynomial. Now suppose that the solid is spun around some axis with an angular velocity Ω_s (Fig. W22.52). There is an identity, called the *addition theorem for spherical harmonics*,

$$P_L(\cos\theta_{ij}) = \frac{4\pi}{2L+1} \sum_{M=-L}^{L} Y_{LM}^*(\theta, \phi) Y_{LM}(\psi_{ij}, \phi_{ij}), \tag{W22.191}$$

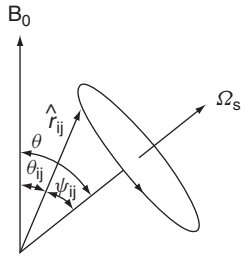

Figure W22.52. Orientation of the external magnetic field, $\mathbf{B}_0$, the displacement unit vector, $\hat{r}_{ij}$, and the rotation velocity, Ω_s.

where the Y_{LM} are spherical harmonics and ϕ denotes an azimuthal angle (not shown in the figure) around vector $\mathbf{\Omega}_s$. In the course of the angular motion, the terms involving $M \neq 0$ average out, so

$$P_2(\cos\theta_{ij}) \longrightarrow P_2(\cos\psi_{ij})P_2(\cos\theta). \tag{W22.192}$$

If $\cos^2\theta = \frac{1}{3}$ (i.e., $\theta = 54.7°$), then $P_2(\cos\theta) = 0$ and the spin–spin interaction is effectively removed as a first-order perturbation in the problem. This allows the lines to become very narrow when the solid is spun at the magic angle. It must be emphasized, however, that magic-angle spinning is only effective in eliminating the broadening due to "like" spins. It does not eliminate inhomogeneous broadening due to other sources.

It is possible to remove some dipole–dipole broadening effects due to the interactions between unlike spins by employing a technique called *dipolar decoupling*. For example, suppose that ^{1}H is present and one is interested in studying the ^{13}C spectrum. Normally, the two spins would interact in such a way as to broaden the spectra. A strong RF field is applied whose frequency resonates with the protons. The spins of the protons are made to flip up and down rapidly and hence their magnetic moments average to zero. Their interaction with the ^{13}C nuclei is suppressed.

It is also possible to use a technique called *cross-polarization* to increase the sensitivity of the NMR resonance of one of the spins of a multispin system. For example, there may be many more ^{1}H nuclei present than ^{13}C nuclei. In this technique one applies two RF frequencies which effectively lock the nuclear resonances together. This occurs when the Hahn–Hartmann condition applies (i.e., $\gamma_C B_C = \gamma_H B_H$). The Zeeman splittings of the two nuclei are made degenerate with each other, and this facilitates the resonant exchange of energy via the spin–spin interaction. The net result is a transfer of magnetization from the majority ^{1}H nuclei to the minority ^{13}C nuclei and a strengthening of the ^{13}C signal.

It should also be mentioned that in some solids the analysis of the NMR line shape reveals that the interaction between "like" spins leads to non-Lorentzian resonances. This reflects a limitation of the Bloch equations in which one attempts to parametrize all dephasing effects in terms of a single time, T_2. The measured line shape may contain important information concerning the interatomic distances and the short-range order, in general.

The relaxation time T_1 can be very long, in the range of minutes or longer. In some cases this long relaxation time limits the ability to carry out NMR experiments on solids. On the other hand, it also implies that quantum coherence is being maintained for a long period of time. This could potentially be utilized in the construction of quantum computers, which rely on the quantum-mechanical coherence being maintained during the course of a calculation.

NMR is a long-established technique and there are a variety of ways of employing it. There are powerful methods using time-programmed pulses of RF magnetic fields, but these will not be discussed here.

It is also possible to obtain information concerning the density of conduction electrons by measuring the Knight shift. At a given frequency the nuclear magnetic resonance of a nucleus in a metal occurs at a different value of the magnetic field than it would in an insulator. The Knight shift is defined as $-\Delta B/B$. This is due to the fact that the conduction electrons exhibit magnetism, and this modifies the local magnetic field experienced by the nucleus. The interaction responsible for this shift (called the

Fermi contact interaction) is a point-magnetic interaction between the electron-spin magnetic moment and the magnetic moment of the nucleus. An expression for this interaction may be obtained by regarding the nucleus as a small magnetized sphere of radius b and allowing the size of the sphere to shrink to zero. The magnetic induction inside the sphere can be shown, by elementary magnetostatic arguments, to be given by $\mathbf{B}_{\text{in}} = \mu_0 g_I \mu_N \mathbf{I}/2\pi b^3$. The interaction energy is $V = g_e \mu_B \mathbf{s} \cdot \mathbf{B}_{\text{in}}$, so

$$V = \frac{2\mu_0}{3} g_e \mu_B g_I \mu_N \mathbf{s} \cdot \mathbf{I} \delta(\mathbf{r}), \tag{W22.193}$$

g_e being the electron g factor and μ_B the Bohr magneton. The substitution $1/(4\pi b^3/3) \rightarrow \delta(\mathbf{r})$ is also made in deriving this formula. Applying first-order perturbation theory, one finds an expression for the energy of the nuclear magnetic moment in the magnetic field:

$$E = -g_I \mu_N \mathbf{I} \cdot \left[\mathbf{B} - \frac{2\mu_0}{3} g_e \mu_B \mathbf{s} |\psi(0)|^2 \right], \tag{W22.194}$$

where $|\psi(0)|^2$ is the probability density for finding the electron at the nucleus. The Knight shift, K, is therefore

$$K \equiv -\frac{\Delta B}{B} = \frac{2\mu_0 g_e \mu_B \langle s_z \rangle}{3B} |\psi(0)|^2. \tag{W22.195}$$

This may be expressed in terms of the magnetic susceptibility χ and the magnetic permeability μ using the relation $\langle s_z \rangle / B = \chi / n \mu_0 g_e \mu_B$, where n is the electron density. Typical experimental values for the Knight shift for the alkali metals ^{7}Li, ^{23}Na, ^{39}K, and ^{87}Rb are 0.026%, 0.112%, 0.265%, and 0.653%.

The Fermi contact interaction is also responsible for the relaxation of the z component of the spins. Korringa derived a relation for the spin–lattice relaxation time, based on Fermi's golden rule, in terms of the Knight shift in metals:

$$T_1 \left(\frac{\Delta B}{B} \right)^2 = \frac{\hbar g_e^2 \mu_B^2}{4\pi k_B T g_I^2 \mu_N^2} = \frac{\hbar g_e^2 M_p^2}{4\pi k_B T g_I^2 m_e^2}. \tag{W22.196}$$

In Fig. W22.53 magic-angle spinning NMR spectra are presented for ^{29}Si at 79.5 MHz from samples of the catalyst ZSM-5 discussed in Section 13.6. The spectra are compared for various degrees of removal of Al from the framework. The NMR spectra are far more sensitive to the changes in the lattice structure than are x-ray diffraction spectra. A precise determination of the lattice geometry may be obtained from NMR studies.

W22.31 Nuclear Quadrupole Resonance

Nuclei with spins greater than or equal to $\frac{1}{2}$ possess magnetic moments. If the spins are greater than 1, they also possess electrical-quadrupole moments. The quadrupole moment is a measure of the spherical asymmetry of the charge distribution of the

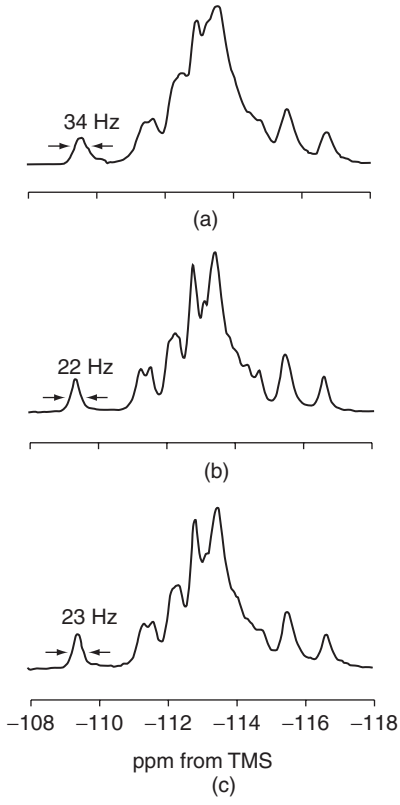

Figure W22.53. ^{29}Si magic-angle spinning NMR spectra for the zeolite ZSM-5 for various degrees of dealumination. The Si/Al ratios are: (*a*), 20; (*b*), 125; (*c*), 800. [Reprinted with permission from C.A. Fyfe et al., *J. Phys. Chem.*, **88**, 3248 (1984). Copyright 1984 by the American Chemical Society.]

nucleus. The quadrupole moment is defined in terms of the nuclear charge density $\rho(\mathbf{r})$ by

$$eQ = \int d\mathbf{r}\, \rho(\mathbf{r})(3z^2 - r^2), \tag{W22.197}$$

where the z axis is directed along the spin angular momentum vector. The sign of Q is an indicator of the shape of the nucleus, being positive for cigar-shaped nuclei and negative for pancake-shaped nuclei. Nuclei do not possess electric-dipole moments, consistent with the invariance of the strong interaction under parity reversal (and also time reversal).

The interaction of a quadrupole moment with an inhomogeneous electric field is obtained from a Taylor series expansion:

$$U = \int d\mathbf{r}\Phi(\mathbf{r})\rho(\mathbf{r}) = Ze\Phi(0) + \frac{e}{6}\sum_{\alpha,\beta}\frac{\partial^2\Phi}{\partial x_\alpha \partial x_\beta}Q_{\alpha\beta} + \cdots, \tag{W22.198}$$

where $\Phi(\mathbf{r})$ is the electrostatic potential and Z is the atomic number of the nucleus. The coefficients $Q_{\alpha\beta}$ define what is called the *quadrupole tensor*:

$$eQ_{\alpha\beta} = \int d\mathbf{r}\, \rho(\mathbf{r})(3x_\alpha x_\beta - r^2\delta_{\alpha\beta}). \tag{W22.199}$$

It is defined here so that it has the dimensions m^2 and is represented by a symmetric matrix. The only vector defined for the nucleus as a whole is the spin angular-momentum vector. Therefore, all vectors can be expressed in terms of $\mathbf{I}$, so

$$\int d\mathbf{r}\, \rho(\mathbf{r})x_\alpha x_\beta = \frac{C}{2}(I_\alpha I_\beta + I_\beta I_\alpha), \qquad \int d\mathbf{r}\, \rho(\mathbf{r})r^2 = CI^2. \tag{W22.200}$$

If the expectation values of these expressions are evaluated in the state in which $\mathbf{I}^2|I, I\rangle = I(I+1)|I, I\rangle$ and $I_z|I, I\rangle = I|I, I\rangle$, then C may readily be shown to be equal to

$$C = \frac{eQ}{I(2I-1)}. \tag{W22.201}$$

The product of the spin matrices has been written in a form that preserves the symmetry of the quadrupole tensor. (Note that angular momenta matrices need not commute with each other.) The Hamiltonian for the quadrupole interaction is

$$H_Q = \frac{C}{6}\sum_{\alpha\beta}\Phi_{\alpha\beta}\left[\frac{3}{2}(I_\alpha I_\beta + I_\beta I_\alpha) - \delta_{\alpha\beta}I^2\right], \tag{W22.202}$$

using a shorthand notation for the second derivative of the potential. After some manipulation and making use of $\nabla^2\Phi = 0$, this reduces to

$$H_Q = \frac{e^2Qq}{4I(2I-1)}\left[3I_z^2 - I^2 + \eta(I_x^2 - I_y^2)\right], \quad \Phi_{zz} \equiv eq, \quad \frac{\Phi_{xx} - \Phi_{yy}}{\Phi_{zz}} \equiv \eta, \tag{W22.203}$$

where η is called the asymmetry parameter and eqQ is called the *quadrupole-coupling parameter*. The effects of this interaction are probed in NQR experiments.

This equation shows how the nuclear spin couples to the gradient of the electric field. This field is set up by the neighboring ions and their associated electron charge distributions. The field depends on the types of neighboring atoms, the internuclear distances, and the types of chemical bonds that are formed. NQR therefore provides a useful tool for obtaining the information above.

It is not possible to create strong-enough RF laboratory electric-field gradients that can be used as the basis for NQR resonance measurements. Instead, one uses the RF magnetic field, usually in conjunction with a dc magnetic field, and looks at the simultaneous NMR and NQR effects. For example, suppose that there is a dc magnetic field directed along the z axis, and this is aligned with a symmetry axis of the crystal. In this case, $\eta = 0$. The Hamiltonian then consists of a Zeeman term and the quadrupole interaction:

$$H = -\gamma B_0 I_z + \frac{e^2Qq}{4I(2I-1)}(3I_z^2 - \mathbf{I}^2). \tag{W22.204}$$

The first-order splitting caused by such an interaction may be obtained for the eigenstates $|I, m\rangle$ as

$$\langle I, m|H|I, m\rangle = -\hbar\gamma B_0 m + \frac{e^2Qq}{4I(2I-1)}[3m^2 - I(I+1)]. \tag{W22.205}$$

The effect of the Zeeman term is to lift the degeneracy by spreading out the sublevels uniformly. The effect of the quadrupole coupling is to raise (or lower) states with $\pm m$ by the same amount. The combined effect is to produce a nonuniform spreading of the sublevels. The magnetic-dipole selection rule is $\Delta m = \pm 1$. The transitions may be tracked in a resonance experiment, and the value of eqQ may be obtained to high precision.

For the case where there is no axial symmetry the formulas are more complicated. For $I = 1$ one finds that

$$\langle 1, m|H|1, m\rangle = \begin{cases} -\dfrac{e^2}{2}qQ & \text{if} \quad m = 0, \\ \mp\gamma B_0 + \dfrac{e^2qQ}{4}(1 \pm \eta), & \text{if} \quad m = \pm 1, \end{cases} \tag{W22.206}$$

and for $I = \frac{3}{2}$ one finds that

$$\left\langle \frac{3}{2}, m|H|\frac{3}{2}, m\right\rangle = \begin{cases} \mp\dfrac{\gamma B_0}{2} + \dfrac{e^2}{4}qQ\sqrt{1+\eta^2/3}, & \text{if} \quad m = \pm\dfrac{1}{2}, \\ \mp\dfrac{3\gamma B_0}{2} - \dfrac{e^2qQ}{4}\sqrt{1+\eta^2/3}, & \text{if} \quad m = \pm\dfrac{3}{2}. \end{cases} \tag{W22.207}$$

Typical values of Q are presented in Table W22.4, along with nuclear spins, abundances, and Zeeman (precession) frequencies for magnetic-dipole transitions. Nuclear quadrupole resonance provides information about bond hybridization and the covalent nature of the chemical bond. For example, if there is sp-hybridization, only the p-orbital contributes to the quadrupole moment. Similarly, in ionic bonding, the closed-shell ions do not possess quadrupole moments.

TABLE W22.4 Spins, Abundances, Precession Frequencies, and Quadrupole Moments for Some Nuclei

Nucleus	Spin I	Isotopic Abundance (%)	$f(B = 1\ \text{T})$ (MHz)	Q (10^{-30} m^2)
^{2}H	1	0.015	42.5764	0.2860
^{11}B	$\frac{3}{2}$	80.1	13.6626	4.059
^{17}O	$\frac{5}{2}$	0.038	5.7741	−2.558
^{25}Mg	$\frac{5}{2}$	10.00	2.6082	19.94
^{27}Al	$\frac{5}{2}$	100	11.1028	14.03

Source: Data from D. R. Lide, ed., *CRC Handbook of Chemistry and Physics*, 75th ed., CRC Press, Boca Raton, Fla., 1997.

W22.32 Electron-Spin Resonance

Much of the inner workings of atoms has been elucidated by employing resonance techniques in conjunction with the use of external magnetic fields. The physics of the atom is described in terms of a succession of contributions to the Hamiltonian. These describe the kinetic energy, the electrostatic interaction between the electrons and the nucleus, the electron–electron electrostatic interactions, the spin–orbit coupling, the spin–spin interaction, the interaction of the electron orbital angular momentum $\mathbf{L}$ and spin $\mathbf{S}$ with external magnetic fields, the hyperfine interaction, the nuclear Zeeman and quadrupole couplings, and various relativistic and quantum-electrodynamic corrections. If the atom is not free but is embedded in a crystal, one must, in addition, consider the effect of the crystal electric field imposed by the neighboring ions and electrons, the interaction of the atomic spin with the spins on nearby atoms, and the possibility of losing electrons to or gaining electrons from other atoms of the solid. These effects are often by no means small and lead to major perturbations of the energy levels and the corresponding spectroscopy. To the extent that they can be understood, however, they provide a powerful analytical tool for probing the solid. The field is called *electron-spin resonance* (ESR) or sometimes *electron paramagnetic resonance* (EPR). For simple electron-spin systems, ESR may be described in terms of the Bloch equations, although the quantum-mechanical approach is used in this section.

ESR is a very rich field and cannot be summarized adequately in a short amount of space. It can provide information concerning donor or acceptor impurities in semiconductors. It can be used to study transition metal ions. It is useful for analyzing color centers in insulators. It is sensitive to electron and hole traps. There are two simple uses for it: determining the symmetry of the site where the spin sits and determining the valence of the magnetic ion.

In atomic physics one is concerned with the coupling of the nuclear spin, $\mathbf{I}$, to the electronic spin, $\mathbf{J} = \mathbf{L} + \mathbf{S}$, to form a total angular momentum $\mathbf{F} = \mathbf{I} + \mathbf{J}$. In the presence of a magnetic induction $\mathbf{B} = \hat{k}B_0$, the Hamiltonian for a given electronic term is written as

$$H = \lambda \mathbf{L} \cdot \mathbf{S} + \mu_B \mathbf{B} \cdot (\mathbf{L} + g\mathbf{S}) + A\mathbf{S} \cdot \mathbf{I} + \mu_N \mathbf{B} \cdot \mathbf{I}, \tag{W22.208}$$

where the first term is the spin–orbit coupling, the second term is the electronic Zeeman effect, the third term represents the hyperfine coupling, and the last term is the nuclear Zeeman effect (which is three orders of magnitude weaker). The parameter g is the g factor of the electron and is approximately 2. One usually forms matrix elements of this Hamiltonian in an appropriate basis, diagonalizes the matrix, and interprets the eigenvalues as the energy levels. Resonance spectroscopy may then be used to drive transitions between the energy levels and therefore to deduce the coupling constants, λ and A, as well as to determine L, S, and I.

The same basic idea is used in the solid, but the Hamiltonian becomes more complicated. First, quenching of the orbital angular momentum may occur. This occurs in the sp-bonded materials and transition metal ions (but not in the rare earths with f electrons, which need to be considered separately). Since the crystal is not an isotropic medium, the mean orbital angular momentum operator does not commute with the potential energy function. On the other hand, to a first approximation, the electron and nuclear spins are impervious to the presence of this anisotropy. In place of the full rotational symmetry of the free atom, there is the point-group symmetry of the crystal.

A fruitful approach is to try to write a Hamiltonian operator involving **S**, **I**, and **B** in a form that will respect the symmetry operations of the crystal. This will often require introducing more than two arbitrary constants. Resonance techniques are able to determine these parameters in the same way as they are determined for a free atom. The size of the parameters often offers important clues to the nature of the chemical bonds formed. Moreover, a study of the degeneracies and their lifting under the application of a magnetic field allows valuable information concerning the valency and symmetry of the paramagnetic ions to be obtained.

As an example, consider the case of a magnetic ion sitting on a site with octahedral symmetry inside a cubic host crystal. The Hamiltonian may be written as

$$H = g\mu_B \mathbf{B} \cdot \mathbf{S} + A\mathbf{S} \cdot \mathbf{I} + C(S_x^4 + S_y^4 + S_z^4) + D(S_x^6 + S_y^6 + S_z^6) + \cdots, \quad \text{(W22.209)}$$

where the higher-order terms are usually smaller than the lower-order terms and are often neglected. This Hamiltonian respects the cubic symmetry of the crystal in that the permutation $x \to y \to z \to x$ is a symmetry operation (rotations of 120° around the main diagonal), as is $x \to -x$ (reflections in bisecting planes), $(x, y) \to (y, -x)$ (90° rotations), and so on.

Now suppose that a tetragonal distortion is introduced in the crystal. The x and y lattice constants are assumed to remain the same, but the z lattice constant is made different. This introduces new parameters into the Hamiltonian:

$$\begin{aligned} H = {} & g_z\mu_B S_z B_z + g_{xy}\mu_B[S_x B_x + S_y B_y] + A_z S_z I_z \\ & + C' S_z^2 + A_{xy}[S_x I_x + S_y I_y] + P\left[I_z^2 - \tfrac{1}{3}I(I+1)\right], \end{aligned} \quad \text{(W22.210)}$$

where higher-order terms have been dropped.

If the symmetry is lifted further, by creating an orthorhombic distortion, the Hamiltonian is expanded even further:

$$\begin{aligned} H = {} & g_z\mu_B S_z B_z + g_x\mu_B S_x B_x + g_y\mu_B S_y B_y + A_z S_z I_z + A_x S_x I_x + A_y S_y I_y \\ & + P[I_z^2 - \tfrac{1}{3}I(I+1)] + C' S_z^2 + C''(S_x^2 - S_y^2). \end{aligned} \quad \text{(W22.211)}$$

A typical lifting of the degeneracy is represented in Fig. W22.54 for the case of a d-shell electron. The ten-fold degenerate level for the free ion is split in stages and ultimately consists of five doubly degenerate levels.

In Fig. W22.55 results are presented for a Mn^{2+} ion in a calcite host crystal, $CaCO_3$. In the presence of the magnetic field the $S = 5/2$ level is Zeeman-split into $2I + 1 = 6$ lines. The widths of the lines are attributed mainly to random strains in the crystal.

W22.33 Mössbauer Spectroscopy

Consider the gamma decay of an isolated radioactive nucleus in an excited state I resulting in a ground-state nucleus F. A gamma ray of energy $\hbar\omega$ is emitted in one direction and nucleus F recoils with momentum $\hbar\omega/c$ in the opposite direction. The total energy available in the transition is the sum of the photon energy and the recoil energy: $E = \hbar\omega + (\hbar\omega)^2/2Mc^2$, where M is the nuclear mass. The photon that is emitted cannot be absorbed by another F nucleus, because it is shifted out of resonance (i.e., $\hbar\omega < E$).

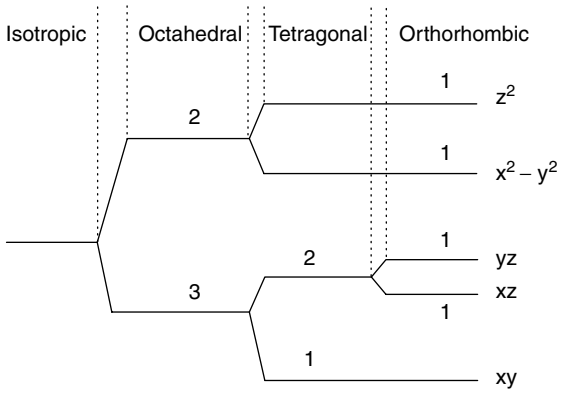

Figure W22.54. Lifting of the degeneracy of the d-electron energy levels as the symmetry of the crystal is lowered.

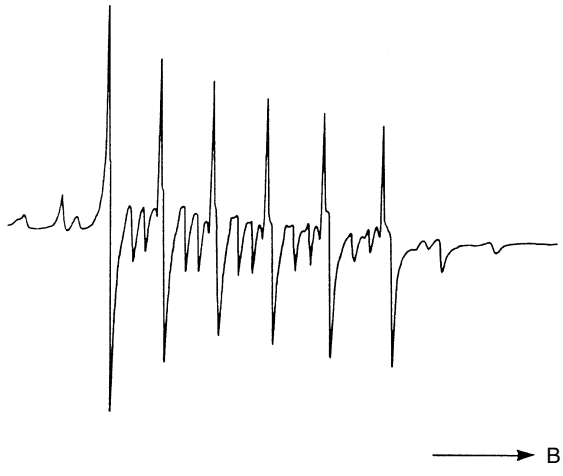

Figure W22.55. ESR spectrum of a Mn^{2+} ion in a calcite host. [Reprinted from J. G. Angus et al, *Chem. Geol.*, **27**, 181 (1979). Copyright 1979, with permission from Elsevier Science.]

The natural width of the emission line, determined by its radiative lifetime, is typically on the order of several 10^{-9} eV, much smaller than the recoil energy. There are only several nuclei that may be used in Mössbauer spectroscopy. Chief among them is ^{57}Fe. The parent nucleus is ^{57}Co. The sequence of decays is $^{57}\text{Co} \rightarrow {}^{57}\text{Fe}^* + e^-$, with a half-life of 271 days, followed by $^{57}\text{Fe}^* \rightarrow {}^{57}\text{Fe} + \gamma$, with a half-life of 99.3 ns. The energy of the gamma ray used in Mössbauer spectroscopy is 14.41 keV, although there are two others emitted at 123 and 137 keV. Other useful emitters are ^{119}Sn, ^{121}Sb, ^{125}Te, ^{129}I, ^{151}Eu, ^{190}Os, and ^{197}Au.

Gamma decay often involves a change in the nuclear spin. Due to the hyperfine interaction there may be several possible values for $\hbar\omega$.

Next consider the nucleus embedded in a crystal, which will be called the *source crystal*. In the discussion of the Debye–Waller factor, $\exp(-2W)$, the factor was interpreted as the probability for the crystal to be found in a periodic arrangement. If the

crystal is periodic, when one atom moves, all atoms must move. Energy conservation requires $E = \hbar\omega + (\hbar\omega)^2/2NMc^2$, where N is the number of atoms in the crystal. For a macroscopic sample the second term is negligible and so it is safe to write $E = \hbar\omega$.

Suppose that an attempt is made to absorb the gamma ray using a second crystal. The absorption process is one in which the inverse process takes place (i.e., $F + \hbar\omega \rightarrow I$). In general, this too will involve nucleus I recoiling upon absorption, and even if $E = \hbar\omega$, it would not have sufficient energy to cause the transition. However, recoilless absorption is also possible. The probability for this is given by a Debye–Waller factor for the absorbing crystal. The conclusion is that it is possible to have resonant energy transfer from one crystal to the other. This is the Mössbauer effect.

By moving one crystal relative to the other, the gamma rays are Doppler shifted. This may drive the crystals out of resonance again. Thus, if the absorber is moved toward the source at velocity v, it sees a gamma ray at frequency $\omega' = \omega[(1 + v/c)/(1 - v/c)]^{1/2} \approx \omega(1 + v/c)$. By gradually increasing v and monitoring the transmitted gamma rays through the absorbing crystal, it is possible to carefully map out the line shape of the gamma ray and hyperfine structure of the nucleus.

The utility of the Mössbauer effect is that the line shape and hyperfine splittings provide information concerning the local electronic environment of the nucleus. One compares the energy levels in the source with those of the absorber. Each is subject to a chemical shift (also called an *isomer shift*) determined, for example, by its oxidation state. The Mössbauer spectrum also provides information about the magnetic fields and spins in the solid. Thus information is provided in a similar fashion to that obtained from NMR or NQR studies. For example, one may obtain the quadrupole splitting, as in NQR. In the case of ^{57}Fe, with $I = \frac{3}{2}$, the quadrupole splitting is given by the formula $\Delta E = (e^2qQ/2)\sqrt{1 + \eta^2/3}$ [see Eq. (W22.207)]. From a measurement of the Zeeman splitting, one may determine the strength of the magnetic induction, B, at the nucleus.

An example of a Mössbauer spectrum is presented in Fig. W22.56. The gamma-ray source is $Mg_3^{125}Te^mO_6$ (with a 58-day half-life) and the absorber is ZnTe. The recoilless fraction depends on the Debye–Waller factor, $\exp[-2W(T)]$. Equation (W5.13)

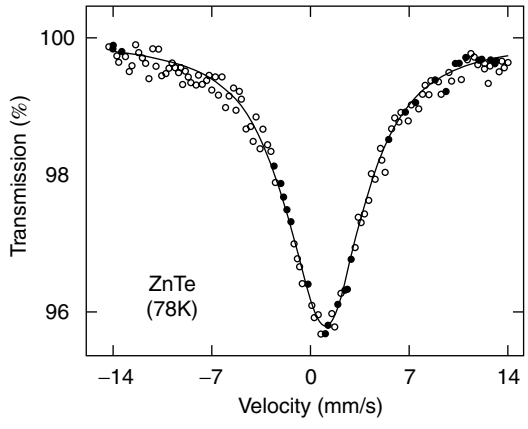

Figure W22.56. Mössbauer spectrum produced with the metastable source $Mg_3^{125}Te^m$-O_6 and the absorber ZnTe at $T = 78$ K. [From W. Bresser et al, *Phys. Rev. B*, **47**, 11663 (1993). Copyright 1993 by the American Physical Society.]

gives an expression for $W(T)$ which may be evaluated using the Debye theory used to calculate the specific heat of solids. Thus W will also depend parametrically on the Debye temperature Θ_D. By studying the Mössbauer signal as a function of temperature, it is possible to determine Θ_D. A value $\Theta_D = 188$ K is found for the absorber.

ELEMENTARY PARTICLES

The final sections of the characterization chapter are concerned with two techniques that rely on elementary particles other than the familiar ones of ordinary matter. They are positron-annihilation spectroscopy and muon-precession spectroscopy.

W22.34 Positron-Annihilation Spectroscopy

The positron is the antiparticle of the electron, with the same mass and spin but opposite charge and magnetic moment (relative to the spin). When positrons come together with electrons, pair annihilation occurs. If the pair is in a spin-singlet state and is at rest, two 0.511-MeV gamma rays are emitted in opposite directions. If the pair is in a triplet state, three gamma rays are emitted, the sum of the energies adding up to the total rest energy of 1.022 MeV. The rate for singlet decay is much faster than for triplet decay.

In positron-annihilation spectroscopy (PAS) a beam of positrons is directed at a solid and the resulting gamma-ray distribution is analyzed. Three popular ways of analyzing the data are to:

1. Measure the time decay of the gamma-ray signal
2. Measure the angular correlation of the gamma rays
3. Measure the energy distribution of the gamma rays

Typical positron sources include ^{22}Na ($\tau_{1/2} = 2.6$ years, $E = 0.54$ MeV) and ^{68}Ge ($\tau_{1/2} = 280$ days, $E = 1.89$ MeV), where E is the energy of the positron. Accelerators are also often used. The positrons are rapidly thermalized after entering the solid by making frequent collisions with the electrons and sharing their energy and momentum with them. The thermalization time is typically 25 ps. The penetration "depth" with 1% survival against annihilation is $\rho d = 10$ kg/m^2 for a 2-MeV positron, which translates into approximately 0.003 m for Al, where $\rho = 2700$ kg/m^3. A typical positron lifetime in a metal (Mg) is 232 ps.

Positrons, being positively charged, avoid the regions of high positive potential inside an atom and thus tend to settle as far from the nuclei as possible. If open-volume defects such as voids or vacancies are present, the emitted positrons are likely to settle there. Trapping can also occur in dislocations. PAS therefore provides a powerful method for studying these defects in a crystal. The decay rate per unit volume is proportional to the probability that both the electron and positron are to be found in that volume. If the positron is in a vacancy instead of being inside a normal region of the crystal, this joint probability can be expected to be lower than its normal value and hence the decay rate will also be different. The decay of the gamma-ray signal in time will also be modified. This effect may be modeled by simple kinetic equations, as follows.

Let n_f be the number of free positrons per unit volume and n_t be the corresponding number of trapped positrons per unit volume. Let the decay rate for a free positron be Γ_f and for a trapped positron be Γ_t. Let C be the concentration of traps, σ_t the trapping cross section, and v the positron speed. The rate of change of the free-positron density is given by

$$\frac{dn_f}{dt} = -\Gamma_f n_f - C\sigma_t v n_f. \tag{W22.212}$$

The rate of change of the trapped-positron density is

$$\frac{dn_t}{dt} = C\sigma_t v n_f - \Gamma_t n_t. \tag{W22.213}$$

Begin by injecting a pulse of free positrons at time $t = 0$, so

$$n_f(0) = n_0, \qquad n_t(0) = 0. \tag{W22.214}$$

The kinetic equations are readily integrated to give

$$n_f(t) = n_0 \exp[-(\Gamma_f + C\sigma_t v)t], \tag{W22.215}$$

$$n_t(t) = \frac{c\sigma_t v n_0}{\Gamma_f - \Gamma_t + c\sigma_t v}\{\exp(-\Gamma_t t) - \exp[-(\Gamma_f + c\sigma_t v)t]\}. \tag{W22.216}$$

The rate of gamma-ray production per unit volume is

$$\begin{aligned}\frac{dn_\gamma}{dt} &= n_t\Gamma_t + n_f\Gamma_f \\ &= n_0\frac{(\Gamma_f - \Gamma_t)(\Gamma_f + C\sigma_t v)}{\Gamma_f - \Gamma_t + C\sigma_t v}\exp[-(\Gamma_f + Cv\sigma_t)t] \\ &\quad + n_0\frac{C\sigma_t v\Gamma_t}{\Gamma_f - \Gamma_t + C\sigma_t v}\exp(-\Gamma_t t).\end{aligned} \tag{W22.217}$$

The exponents and amplitudes multiplying the exponentials may be extracted by fitting the time-resolved gamma-ray decay rate to a two-exponential fit.

PAS may be used to obtain information about the distribution of electrons in momentum space. In a metal the electrons fill the Fermi sea and therefore have a momentum distribution whose maximum value is determined by the Fermi energy and the band structure. The wavefunction of the electron at the location of the positron may be expanded in momentum eigenstates. The square of the expansion coefficient gives the probability of finding the electron with that momentum at the positron. The physics follows from elementary conservation laws.

Let the momentum of the electron be $\mathbf{p}$, the wave vectors of the gamma rays be $\mathbf{k}_1$ and $\mathbf{k}_2$, and the momentum of the thermalized positron be approximated by 0. Momentum conservation gives

$$\hbar[\mathbf{k}_1 + \mathbf{k}_2] = \mathbf{p}. \tag{W22.218}$$

Energy conservation gives

$$mc^2 + E = mc^2 + \sqrt{m^2c^4 + c^2p^2} = \hbar(\omega_1 + \omega_2), \tag{W22.219}$$

where E is the energy of the electron. The gamma-ray dispersion formulas are essentially those in vacuum,

$$\omega_1 = k_1 c, \qquad \omega_2 = k_2 c. \tag{W22.220}$$

Eliminating ω_1 and ω_2 leads to

$$\hbar(k_1 + k_2) = mc + \sqrt{p^2 + (mc)^2}, \tag{W22.221}$$

$$\hbar^2(k_1^2 + k_2^2 + 2k_1 k_2 \cos\theta) = p^2. \tag{W22.222}$$

where θ is the angle between $\mathbf{k}_1$ and $\mathbf{k}_2$. Solving for k_1 yields

$$\hbar k_1 = \frac{1}{2c}\left| mc^2 + E \pm \sqrt{(mc^2 + E)\left(E + mc^2 - \frac{4mc^2}{1 - \cos\theta}\right)}\right|. \tag{W22.223}$$

For the solution to be real, this formula must have a nonnegative argument for the square root. This implies that

$$1 - \cos\theta \geq \frac{4}{1 + \sqrt{1 + (p/mc)^2}}. \tag{W22.224}$$

Let $\theta = \pi - \delta$ and assume that δ is small. Then this becomes

$$-\frac{p}{mc} \leq \delta \leq \frac{p}{mc}. \tag{W22.225}$$

If there is a distribution in p values this equation implies that there will be a distribution in values of δ or, equivalently, of θ. The momentum distribution of the electrons in the solid may therefore be probed by measuring the angular-correlation function of the gamma rays.

Another way to measure the momentum distribution is to keep θ fixed at π and to measure the energy distribution of the gamma rays. Thus

$$\hbar k_1 = \frac{1}{2}\left(mc + \frac{E}{c} \pm p\right). \tag{W22.226}$$

Taking the nonrelativistic limit gives

$$\hbar\omega_1 = mc^2 \pm \frac{pc}{2}, \tag{W22.227}$$

which shows that a momentum value determines two values for the energy. The distribution of gamma-ray energies may be mapped into a distribution of electron momenta.

Thermalized positrons are emitted from the surfaces of metals as a result of the negative work functions presented by these metals to positrons, W_+. Some examples are $W_+ = -0.16$ eV for Al(100); $W_+ = -3.0$ eV for W(100) and W(110); $W_+ = -0.14$ eV for Cu(110); $W_+ = -0.33$ eV for Cu (111); and $W_+ = -1.3$ eV for Ni(100). The origin of these negative work functions is largely due to the surface

dipole layer that exists near the surfaces of metals. The positrons that are able to diffuse close to the surface are ejected with a distribution of kinetic energies centered around the negative of the work function. The width of the distribution is determined by the temperature of the solid. The angular distribution of the emitted positrons is sharply peaked around the surface normal when the surface is atomically flat and clean. For example, the full width at half maximum for W(100) positrons is $\approx 30^\circ$. Adsorbates on the surface broaden the emission cone. The emitted positrons may also display inelastic energy-loss peaks due to the excitation of surface adsorbates, much as is seen in LEELS experiments involving electrons.

Trapping of positrons by vacancies alters their decay rate, and this can be used to probe the thermal formation of vacancies in the interior of a solid. Positrons have also found use in studying multilayer interfaces and in depth profiling.

In addition to positron emission it is also possible for positronium (Ps) to be emitted. Positronium is a hydrogenic system consisting of a bound electron and positron. The binding energy of the ground state is 6.8 eV. The presence of surface defects, such as steps or vacancies, alters the emission rate for Ps.

Figure W22.57 gives an example of the electron momentum distribution obtained from the angular correlation of annihilation radiation of positrons in Cu (lower curve).

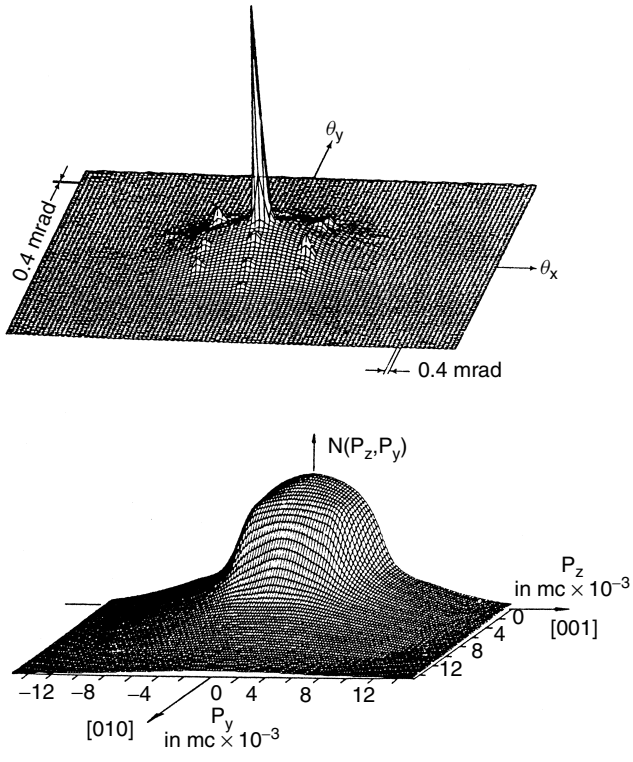

Figure W22.57. Momentum distribution of electrons obtained from studying the angular correlation of annihilation of positrons in Cu (lower curve) and the annihilation of *para*-Ps in single-crystal quartz (upper curve). [From P. J. Schultz and K. G. Lynn, *Rev. Mod. Phys.*, **60**, 701 (1988). Copyright 1988 by the American Physical Society.]

Also shown is the electron momentum distribution in single-crystal quartz (upper curve) obtained from the angular correlation of gamma rays from *para*-Ps. In Cu there is a high Fermi energy, so there is a broad distribution of electron momenta. The momentum distribution provides direct information concerning the wavefunction of the electrons in solids.

W22.35 Muon-Precession Spectroscopy

Muon precession spectroscopy (μPS) permits one to measure the spatial inhomogeneity of the magnetic field inside a material. Muons are created in an accelerator by colliding energetic particles with nuclei. At first π^+ mesons are produced, but these decay into μ^+ mesons (muons) and ν_μ neutrinos. The muons are created in a state of negative helicity (i.e., their spins point opposite to their momenta). In one type of experiment the muons enter the sample perpendicular to an external magnetic field. The implantation energy is typically 50 MeV. They rapidly slow down to an energy of 2 to 3 keV in approximately 0.1 to 1 ns. At this point they capture an electron from the material and form muonium. Muonium has the same properties as hydrogen, except the muon replaces the proton. The muonium is rapidly deexcited, on a time scale of 0.5 ps, achieving a kinetic energy of 15 eV. In another picosecond it thermalizes. Despite the fact that the muon has undergone all this deceleration and capture, the spin direction of the muon remains unchanged. The mean lifetime of the muon against decay, $\tau = 2.22$ μs, is long compared to the processes above.

The muons precess around the direction of the magnetic induction vector $\mathbf{B}_0$ at a frequency

$$\Omega(\mathbf{r}) = \frac{\mu_B B_0(\mathbf{r})}{\hbar} \frac{m_e}{m_\mu} g_\mu. \tag{W22.228}$$

Here μ_B is the Bohr magneton, m_μ the muon mass, and the g factor for the muon is $g_\mu \approx 2$. The local precession angle is $\Omega(\mathbf{r})t$. When the muon finally does decay by the process

$$\mu^+ \longrightarrow e^+ + \overline{\nu_\mu} + \nu_e, \tag{W22.229}$$

the positron e^+ is emitted preferentially along the direction of the muon-spin vector (consistent with the nonconservation of parity). The fraction of muons that live to time t is $\exp(-t/\tau)$. The product positrons are detected with sufficient angular resolution to determine the direction in which the muon spin was pointing at the time of its decay. The positron signal varies with angle and time as

$$S(\theta, t) = N_0 \exp\left(-\frac{t}{\tau}\right)[1 + A\cos(\Omega t - \theta)]. \tag{W22.230}$$

The penetration depth of the muons is large compared with the sample size, D, so only a small fraction of the muons are actually captured, but they populate the sample uniformly.

If there is a distribution of magnetic fields inside the material, there will be a distribution of precession frequencies and the angular distribution of the signal will become dephased. The time over which this occurs is a measure of the spatial inhomogeneity of the magnetic field.

Muon precession has been used to determine the local magnetic fields in antiferromagnetic materials and in ferromagnetic transition metals. It has also provided information concerning the penetration depth of magnetic fields into superconductors.

Appendix W22A: Quantum-Mechanical Description of NMR

In the development of the quantum theory of NMR in this section, the scope is limited to the case of a nucleus with spin $I = \frac{1}{2}$. Choose the quantization axis along the direction of the dc magnetic field and define it as the z direction. There are two states for the system, spin up and spin down. The time-dependent Schrödinger equation is

$$H\psi = i\hbar\frac{\partial\psi}{\partial t}, \tag{W22A.1}$$

where H is the Hamiltonian governing the system and ψ is a two-component vector with time-dependent components:

$$\psi(t) = \begin{bmatrix} u(t) \\ v(t) \end{bmatrix}. \tag{W22A.2}$$

The components $u(t)$ and $v(t)$ give the amplitudes for being in the spin-up and spin-down states, respectively. Introduce a two-dimensional matrix called the *density matrix* ρ, defined by

$$\rho = \langle\psi\psi^{+}\rangle, \tag{W22A.3}$$

where ψ^{+} is a row vector whose elements are the complex conjugates $u^{*}(t)$ and $v^{*}(t)$. The average is taken over an ensemble of ways of preparing the same state, but with different phases. Note that the density matrix is described by a Hermitian matrix (i.e., $\rho = \rho^{+}$). Also, the sum of the diagonal matrix elements of ρ (the *trace*, abbreviated $\mathrm{Tr}\rho$) is 1, since $|u|^2 + |v|^2 = 1$. It may be expanded in terms of the Pauli spin matrices, which form a basis for expanding an arbitrary 2×2 Hermitian matrix:

$$\rho = \tfrac{1}{2}[I_2 + P_x(t)\sigma_x + P_y(t)\sigma_y + P_z(t)\sigma_z] = \tfrac{1}{2}[I_2 + \boldsymbol{\sigma}\cdot\mathbf{P}(t)], \tag{W22A.4}$$

where $\mathbf{P}(t)$ is a real polarization vector and where the matrices are

$$I_2 = \begin{bmatrix} 1 & 0 \\ 0 & 1 \end{bmatrix}, \quad \sigma_x = \begin{bmatrix} 0, & 1 \\ 1 & 0 \end{bmatrix}, \quad \sigma_y = \begin{bmatrix} 0 & -i \\ i & 0 \end{bmatrix}, \quad \sigma_z = \begin{bmatrix} 1 & 0 \\ 0 & -1 \end{bmatrix}. \tag{W22A.5}$$

This form for ρ is manifestly Hermitian and obeys the trace condition $\mathrm{Tr}\rho = 1$. It follows from the Schrödinger equation that the density matrix obeys the equation

$$H\rho - \rho H = [H, \rho] = -i\hbar\frac{\partial\rho}{\partial t}. \tag{W22A.6}$$

The square bracket in this equation is called the *commutator*.

In a uniform magnetic field the Hamiltonian consists of the magnetic interaction of the dipole with the magnetic field, that is, the Zeeman interaction

$$H_0 = -\mathbf{m} \cdot \mathbf{B} = -\frac{\gamma}{2} B\sigma_Z = -\frac{\hbar}{2}\Omega\sigma_z. \tag{W22A.7}$$

There are two eigenfunctions of the time-independent Schrödinger equation $H_0\psi = E\psi$:

$$\psi_- = \begin{bmatrix} 1 \\ 0 \end{bmatrix}, \qquad \psi = \begin{bmatrix} 0 \\ 1 \end{bmatrix}, \tag{W22A.8}$$

with the corresponding eigenvalues

$$E_- = -\frac{\hbar\Omega}{2}, \qquad E = +\frac{\hbar\Omega}{2}, \tag{W22A.9}$$

where $\Omega = \gamma B/\hbar$. Suppose that the system is in thermal equilibrium at some temperature T. The Boltzmann probability for occupying the states with energy E_+ and E_- are

$$P_+ = \frac{\exp(-\beta E_+)}{\exp(-\beta E_+) + \exp(-\beta E_-)}, \quad P_- = \frac{\exp(-\beta E_-)}{\exp(-\beta E_+) + \exp(-\beta E_-)}, \tag{W22A.10}$$

where $\beta = 1/k_B T$. The density matrix corresponding to this thermal distribution is

$$\rho^0 = \frac{\exp(-\beta H_0)}{\mathrm{Tr}[\exp(-\beta H_0)]}. \tag{W22A.11}$$

In terms of the polarization vector introduced in Eq. (W22A.4), the components are

$$P_z^0 = \tanh\frac{\beta\hbar\Omega}{2}, \qquad P_x^0 = 0, \quad P_y^0 = 0. \tag{W22A.12}$$

Next introduce the rotating RF magnetic field B', as before. The Hamiltonian is

$$H = -\boldsymbol{\mu} \cdot [\mathbf{B} + \mathbf{B}'(t)] = -\frac{\hbar}{2}\Omega\sigma_z - \frac{\hbar}{2}\Omega'(\sigma_x \cos\omega t - \sigma_y \sin\omega t), \tag{W22A.13}$$

where $\Omega' = \gamma B'/\hbar$. Inserting this into the time-dependent Schrödinger equation leads to the following three equations:

$$i\dot{P}_z = -\frac{\Omega'}{2}[P_+ \exp(i\omega t) - P_- \exp(-i\omega t)], \tag{W22A.14a}$$

$$i\dot{P}_- = -\Omega P_- + \Omega' P_z \exp(i\omega t), \tag{W22A.14b}$$

$$i\dot{P}_+ = \Omega P_+ - \Omega' P_z \exp(-i\omega t), \tag{W22A.14c}$$

where

$$P_+ = P_x + iP_y, \qquad P_- = P_x - iP_y. \tag{W22A.15}$$

Next include the interaction with the other atoms of the system. The diagonal components of the density matrix represent the probabilities for being in the upper or lower state. These are taken to relax to the thermal values with a time constant called T_1. In place of Eq. (W22A.14*a*) is

$$\dot{P}_z + \frac{P_z - P_z^0}{T_1} = i\frac{\Omega'}{2}[P_+ \exp(i\omega t) - P_- \exp(-i\omega t)]. \tag{W22A.16}$$

The x and y components of the density matrix represent what are called *coherence terms*. These will also relax from their nonequilibrium values with a time constant called the *dephasing time*, T_2. Thus the following generalizations of Eqs. (W22A.14*b*) and (W22A.14*c*), including relaxation, are

$$\dot{P}_- + \frac{P_-}{T_2} = i\Omega P_- - i\Omega' P_z \exp(i\omega t), \tag{W22A.17a}$$

$$\dot{P}_+ + \frac{P_+}{T_2} = -i\Omega P_+ + i\Omega' P_z \exp(-i\omega t). \tag{W22A.17b}$$

These three formulas are called the *Bloch equations*. They are similar in form to the classical equations derived earlier [see Eqs. (W22.181) and (W22.182)]. To find a steady-state solution, let

$$P_+ = F_+ \exp(-i\omega t), \qquad P_- = F_- \exp(i\omega t) \tag{W22A.18}$$

and obtain

$$F_+ = \frac{\Omega' P_z}{\Omega - \omega - i/T_2}, \qquad F_- = \frac{\Omega' P_z}{\Omega - \omega + i/T_2}, \tag{W22A.19}$$

where

$$P_z = P_z^0 \frac{(\Omega - \omega)^2 T_2^2 + 1}{(\Omega - \omega)^2 T_2^2 + (1 + T_1 T_2 \Omega'^2)}. \tag{W22A.20}$$

This expression demonstrates that the probability of finding the system in the upper-energy state is increased above that expected at thermal equilibrium. The probability of finding the system in the lower-energy state is decreased correspondingly. The maximum increase occurs at resonance, when $\omega = \Omega$. The full-width at half maximum of the resonance is

$$\Delta\omega = \frac{2}{T_2}\sqrt{1 + T_1 T_2 \Omega'^2}. \tag{W22A.21}$$

By studying the behavior of $\Delta\omega$ as a function of Ω' it is possible to extract the parameters T_1 and T_2.

Since the populations of atoms in the upper and lower energy levels change as the RF frequency is varied, the magnetic energy of nuclei must also change. This energy must have come from somewhere. Since a dc magnetic field is incapable of supplying energy, it must have come from the RF field. The RF oscillator supplying the RF field experiences an added resistive and inductive component in the resonant circuit. This

may be monitored electronically, and the location of the resonance frequency may be determined.

REFERENCES

General

Brundle, C. R., C. A. Evans, Jr., and S. Wilson, eds., *Encyclopedia of Materials Characterization*, Butterworth-Heinemann, Boston, 1992.

Bulletin of the Materials Research Society.

Kane, P. F., and G. B. Larrabee, eds., *Characterization of Solid Surfaces*, Plenum Press, New York, 1974.

Wachtman, J. B., *Characterization of Materials*, Butterworth-Heinemann, Boston, 1993.

X-ray Diffraction

Cullity, B. D., *Elements of X-ray Diffraction*, 2nd ed., Addison-Wesley, Reading, Mass., 1978.

Suryanarayana, C., and M. B. Norton, *X-ray Diffraction: A Practical Approach*, Plenum Press, New York, 1998.

Zachariasen, W. H., *Theory of X-ray Diffraction in Crystals*, Wiley, New York, 1945.

LEED

Brundle, C. R., *Electron Spectroscopy: Theory, Techniques and Applications*, Academic Press, San Diego. Calif., 1977.

Pendry, J. B., *Low Energy Electron Diffraction: The Theory and Its Application to Determination of Surface Structure*, Academic Press, San Diego, Calif., 1974.

Sevier, K. D., *Low Energy Electron Spectrometry*, Wiley-Interscience, New York, 1972.

van Hove, M. A., W. H. Weinberg, and C. M. Chan, *Low-Energy Electron Diffraction: Experiment, Theory, and Surface Structure Determination*, Springer-Verlag, Berlin, 1986.

RHEED

Larsen, P. K., and P. J. Dobson, eds., *Reflection High-Energy Electron Diffraction and Reflection Electron Imaging of Surfaces*, Plenum Press, New York, 1988.

Neutron Scattering

Ashcroft, N. W., and N. D. Mermin, *Solid State Physics*, Saunders College, Philadelphia, 1976.

Bacon, G. E., *Neutron Diffraction*, 3rd ed., Clarendon Press, Oxford, 1980.

Optical Spectroscopy

Palik, E. D., ed., *Handbook of Optical Constants of Solids*, Academic Press, San Diego, Calif., Vol. 1: 1985, Vol. II: 1991.

Ellipsometry

Aspnes, D. E., The accurate determination of optical properties by ellipsometry, in, E. D. Palik, ed., *Handbook of Optical Constants of Solids* Vol. I, Academic Press, San Diego, Calif., 1985.

Azzam, R. M. A., Ellipsometry, in, M. Bass, ed., *Handbook of Optics*, Vol. 2, McGraw-Hill, New York, 1995.

Jackson, J. D., *Electrodynamics*, 2nd ed., Wiley, New York, 1975.

FTIR

Bell, R. J., *Introductory Fourier Transform Spectroscopy*, Academic Press, San Diego, Calif., 1972.

Chamberlain, J. E., *The Principles of Interferometric Spectroscopy*, Wiley, New York, 1979.

Griffiths, P. R., and J. H. de Haseth, *Fourier Transform Infrared Spectrometry*, Wiley, New York, 1986.

Raman Scattering

Colthup, N. B., *Introduction to Infrared and Raman Spectroscopy*, 3rd ed., Academic Press, San Diego, Calif., 1990.

Ferraro, J. R., *Introductory Raman Spectroscopy*, Academic Press, San Diego, Calif., 1994.

Herzberg, G., Molecular spectra and molecular structure, in *Infrared and Raman Spectra of Polyatomic Molecules*, Prentice-Hall, New York, 1939.

Ferraro, J. R., and K. Nakamoto, eds., *Introductory Raman Spectroscopy*, Academic Press, San Diego, Calif., 1994.

Luminescence

Alfano, R. R., *Semiconductors Probed by Ultrafast Laser Spectroscopy*, Academic Press, San Diego, Calif., 1984.

Ropp, R. C., Luminescence and the Solid State, Vol. 12 of *Studies in Inorganic Chemistry*, Elsevier, Amsterdam, 1991.

Nonlinear Spectroscopy

Bloembergen, N., *Nonlinear Optics*, Addison-Wesley, Reading, Mass., 1992.

Butcher, N., and D. Cotter, *The Elements of Nonlinear Optics*, Cambridge University Press, New York, 1990.

Mills, D. L., *Nonlinear Optics: Basic Concepts*, Springer-Verlag, New York, 1991.

Newell, A. C., and J. V. Moloney, *Nonlinear Optics*, Addison-Wesley, Reading, Mass., 1992.

Shen, Y. R., *The Principles of Nonlinear Optics*, Wiley, New York, 1984.

SEM

Goldstein, J. I., et al, *Scanning Electron Microscopy and X-ray Microanalysis: A Text for Biologists, Materials Scientists, and Geologists*, 2nd ed., Plenum Press, New York, 1992.

Lyman, C. E., et al., *Scanning Electron Microscopy, X-ray Microanalysis and Analytical Electron Microscoscopy*, Plenum Press, New York, 1990.

Reimer, L., in P. Hawkes, ed., *Scanning Electron Microscope*, Springer-Verlag, Berlin, 1985.

TEM

Edington, J. W., *Practical Electron Microscopy in Materials Science*, N. V. Philips, Eindhoven, The Netherlands, 1976.

Reimer, L., *Transmission Electron Microscopy*, Springer-Verlag, Berlin, 1984.

HRTEM

Buseck, P., J. Cowley, and L. Eyring, eds., *High-Resolution Transmission Electron Microscopy and Associated Techniques*, Oxford University Press, New York, 1988.

Spence, J. C. H., *Experimental High Resolution Electron Microscopy*, Oxford University Press, New York, 1988.

LEEM

Howie, A., and U. Valdre, eds., *Study of Surfaces and Interfaces by Electron Optical Techniques*, Plenum Press, New York, 1987.

Photoemission

Cardona, M., and L. Ley, eds., *Photoemission in Solids*, Springer-Verlag, Berlin, 1978.

Feuerbacher, B., ed., *Photoemission and the Electronic Properties of Surfaces*, Wiley, New York, 1978.

XPS

Carlson, T. A., *Photoelectron and Auger Spectroscopy*, Plenum Press, New York, 1978.

Ibach, H., ed., *Electron Spectroscopy for Chemical Analysis*, ed., Springer-Verlag, Berlin, 1978.

LEELS

Ibach, H., *Electron Energy Loss Spectroscopy and Surface Vibrations*, Academic Press, San Diego, Calif., 1982.

EXAFS

Koningsberger, D. C., and R. Prins, eds., *X-ray Absorption: Principles, Applications, Techniques of EXAFS, SEXAFS, and XANES*, Wiley, New York, 1988.

Teo, B. K., *EXAFS: Basic Principles and Data Analysis*, Springer-Verlag, Berlin, 1986.

AES

Briggs, D., and M. P. Seah, *Practical Surface Analysis by Auger and X-ray Photoelectron Spectroscopy*, Wiley, New York, 1983.

SIMS

Benninghoven, A., F. G. Rudenauer, and H. W. Werner, *Secondary Ion Mass Spectroscopy*, Wiley-Interscience, New York, 1987.

RBS

Chu, W. K., J. W. Mayer, and M. A. Nicolet, *Backscattering Spectrometry*, Academic Press, San Diego, Calif., 1978.

Feldman, L. C., and J. W. Mayer, *Fundamentals of Surface and Thin Film Analysis*, North-Holland, New York, 1986.

AFM

Sarid, D., *Scanning Force Microscopy with Applications to Electric, Magnetic and Atomic Forces*, Oxford University Press, New York, 1991.

STM

Neddermeyer, H. ed., *Scanning Tunneling Microscopy*, Vol. 6, *Perspectives in Condensed Matter Physics*, Kluwer, Boston, 1993.

Transport Measurements

Lark-Horovitz, K., and V. A. Johnson, eds., *Solid State Physics*, in Marton, L. ed., *Methods of Experimental Physics*, Vol. 6, Academic Press, San Diego, Calif., 1959.

NMR and NQR

Abragam, A., *The Principles of Nuclear Magnetism*, Oxford University Press, Oxford, 1978.

Slichter, C. P., *Principles of Magnetic Resonance*, 3rd enlarged and updated ed. Springer-Verlag, Berlin, 1990.

ESR

Abragam, A., and B. Bleaney, *Electron Paramagnetic Resonance of Transition Ions*, Clarendon Press, Oxford, 1970.

Pake, G. E., *Paramagnetic Resonance*, W.A. Benjamin, New York, 1962.

Poole, C. P., and H. A. Farach, *Theory of Magnetic Resonance*, 2nd ed., Wiley, New York, 1987.

Mössbauer Effect

Gibb, T. C., *Principles of Mössbauer Spectroscopy*, Chapman & Hall, London, 1976.

Wertheim, G. K., *Mössbauer Effect: Principles and Applications*, Academic Press, San Diego, Calif., 1964.

PAS

Coleman, C. F., and A. E. Hughes, Positron annihilation, in *Research Techniques in Nondestructive Testing*, Vol. 3, R. S. Sharpe, ed., Academic Press, San Diego, Calif., 1977.

Hautojarui, P., *Positrons in Solids*, Springer-Verlag, Berlin, 1979.

μPS

Chappert, J., and R. I. Grynczpan, eds., *Muons and Pions in Materials Research*, North-Holland, Amsterdam, 1984.

PROBLEMS

W22.1 A beam of x-rays impinges on the surface of a metal at a small angle of incidence. Treat the metal as a plasma. Show that total-internal reflection is possible when the angle is sufficiently small. Derive an expression for the critical angle in terms of the plasma frequency of the metal and the frequency of the x-rays.

W22.2 The Bragg description of x-ray scattering assumes that specular scattering from the various lattice planes occurs. What happens when nonspecular scattering occurs? Does one find additional peaks due to nonspecular scattering?

W22.3 Light is incident normally on a film of material of thickness D characterized by the complex index of refraction $\tilde{n} = n + i\kappa$. Derive expressions for the reflection coefficient and the transmission coefficient. What fraction of the radiation is absorbed inside the medium? Consider the multiple reflections inside the slab.

W22.4 Given the dielectric function $\epsilon(\omega) = 1 - \omega_p^2/\omega(\omega + i/\tau)$ for a plasma, verify the following sum rules:

$$\int_0^\infty \omega\epsilon_2(\omega)d\omega = \frac{\pi}{2}\omega_p^2,$$

$$\int_0^\infty [n(\omega) - 1]d\omega = 0,$$

$$\epsilon_1(\omega) = \frac{2}{\pi}\mathscr{P}\int_0^\infty \frac{\omega'\epsilon_2(\omega')}{\omega'^2 - \omega^2}d\omega',$$

$$\epsilon_2(\omega) - \frac{4\pi}{\omega}\sigma(0) = -\frac{2}{\pi}\omega\mathscr{P}\int_0^\infty \frac{\epsilon_1(\omega') - 1}{\omega'^2 - \omega^2}d\omega'.$$

[The symbol $\mathscr{P}$ denotes taking the "principal part" (i.e., leaving out a small region around the singularity when evaluating the integral and then making the region smaller and smaller in such a way that the integral remains nonsingular).] The last two equations are called the *Kramers–Kronig relations*. All these formulas are general.

W22.5 Derive the Rutherford differential scattering cross section for a charge Z_1e, moving with kinetic energy E, scattering through an angle θ off a stationary charge Z_2e:

$$\frac{d\sigma}{d\Omega} = \frac{Z_1^2Z_2^2e^4}{16E^2(4\pi\epsilon_0)^2}\frac{1}{\sin^4(\theta/2)}.$$

W22.6 Derive the cross section for an ion of charge Ze scattering from a molecule and vibrationally exciting it. To a first approximation, assume that the charge

moves on a straight line with velocity v and impact parameter b. Model the molecule as a simple harmonic oscillator with spring constant k, mass M, and a charge $+q$ at one end of the spring and $-q$ at the other end. Compute the impulse delivered to the oscillator. Assume that the oscillator is excited when the energy transferred exceeds the vibrational quantum of energy hf. Proceed to calculate the cross section for low-energy electron loss spectroscopy from a layer of molecules on the surface of a solid.

W22.7 Repeat the calculation in Problem. W22.6 using the Born approximation (i.e., representing the incident and outgoing wavefunctions as plane waves and using first-order time-dependent perturbation theory). Assume that the moving charge couples to the harmonic oscillator by the Coulomb interaction. You may assume that the amplitude for molecular vibration is small compared with other relevant distances.

W22.8 In the atomic-force microscope, as well as the scanning-tunneling microscope, it is important to try to eliminate the effect of external vibrations as much as possible. Model the cantilever and stylus as a spring–mass system, with resonant frequency ω_0, as shown in Fig PW22.8. Show that if the entire microscope is made to oscillate up and down with frequency ω and amplitude A, the distance between the stylus and the sample will oscillate with the same frequency but with an amplitude approximated by $(\omega/\omega_0)^2 A$, when $\omega \ll \omega_0$.

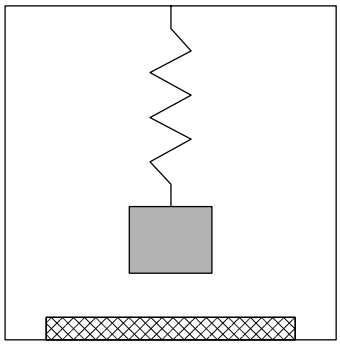

Figure PW22.8

W22.9 K-shell electrons of Cl^- ions in NaCl absorb x-rays of wavelength λ. The energy needed to ionize this electron from the K shell will be denoted by I_K. The NN distance is denoted by a. EXAFS oscillations are observed when λ is varied. Find the periods of these oscillations. Include the effect from NNs and next-NNs.

W22.10 Electrons with 200 eV energy are incident on the (100) face of GaAs. Find the angles at which the LEED beams will emerge. Repeat the calculation for the (111) and (110) faces.

W22.11 Calculate the force between the stylus of the atomic-force microscope and a solid material. Model the stylus as a sphere of radius R and the solid as a half-space filled with material in the region $z < 0$. Let the minimum distance between the sphere and plane be H. Assume a concentration n_s of atoms per

unit volume in the stylus and correspondingly n_m in the material. Assume that each stylus atom interacts with each material atom through the Lennard-Jones potential given in Eq. (2.3):

$$u(r) = 4\varepsilon \left[\left(\frac{\sigma}{r}\right)^{12} - \left(\frac{\sigma}{r}\right)^{6} \right],$$

where ε and σ are constants characterizing the interaction and the $1/r^6$ term represents the van der Waals potential. (To obtain a precise answer, it will probably be necessary to do a numerical integration. You may, instead, make whatever reasonable assumptions are necessary to obtain an estimate.)

W22.12 A silver mirror is found to have a reflectivity R as a function of wavelength λ given by the following data:

$\lambda(\mu\text{m})$	0.20	0.30	0.40	0.50	0.60	0.70	0.80	0.90	1.00
R (%)	20	12	85	91	93	95	97	98	98

Why is the reflectivity so high at long wavelengths? Use the data above to estimate the plasma frequency, ω_p, of Ag.

W22.13 An x-ray diffraction study of $(Ca_{0.3}Sr_{0.7})_{0.9}CuO_2$ made with the Cu(Kα) line ($\lambda = 0.1544$ nm) reveals peaks at the following values of the angle $\psi = 2\theta$ (in degrees): 23.1, 26.7, 32.4, 35.3, 42.6, 46.5, 54.9, 59.8, 65.4, 68.2. The crystal is believed to be orthorhombic. Find the reciprocal lattice vectors and lattice constants.

W22.14 Indium, at room temperature, is a tetragonal crystal with $a = 0.325$ nm and $c = 0.495$ nm. Find the 2θ values for the first 16 x-ray diffraction peaks. Assume that the Mo (Kα) line is used ($\lambda = 0.07136$ nm).

W22.15 Six surfaces of a crystal are shown in Fig. PW22.15. The two leftmost figures show the (100) and (111) faces of an FCC crystal. The remaining figures show adsorbed atoms on these faces. In the primitive 2×2 [$p(2 \times 2)$] structures and the centered 4×2 structure [$c(4 \times 2)$] one-fourth of a monolayer is adsorbed. In the centered 2×2 structure [$c(2 \times 2)$], one-half of a monolayer is adsorbed. Find the LEED pattern from each of the six surfaces.

(*Note*: Often, faces of pure crystals will reconstruct and substrate atoms will occupy the sites occupied by adsorbate atoms, as in this example.)

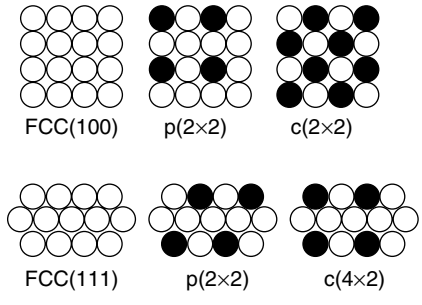

Figure PW22.15

W22.16 Ring patterns are formed when x-rays are diffracted from a crystalline powder. Show that the radii of the rings vary with the integers N as $r_N \propto \sqrt{N}$. What are the allowable values for N for the following crystal structures: simple cubic, BCC, FCC, and diamond?

W22.17 Given $\Delta\theta = 0.05$ rad for the (100) diffraction maximum from polycrystalline Al, use Eq. (W22.4) to find the average crystallite size. Use $\lambda = 0.1$ nm.

Computer Problems

W22.18 To get a feeling for the design of an electron microscope, write a program to determine the focal length for a beam of electrons directed toward a charged ring at normal incidence. To do this, obtain an expression for the electric field at an arbitrary point in space set up by a charged ring of unit radius. This may be left as an integral over the length elements of the ring. Numerically integrate Newton's second law, taking as the initial condition the displacement of the electron from the axis. Determine where this beam crosses the symmetry axis. Show that to a first approximation, this focal length is independent of the original distance from the axis. To the next approximation you may use the program to study the spherical aberrations of this electrostatic lens.

W22.19 Repeat Problem W22.18 for an electron beam directed at a circular loop of wire carrying an electric current. This time use the Biot–Savart formula to calculate the magnetic field at an arbitrary point in space, and calculate the magnetic force on a moving electron. Proceed as before to integrate Newton's equations of motion numerically.

W22.20 A commonly used device in SIMS is the electrostatic quadrupole mass analyzer. It consists of four parallel cylinders whose projections form a square. Two diagonally opposite wires are positively charged and the other two are negatively charged. Show that to a first approximation, the angle of deflection of an electron beam is independent of its distance from the plane of reflection symmetry of the wires. To the next approximation, study the aberrations of this device.